UNIVERSITY OF CALIFORNIA
SANTA CRUZ

CUSTOM TAILORING OF NANOPARTICLE PROPERTIES THROUGH SURFACE MANIPULATION

A dissertation submitted in partial satisfaction
of the requirement for the degree of

DOCTOR OF PHILOSOPHY

in

CHEMISTRY

by

Chris Deming

September 2016

The dissertation of Chris Deming
is approved

Professor Shaowei Chen

Professor Ilan Benjamin

Professor Yat Li

Tyrus Miller
Vice Provost and Dean of Graduate Studies

Table of Content

LIST OF FIGURES

Chapter 1

Chapter 3

Chapter 4

Chapter 5

Chapter 6

LIST OF TABLES

Chapter 4

Chapter 5

Chapter 6

CUSTOM TAILORING OF NANOPARTICLE PROPERTIES THROUGH SURFACE MANIPULATION

Chris Deming

ABSTRACT

The extensive research in the development of nanomaterials for applications diverse as energy and medicine is a result of the unique properties of nanomaterials, especially given the countless reports of facile and safe techniques for controlled modification of nanomaterial properties. What is more interesting and is at the heart of all research is the connection between morphological, compositional, or other physical characteristic and the exhibited performance or function for a given application. To further the effectiveness of nanomaterial-based technologies we must additionally understand the relationship between our processing and treatment of the material and the resulting structural features, hence providing a route to control and exploit the material's properties. This dissertation accounts my search for such a level of understanding of the behavior of materials on the nanoscale where manipulation of the nanoparticle interface has provided fine tuning of particle properties for selective sensing of chemical vapors as well optimization of conditions for electrocatalytic oxygen reduction

Films of organically capped metal nanoparticles are a common method for sensing organic vapors by measuring conductivity loss upon film solvation. As this

mechanism provides very sensitive detection, selectivity on the basis of solvation is not specific enough for a practical sensing. Instead, selectivity based on specific structural groups is required. Recently it was found that nitrene functionalized ruthenium nanoparticles selectively react with vinyl groups through imido transfer. This selectivity was exploited for a chemical sensor where the electronic conductivity of a solid film of ruthenium functionalized ruthenium nanoparticles was measured and compared in the presence of vapors of relative polarity including ethanol, acetone, n-hexane, 1-hexene, toluene and styrene. The ensemble conductivity was found to decrease upon exposure to each vapor with the largest drop resulting from toluene and styrene vapors. Interestingly, the decrease in conductivity was 2.5 times larger for styrene than toluene, despite the similarity in structure and hence solvation properties. This discrepancy is attributed to a chemical interaction between the ruthenium nitrene bond and vinyl groups that alter the nature of the conductive media between the metal cores and diminish conductivity based on specific functional groups rather than solvation alone.

Current fuel cell technologies are severely limited in part by a large amount of precious metal catalyst required for energy extraction. To remedy this issue, alloy nanoparticles have allowed for not only the reduction of precious metal required but have displayed actual enhancement in activity over either pure constituent metal. This enhancement results from the mixing of metal d bands upon alloying and thus an electronic environment in between that of the pure metals. Gold palladium nanoparticle alloys offer a promising route for an efficient electrocatalyst since an

optimal electrocatalyst would exhibit properties in between than of gold and palladium. Dodecyne-capped AuPd alloy nanoparticles of varying compositions were therefore prepared through the co-reduction of metal-salt precursors with $NaBH_4$. TEM measurements showed that the particles were largely in the range of 2–6 nm in diameter. XPS studies showed that the atomic Pd concentration varied from 65 to 100 %. Infrared spectroscopic measurements confirmed the bonding attachment of the dodecyne ligands on the nanoparticle surfaces, which rendered the nanoparticles readily dispersible in common organic media. Electrochemically, the resulting nanoparticles exhibited apparent catalytic activity in oxygen reduction with a volcano-shaped variation with the metal composition. The best performance was identified with the sample composed of 91.2 at% Pd that exhibited a mass activity over eight times better than that of commercial palladium black, and almost twice as good in terms of specific activity. This remarkable performance was accounted for by the manipulation of the electronic interactions between palladium and oxygen resulting from alloying with gold.

Of the many methods to enhance the electrocatalytic oxygen reduction activity of a metal nanoparticle, the incorporation of an active support, such as graphene quantum dots (GQD), has proven very effective. The strong electron withdrawing effects of the oxygen groups of GQDs as well as the ease of manipulating the level of these groups through thermal or chemical treatment may be exploited to find tune metal nanoparticles for electrocatalysis. GQD-supported palladium nanoparticles were synthesized by thermolytic reduction of $PdCl_2$ in 1,2-propanediol at 80 °C in the

presence of GQDs and then were subject to hydrothermal treatment at an elevated temperature within the range of 140 to 200 °C. Transmission electron microscopic measurements showed a raspberry-like morphology for the samples before and after hydrothermal treatment at temperatures ≤ 160 °C, where nanoparticles of ca. 8 nm in diameter formed large aggregates in the range of 50 to 100 nm in diameter, and at higher hydrothermal temperatures (180 and 200 °C), chain-like nanostructures were formed instead. X-ray photoelectron and Raman spectroscopic measurements revealed that the GQD structural defects were readily removed by hydrothermal treatments, and the defect concentrations exhibited a clear diminishment with increasing hydrothermal temperature, as indicated by the loss of oxygenated carbons in XPS and a drop in the D to G band ratio in Raman measurements. Voltammetric studies showed apparent electrocatalytic activity toward oxygen reduction, with a volcano-shaped variation of the activity with GQD defect concentration, and the peak activity was observed for the sample prepared at 180 °C with a mass activity of 23.9 A/g Pd and specific activity of 1.08 A/m^2 at +0.9 V vs RHE. This peak activity is attributed to optimal interactions between Pd and GQD where the GQD defects promoted charge transfer from metal to GQDs and hence weakened interactions with oxygenated intermediates, leading to enhanced ORR activity. The corresponding defect concentration was higher than that identified with the platinum counterparts due to the stronger affinity of oxygen to palladium.

While the oxygen groups of non doped GQDs provide a facile source of electronic modulation for neighboring particles, elevated levels may result in loss of

conductivity, stability, and performance. To overcome this obstacle, nitrogen may be incorporated into the graphitic structure. Similar to level of oxygenated groups on GQDs, nitrogen exists in pyrrolic, pyridinic, and quaternary forms depending on synthetic conditions. To determine the effect of each center on neighbor metal nanoparticle activity, nanocomposites (PdNGQD) based on palladium nanoparticles supported on nitrogen-doped graphene quantum dots were synthesized through a hydrothermal co-reduction method at 160 °C for various periods of time. Transmission electron microscopic studies revealed that all samples exhibited similar morphology with small nanoparticles clustered into larger superstructures of 100 nm and larger. X-ray photoelectron spectroscopic studies showed the NGQDs contained only pyridinic and pyrrolic nitrogen centers, and that the relative abundance of pyrrolic nitrogen increased with prolonging reaction duration whereas a concurrent decrease was observed with the pyridinic nitrogen. The binding energy of the Pd 3d electrons was also found to increase with increasing reaction time. Such a correlation with the pyrrolic nitrogen concentration suggests apparent interactions between palladium and the nitrogen moiety. Accordingly, Raman spectroscopic measurements exhibited an increase of the I_D/I_G ratio, indicative of an increasingly defective structure of the NGQD probably due to the increasing abundance pyrrolic centers which will provide more structural strain than the 6 membered pyridinic heterocycles within the graphitic backbone. Voltammetric studies revealed significant electrocatalytic activity towards oxygen reduction in alkaline media, with the best mass activity of 77.0 A/g at +0.84 V from the sample prepared by 1 h of thermal

treatment, whereas the top specific activity of 31.6 A/m^2 at +0.84 V from the sample prepared by 8 h's heating. These samples represent the optimal combination of electron withdrawing effects form the nitrogen centers and the oxygen groups and it was found that the palladium environment and thus electrocatalytic activity was much more correlated with the pyrrolic concentration rather than the abundance of oxygenate moieties.

Dedicated to

Molly and William

ACKNOWLEDGMENTS

I would first like to thank my boss, mentor, and friend Professor Shaowei Chen for his guidance and support throughout my time working in his lab. As a young undergraduate researcher in his lab, I was very fortunate that he saw potential in me and extended an invitation to continue this work as a graduate student. I am very grateful for this gesture as well as the following years spent working in the Chen lab. None of the following work would be possible without his help and support.

I would also like to thank my committee members, professor Ilan Benjamin and Professor Yat Li. When I initially asked Professor Benjamin to be my committee chair, he had just approved 3 similar requests so I very much appreciate him accepting my request as well as the support thereafter. Additionally, I am very appreciative that both members were very helpful in applying for various positions, especially on short notice.

I owe huge thanks to my colleagues over the years. This includes the past and current members of the great Chen lab as well those in the neighboring Zhang, Li, and Kliger labs. Because of them I have learned so much about laboratory research and working with other towards a common goal.

I would also like to thank all of the friends I have made throughout my time at UCSC. Friendly faces in the workplace are one of the most valuable aspects of a job and I feel very lucky with the people I worked with and around. Special thanks to the Bucky Ballerz and the basketball crew. The exercise and relaxation from playing

with all of you gave me the physical workout when I needed a break from the mental workout.

Big thanks to Virginia Altoe at the Molecular Foundry LBNL for training me in X-Ray photoelectron spectroscopy and Chengyu Song at NCEM LBNL for teaching me to use transmission electron microscopy. I very much appreciate their patience in teaching me the details of using complicated and expensive instruments and I have gained invaluable skill from these great scientists.

I would like to thank my parents for the endless support they have given. As far back as I can remember, I have had loving parents who have enabled me to excel in academics and achieve my goals. I love you, mom and dad.

Last but not least I would like to thank my wonderful girlfriend Molly and our son William. Molly is the love of my life and brought me endless happiness through her spirit, intelligence, and beauty. We are eternally bound through our love for each other and our love for our son. Her support and dedication have provided me the much needed time to complete my degree and for that, I will be forever thankful. To my new best friend William, I thank you for showing me who I am and want to be. You have brought me joy I never thought possible and you will never be far from my thoughts. Everything I do is for you and I hope when you're older you will read this and feel happy as I do now thinking about your smile. Thank you, my man William.

The text of this dissertation includes reprints of the following previously published material

Chapter 3: Christopher P. Deming, Xiongwu Kang, Ke Liu, Shaowei Chen, "Nitrene-Functionalized Ruthenium Nanoparticles: Selective Manipulation of Nanoparticle Electronic Conductivity by Vinyl Derivatives", Sensor Actuat B-Chem, 2014, 194, 319

Chapter 4: Christopher P. Deming, Albert Zhao, Yang Song, Ke Liu, Mohammad M. Khan, Veronica M. Yates, and Shaowei Chen, "Alkyne-protected AuPd alloy nanoparticles for electrocatalytic reduction of oxygen", ChemElectroChem, 2015, 2, 1719

Chapter 5: Christopher P. Deming, Rene Mercado, Vamsi Gadiraju, Samantha Sweeney, Mohammad M. Khan, Shaowei Chen, "Graphene Quantum Dots-Supported Palladium Nanoparticles for Efficient Electrocatalytic Reduction of Oxygen in Alkaline Media", ACS Sustainable Chem. Eng., 2015, 3, 3315

Chapter 1

Introduction

1.1 Background

The advent of nanomaterials has provided a crucial link between bulk materials that we generally experience in everyday life and the individual atoms that are the basic building blocks bulk materials. As an intermediate between these two size regimes, nanomaterial retain some properties of both, such as orbital overlap as in bulk material yet with discrete energy levels like an atom. Much of these unique optical and electronic properties arise from the large surface area to volume ratio. That is, the number of surface atoms is comparable to the number of interior atoms and thus the characteristics are strongly influenced by the surface atoms rather than solely by the interior atoms as would be for bulk materials. Therefore, unique and unprecedented optical and electron properties arise. Additionally, the incredible surface area to volume ratio provides the ample sites for catalysis or other surface processes. In all, the characteristics of nanomaterials are exceptional for many applications including chemical sensing,[1-3], waste cleanup[4,5], catalysis[6,7], electrocatalysis[8-11], and photo conversion processes.[12-14]

For example, nanoparticle arrays have provided superior sensitivity as chemical sensors due to the large change in photoluminescent and/or conductive properties upon surface modification.[1-3,15] and platinum nanoparticles are necessary for fuel cell operation in electric engines due to the intrinsic electrocatalytic activity and stability.[16,17] Although these examples represent only a fraction of the applications of nanomaterials, what is necessary for practical use in all applications is the optimization of properties. That is, high sensitivity does not make for a good

sensor if there is no selectivity while efficient light absorption will not help in solar energy conversion if the range does not correspond to that of the sun's output. An electrocatalytic formation of an undesirable product will limit the electrical energy output of a fuel cell while removal of everything from a liquid sample provides no advantage over simple filtration.

To advance any of these fields, the nanomaterial must be optimized for the desired application. Accordingly, much effort has been focused towards developing techniques to manipulate nanomaterial properties.[18-25] The goal in all of these techniques is optimization of properties through well-controlled manipulations of particle characteristics.[26-28] Therefore, the development of the connection between morphological, compositional, or other physical characteristics and the performance in practical applications is the primary motivation of this dissertation as well as to expanding the repertoire of methods to control such properties.

1.2 Chemical Sensing

The detection of chemical vapors through the utilization of organically capped metal nanoparticle films is a very common and effective method to detect vapors at a low concentration. [1-3] For these nanoparticle films, the mechanism for detecting chemical vapors is by monitoring the change in conductivity of the film ensemble upon exposure to the vapor. Often referred to as a chemiresistor, charge travels though the film by tunneling from one metal core to the next with the conductivity dependent on the distance between metal centers as well as the nature of the media in between each center. Upon solvation of this film, the centers will be forced farther

apart and a significant loss in conductivity is measurable for even low concentrations of the vapor.[29-31] Of course, this will require that the functionalized nanoparticles are solvated by the vapor but this is not a very strict criterion for detection and, in fact, makes for a very poor practical chemical sensor due to this low selectivity. Therefore, advancement of such technology centers on improving the selectivity of chemical detection. One possible route is to functionalize the metal particle with a ligand that displays selective reactivity towards a molecule or functional group. Such a reaction may change the nature of the media between the metal cores and affect the conductivity similar to solvation swelling but with a more targeted stimulus.

It has recently been found that nitrene functionalized ruthenium nanoparticles exhibit unique chemical reactivity towards vinyl groups my means of imido transfer.[19] The nitrene bonds allow for delocalization of electrons from ligand to core, as evidenced by strong photoluminescent properties, and provide a bridge for electron hopping from core to core during charge transfer through organic ligand capped metal nanoparticle films. More interestingly, it was found that this imido transfer cuts off the conjugation between ligand and particle resulting in a complete loss of photoluminescent activity and hence electron delocalization. Chapter 3 details the research aimed to exploit this interaction to develop a sensitive chemical sensor that will be selective to only vinyl groups.

1.3 Hydrogen Fuel Cells

Fuel cells, in specific, polymer electrolyte membrane fuel cells (PEMFC), are currently deemed as a promising source of clean renewable energy for stationary and

mobile applications.[32-35] The fast startup and large energy density are optimal for powering large mobile devices, and the ability to stack such fuel cells allows for control over voltage output.[34-36] With water as the only product and numerous sustainable routes to hydrogen generation, hydrogen fuel cells offer much promise to eliminate our dependence on fossil fuels, in addition to reducing greenhouse gas emissions.

A general PEMFC is characterized by anode and cathode compartments which are separated by a membrane designed to exchange only protons. In these compartments is where the redox reactions occur. Hydrogen gas is fed in at anode where it is oxidized and the resulting protons migrate through the selective ionomer polymer matrix while the electrons travel through the external circuit to meet back with the protons at the cathode to reduce oxygen to water. This process is depicted in Figure 1.1 and the individual and overall reactions are given in equations 1.1-1.3.

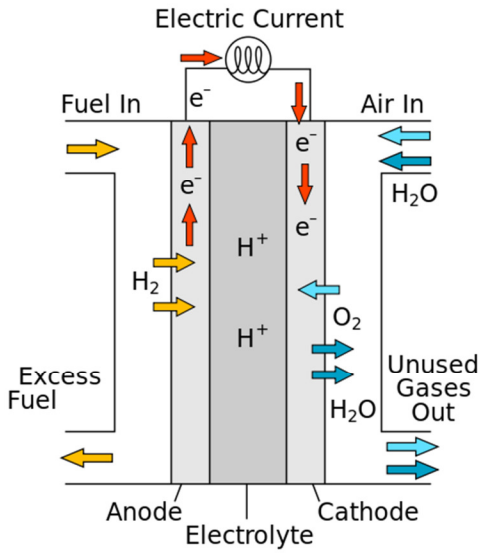

Figure 1.1. Diagram of a polymer electrolyte membrane fuel cell

$$Anode \quad 2H_2 \rightarrow 4H^+ + 4e^- \tag{1.1}$$

$$Cathode \quad O_2 + 4H^+ + 4e^- \rightarrow 2H_2O \tag{1.2}$$

$$Overall \quad O_2 + 2H_2 \rightarrow 2H_2O \tag{1.3}$$

Very closely related to this PEMFC, is the alkaline anion fuel cell which mainly differs in that operation is under basic conditions and that the polymer membrane is designed to selectively allow passage of hydroxide anions rather than protons. The half reactions under basic operation are given in equations 1.4-1.5. The full reaction is the same as in acidic media.

$$Anode \quad 2H_2 + 4OH^- \rightarrow 4H_2O + 4e^- \tag{1.4}$$

$$Cathode \quad O_2 + 2H_2O + 4e^- \rightarrow 4OH^- \tag{1.5}$$

Both situations will provide a maximum of 1.23 V during operation but due to kinetic limitations of the oxygen reduction, some of this energy is lost to heat.

It is well-known that the sluggish kinetics of electrochemical oxygen reduction (ORR) is a significant limitation to the efficiency of fuel cells and therefore a metal catalyst must be utilized.[17,37,38] Platinum has been recognized as the best single metal catalyst for oxygen reduction due to the stability under the harsh operating conditions of the cell as well as a high intrinsic activity, but must be used in excess of 50 g for a 100 kW vehicle given the state of the art PEMFC (polymer electrolyte membrane fuel cell) [16]. This requirement significantly limits commercial production given the yearly global output of Pt and the yearly demand for motor vehicles. Experts predict that the benchmark activity of 160 A/g and 200 μA/cm^2 at +0.90 V must be significantly enhanced for this technology to emerge in the market

as a cost efficient alternative to internal combustion engine vehicles. To improve the intrinsic nature of a metal towards oxygen reduction, it is beneficial to examine the individual steps that comprise the complete reduction.

Many ORR pathways have been proposed [39], and in general, each pathway involves adsorption of oxygen on the catalyst surface followed by electron transfer/proton addition, ending with the release of water. Depending on the metal surface the rate limiting step mostly will either be the initial electron transfer or the final release of the product.

It has been shown experimentally and computationally that the strength of interactions between different oxygenated intermediates (OIs) and a catalyst surface cannot be independently optimized. This idea is rationalized by the fact that all intermediates bind to the catalyst surface through the oxygen atom and that stronger or weaker surface interactions for one intermediate will yield the same result for all other surface bound intermediates. Therefore a surface that binds too strongly to oxygen will undergo facile initial adsorption (initial step) of oxygen but will not easily release the final product (final step) resulting in the poisoning of active sites and poor activity. Metals that bind to oxygenated species too weakly will allow for the rapid release of the final product but will also result in an unfavorable initial step of oxygen adsorption and consequently will exhibit poor activity. Therefore the best catalyst will exhibit moderate adsorptive interactions with OIs to maximize the rate of the limiting step. The benchmark activity of 160 A/g and 200 μA/cm2 at +0.90 V

measured for carbon supported platinum nanoparticles is therefore attributed to the moderate binding to OIs.

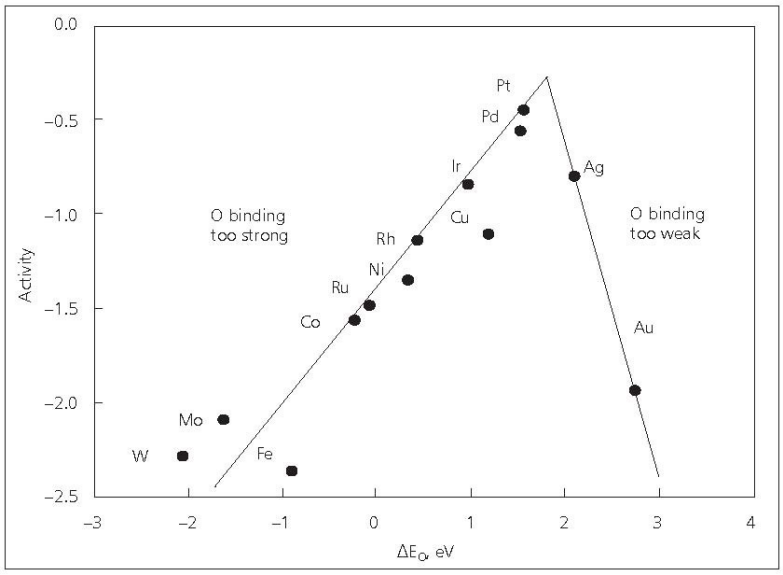

Figure 1.2. Trends in oxygen reduction activity plotted as a function of the oxygen binding energy (Reprinted with permission from Holton, O. T.; Stevenson, J. W.: The Role of Platinum in Proton Exchange Membrane Fuel Cells. Platin Met Rev 2013, 57, 259-271.) Copyright (2013) American Chemical Society

Although platinum displays the highest reported activity as a single metal catalyst, theoretical predictions indicate platinum still binds to OIs too strongly. This model, in fact, shows a volcano-shaped trend when activity is plotted vs metal/adsorbate binding energy for different metals. This trend was predicted by Sabatier over 100 years ago [40] and is graphically represented in Figure 1.2. Here the x-axis represents the strength of binding interaction with O* and the y-axis represents the activity for each metal.

Furthermore, to quantitatively describe the adsorptive behaviors of metals, a model has been developed relating the d band center of a metal to adsorptive

properties. This model states that an upshift of the d band center relative the Fermi level will create empty anti-bonding states that result in stronger bonding to adsorbates. The converse is also true that a downshift of the d band center will result in weaker interactions with adsorbates. This model is particularly useful in predicting how a catalyst surface will respond to structural modifications and when coupled with the dynamics of OIs on the surface, gives a promising outline for future catalysts to meet and/or exceed the theoretical maximum and afford the efficiency required for large scale commercialization.

Thus, significant research efforts have been devoted to the development of alternative catalysts so as to minimize the use of precious metal catalysts and concurrently improve the ORR activity. In fact, a variety of strategies have been reported, such as controlled growth of particle facets and shapes,[23,41-43] alloying of metal nanoparticles,[44-47] catalyst size control,[48-51] surface organic functionalization,[26,52-54] and utilization of new supporting substrates for catalysis.[25,27,55-57]

1.4 Electrocatalytic Oxygen Reduction Evaluations

To analyze the electrocatalytic oxygen reduction activity of a sample, rotating ring disk electrode voltammetry is utilized. This cylindrical (Figure 1.3 A) electrode will generally consist of a glassy carbon disk electrode where the sample is cast and oxygen reduction occurs in addition to a concentric gold or platinum ring that is insulated from the disk electrode. For this method, the rotation of the electrode in an oxygen saturated NaOH solution creates a well-defined convective profile that forces

the transport of dissolved oxygen from solution to the disk electrode at a rate determined by the rotational rate of the spinning electrode. The applied potential of the disk electrode is then swept in toward less positive potentials linearly with time and the current from the reduction of oxygen is measured by the disk electrode. This profile is characterized by no current response at higher potentials and as the potential is swept, an apparent increase in current is observed until reaching a plateau at less positive potentials. Such a profile can be seen in Figures 4.5, 5.4 A, and 6.8 A. When performed at different rotation rates, analysis of the current responses can yield information on the kinetics of the electrocatalytic reduction through Koutecky-Levich analysis.

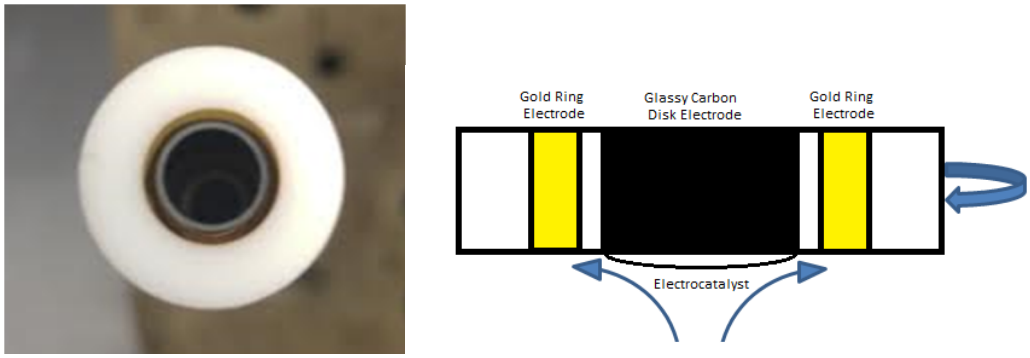

Figure 1.3. (Left panel) Image of rotating ring disk electrode. (Right panel) Illustration of rotating ring disk electrode including electrocatalyst layer and convective profile of dissolved oxygen

At larger positive potentials, the current response is completely controlled by the applied potential. This is evident by the lack of current for all rotation rates. At less positive potentials, the current response is solely determined by the rate of oxygen transfer to the surface, a function of electrode rotation rate. This can be

rationalized by the stark difference in the current for each rotation rate as well as the lack of dependence on the applied bias for this potential region. It is the region connecting each of the plateaus where the measured current response results from both the transfer of oxygen to the electrode surface, called the diffusion current (I_d), and the electrons transferred in the catalyzed oxygen reduction, the kinetic current (I_k). The relationship between these currents and the total current measured at the disk electrode (I_D) is given in equation 1.6-1.8,

$$\frac{1}{I_D} = \frac{1}{I_k} + \frac{1}{I_d} = \frac{1}{I_k} + \frac{1}{B\omega^{1/2}} \tag{1.6}$$

$$B = 0.62nFAC_O D_O^{2/3} \nu^{-1/6} \tag{1.7}$$

$$I_k = nAFkC_O \tag{1.8}$$

where ω is the electrode rotation rate, n is electron-transfer number, F is the Faraday constant (96485 C mol^{-1}), A is the geometric surface area of the electrode, C_O is the oxygen concentration in O_2-saturated solutions (1.26×10^{-6} mol/cm^3),[58] D_O is the diffusion coefficient of O_2 in 0.1 M NaOH aqueous solution (1.93×10^{-5} cm^2/s),[59] v is the kinematic viscosity of the solution (1.009×10^{-2} cm^2/s), [60] and k is the electron-transfer rate constant.

The so-called K–L plots depict I_D^{-1} versus $\omega^{-½}$ and allow for the determination of the kinetic current for a given applied potential. This kinetic current is one of the best descriptors of electrocatalytic activity and is normalized to mass and electrochemical surface to yield the mass activity (J_m) and the specific activity (J_s).

Additionally, the ring electrode can help in identifying the pathway of electroreduction. During the potential sweep and rotation of the disk electrode, the ring electrode is held at a constant potential while the rotation pushes solution from the center of the disk electrode outward to the ring as can be seen in Figure 1.3 B. With a potential sufficiently positive, the ring can detect and hydrogen peroxide generated at the disk electrode by oxidizing it back to oxygen once forced outward. A large ring response signifies the incomplete, 2 electron reduction to H_2O_2 rather than the 4 electron reduction to H_2O. Not only does this yield less energy, but H_2O_2 may also damage the selective membrane. To quantitatively analyze the amount of each produced, equation 1.9 is used to calculate n, the number of electrons transferred. Here, N is collection efficiency of the electrode (40 %).[21]

$$n = 4\, I_D \Big/ (I_D + {}^{I_R}\!/_{N}) \qquad (1.9)$$

This value will be in between 2 and 4 with the higher the number representing more conversion to water as a product.

1.5 Alloy Nanoparticles

Among the pathways of interfacial manipulation, alloying with a second metal serves to alter the electronic structure of surface atoms by imparting lateral force on the particle lattice [61] as well driving electron rearrangements between neighboring atoms with different d band filling and electronegativity [47,62]. Both situations will ultimately alter the d band structure of the surface metal and thus the degree of filling for the metal-adsorbate antibonding state and strength of adsorptive interaction. The

d-band model is well established and has allowed for many predictions and rationalizations of enhanced alloy nanoparticles. Consequently, a great deal of effort has been devoted to alloy cathode catalysts, which can be classified into Pt-based alloy catalysts [46,47,62,63] and non-Pt alloy catalysts [64].

One non-Pt bimetallic alloy that is of interest as an effective electrocatalyst for oxygen reduction is a palladium and gold alloy. Although not as active as pure platinum, pure palladium exhibits good electrocatalytic oxygen reduction activity and is similarly limited by strong interactions with adsorbed oxygen resulting in surface blockage and inactivity. Again, this relates to the high d band center of both palladium and platinum (Figure 1.2).[65] Conversely, gold exhibits a lower d band center relative the fermi level and does not interact appreciably with oxygen.[66] The goal of chapter 4 is to synthesize alloy nanoparticles consisting of gold and palladium in varying atomic ratios to determine the optimal ratio for catalytic oxygen reduction and to improve upon the platinum standard.

1.6 Graphene Quantum Dots as Active Supports

The utilization of graphene quantum dots (GQD) as an active support is an effective method to alter surface properties of neighboring metal nanoparticles.[25,27] Graphene quantum dots are nanosized fragments of graphite a few layers thick and diameter on the nanometer scale. GQDs can be synthesized through either a top-down method where larger pieces of graphite are cleaved to the nanoscale or by a bottom-up method where atomic or molecular sources of carbon are linked together.[13,67] In either case, when synthesized in the presence of oxygen, GQDs will

generally contain copious amounts of various oxygen-containing functional groups allowing facile solvation in water. Although commonly viewed as defects in the graphitic backbone, these groups have been found to anchor metal nanoparticles and, even more, provide a source of electron density withdrawal from the particles.[39] As electrocatalytic applications require a high surface area conducting support, GQDs are a great candidate to act as an electrical contact and support for the metal nanoparticles but, more importantly, to act as a source of electronic and thus activity modulation. This significant electronic interaction between support and nanoparticle is what separates a passive support from an active support. Furthermore, the concentration of oxygen defects has been shown to be easily manipulated by means of thermal treatment. In fact, modulated oxygen reduction activity has been observed for GQD supported platinum nanoparticles.[27]

The focus of the study detailed in chapter 5 is to control defect level through thermal treatment for palladium nanoparticle GQD composites in order to optimize conditions for electrocatalytic oxygen reduction. Not only do we hope to improve on the activity of current electrocatalyst, we hope this work may add to the development of the theory connecting characteristics of an organic ligand to the strength of adsorbate interaction, similar to that for alloy nanoparticles, by demonstrating a clear connection between defect level, electronic environment of the palladium nanoparticle, and electrocatalytic activity.

1.7 Nitrogen Doped Graphene Quantum Dots as Active Supports

While the manipulation of the oxygenated defects of GQDs has afforded control over the activity of associated platinum, palladium and copper nanoparticles, the rather high level of defects required for optimal activity, especially for metals like palladium with very high d band centers, will likely diminish the conductivity and compromise the eventual performance. [25,27,68] A promising alternative is the incorporation of heteroatoms into the graphitic structure, in particular, nitrogen.[69-72]

The incorporation of nitrogen into the graphitic backbone has been accomplished through many methods and has provided varying degrees of enhancement in oxygen reduction activity depending on the specific of the nitrogen incorporation. Besides the level of nitrogen content, which too has profound consequences, nitrogen may exist as pyrrolic, pyridinic, or quaternary centers within the graphitic structure and will affect the particles differently.[13,73] The focus of chapter 6 is determining the relationship between synthetic conditions, the nitrogen center types, the metal nanoparticles electronic environment, and the resulting electrocatalytic activity.

1.7 References

(1) Ahn, H.; Chandekar, A.; Kang, B.; Sung, C.; Whitten, J. E.: Electrical conductivity and vapor-sensing properties of omega-(3-thienyl)alkanethiol-protected gold nanoparticle films. *Chem Mater* **2004**, *16*, 3274-3278.

(2) Garcia-Berrios, E.; Gao, T.; Woodka, M. D.; Maldonado, S.; Brunschwig, B. S.; Ellsworth, M. W.; Lewis, N. S.: Response versus Chain Length of Alkanethiol-Capped Au Nanoparticle Chemiresistive Chemical Vapor Sensors. *J Phys Chem C* **2010**, *114*, 21914-21920.

(3) Chen, W.; Zuckerman, N. B.; Lewis, J. W.; Konopelski, J. P.; Chen, S. W.: Pyrene-Functionalized Ruthenium Nanoparticles: Novel Fluorescence Characteristics from Intraparticle Extended Conjugation. *J Phys Chem C* **2009**, *113*, 16988-16995.

(4) Li, D. D.; Liu, Z. Q.; Liu, X.; Wu, X. L.; Ji, G. Q.: Silver Doped TiO2 Nanotube Arrays: Preparation and Photoelectric Catalysis Degradation of Ammonia Nitrogen Wastewater. *Chinese J Inorg Chem* **2012**, *28*, 1343-1347.

(5) Das, S., Muneer, M., Gopidas, K. R.: Photocatalytic degradation of wastewater pollutants. Titanium-dioxide-mediated oxidation of polynuclear aromatic hydrocarbons. *J. Photochem. Photobiol. A: Chem.* **1994**, *77*, 83-88.

(6) Ponec, V.: Surface Composition and Catalysis on Alloys. *Surf Sci* **1979**, *80*, 352-366.

(7) Haruta, M.: Spiers Memorial Lecture : Role of perimeter interfaces in catalysis by gold nanoparticles. *Faraday Discuss* **2011**, *152*, 11.

(8) Zhou, Z. Y.; Kang, X. W.; Song, Y.; Chen, S. W.: Butylphenyl-functionalized palladium nanoparticles as effective catalysts for the electrooxidation of formic acid. *Chem Commun* **2011**, *47*, 6075-6077.
(9) Zhou, Z. Y.; Ren, J.; Kang, X.; Song, Y.; Sun, S. G.; Chen, S.: Butylphenyl-functionalized Pt nanoparticles as CO-resistant electrocatalysts for formic acid oxidation. *Phys Chem Chem Phys* **2012**, *14*, 1412-7.

(10) Chen, W.; Ny, D.; Chen, S.: SnO2–Au hybrid nanoparticles as effective catalysts for oxygen electroreduction in alkaline media. *J Power Sources* **2010**, *195*, 412-418.

(11) Chen, W.; Chen, S.: Oxygen electroreduction catalyzed by gold nanoclusters: strong core size effects. *Angewandte Chemie* **2009**, *48*, 4386-9.

(12) Kosowska, B.; Mozia, S.; Morawski, A. W.; Grzmil, B.; Janus, M.; Kalucki, K.: The preparation of TiO2-nitrogen doped by calcination of TiO2 center dot xH(2)O under ammonia atmosphere for visible light photocatalysis. *Sol Energ Mat Sol C* **2005**, *88*, 269-280.

(13) Qu, D.; Zheng, M.; Du, P.; Zhou, Y.; Zhang, L.; Li, D.; Tan, H.; Zhao, Z.; Xie, Z.; Sun, Z.: Highly luminescent S, N co-doped graphene quantum dots with broad visible absorption bands for visible light photocatalysts. *Nanoscale* **2013**, *5*, 12272-7.

(14) An, T.; Li, G.; Zhu, X.; Fu, J.; Sheng, G.; Kun, Z.: Photoelectrocatalytic degradation of oxalic acid in aqueous phase with a novel three-dimensional electrode-hollow quartz tube photoelectrocatalytic reactor. *Applied Catalysis A: General* **2005**, *279*, 247-256.

(15) Sun, H. J.; Gao, N.; Wu, L.; Ren, J. S.; Wei, W. L.; Qu, X. G.: Highly Photoluminescent Amino-Functionalized Graphene Quantum Dots Used for Sensing Copper Ions. *Chem-Eur J* **2013**, *19*, 13362-13368.

(16) Stephens, I. E. L.; Bondarenko, A. S.; Grønbjerg, U.; Rossmeisl, J.; Chorkendorff, I.: Understanding the electrocatalysis of oxygen reduction on platinum and its alloys. *Energ Environ Sci* **2012**, *5*, 6744.

(17) Rabis, A.; Rodriguez, P.; Schmidt, T. J.: Electrocatalysis for Polymer Electrolyte Fuel Cells: Recent Achievements and Future Challenges. *Acs Catal* **2012**, *2*, 864-890.

(18) Hu, P. G.; Song, Y.; Chen, L. M.; Chen, S. W.: Electrocatalytic activity of alkyne-functionalized AgAu alloy nanoparticles for oxygen reduction in alkaline media. *Nanoscale* **2015**, *7*, 9627-9636.

(19) Kang, X. W.; Song, Y.; Chen, S. W.: Nitrene-functionalized ruthenium nanoparticles. *J Mater Chem* **2012**, *22*, 19250-19257.

(20) Zhang, S.; Shao, Y.; Yin, G.; Lin, Y.: Facile synthesis of PtAu alloy nanoparticles with high activity for formic acid oxidation. *J Power Sources* **2010**, *195*, 1103-1106.

(21) Zhou, Z. Y.; Kang, X.; Song, Y.; Chen, S.: Enhancement of the electrocatalytic activity of Pt nanoparticles in oxygen reduction by chlorophenyl functionalization. *Chem Commun (Camb)* **2012**, *48*, 3391-3.

(22) Hernandez, J.; Solla-Gullon, J.; Herrero, E.; Aldaz, A.; Feliu, J. M.: Electrochemistry of shape-controlled catalysts: Oxygen reduction reaction on cubic gold nanoparticles. *J Phys Chem C* **2007**, *111*, 14078-14083.

(23) Wu, J.; Zhang, J.; Peng, Z. M.; Yang, S. C.; Wagner, F. T.; Yang, H.: Truncated Octahedral Pt3Ni Oxygen Reduction Reaction Electrocatalysts. *J Am Chem Soc* **2010**, *132*, 4984-4985.

(24) Park, S.; Xie, Y.; Weaver, M. J.: Electrocatalytic pathways on carbon-supported platinum nanoparticles: Comparison of particle-size-dependent rates of methanol, formic acid, and formaldehyde electrooxidation. *Langmuir* **2002**, *18*, 5792-5798.

(25) He, G. Q.; Song, Y.; Liu, K.; Walter, A.; Chen, S.; Chen, S. W.: Oxygen Reduction Catalyzed by Platinum Nanoparticles Supported on Graphene Quantum Dots. *Acs Catal* **2013**, *3*, 831-838.

(26) Zhou, Z. Y.; Kang, X. W.; Song, Y.; Chen, S. W.: Ligand-Mediated Electrocatalytic Activity of Pt Nanoparticles for Oxygen Reduction Reactions. *J Phys Chem C* **2012**, *116*, 10592-10598.

(27) Song, Y.; Chen, S. W.: Graphene Quantum-Dot-Supported Platinum Nanoparticles: Defect-Mediated Electrocatalytic Activity in Oxygen Reduction. *Acs Appl Mater Inter* **2014**, *6*, 14050-14060.

(28) Song, Y.; Klivansky, L. M.; Liu, Y.; Chen, S.: Enhanced stability of Janus nanoparticles by covalent cross-linking of surface ligands. *Langmuir* **2011**, *27*, 14581-8.

(29) Kang, X. W.; Chen, S. W.: Electronic conductivity of alkyne-capped ruthenium nanoparticles. *Nanoscale* **2012**, *4*, 4183-4189.

(30) Wang, G. N. R.; Wang, L. Y.; Qiang, R. D.; Wang, J. G.; Luo, J.; Zhong, C. J.: Correlation between nanostructural parameters and conductivity properties for molecularly-mediated thin film assemblies of gold nanoparticles. *J Mater Chem* **2007**, *17*, 457-462.

(31) Terrill, R. H.; Postlethwaite, T. A.; Chen, C. H.; Poon, C. D.; Terzis, A.; Chen, A. D.; Hutchison, J. E.; Clark, M. R.; Wignall, G.; Londono, J. D.; Superfine, R.; Falvo, M.; Johnson, C. S.; Samulski, E. T.; Murray, R. W.: Monolayers in three dimensions: NMR, SAXS, thermal, and electron hopping studies of alkanethiol stabilized gold clusters. *J Am Chem Soc* **1995**, *117*, 12537-12548.

(32) Cano-Castillo, U.: Hydrogen and Fuel Cells: Potential Elements in the Energy Transition Scenario. *Rev Mex Fis* **2013**, *59*, 85-92.

(33) Hamrock, S. J.; Herring, A. M.; Zawodzinski, T. A.: Fuel cell chemistry and operation. *J Power Sources* **2007**, *172*, 1.

(34) Dhathathreyan, K. S.; Sridhar, P.; Sasikumar, G.; Ghosh, K. K.; Velayutham, G.; Rajalakshmi, N.; Subramaniam, C. K.; Raja, M.; K., R.: Development of polymer electrolyte membrane fuel cell stack. *Int J Hydrogen Energ* **1999**, *24*, 1107-1115.

(35) Borup, R.; Meyers, J.; Pivovar, B.; Kim, Y. S.; Mukundan, R.; Garland, N.; Myers, D.; Wilson, M.; Garzon, F.; Wood, D.; Zelenay, P.; More, K.; Stroh, K.; Zawodzinski, T.; Boncella, J.; McGrath, J. E.; Inaba, M.; Miyatake, K.; Hori, M.; Ota, K.; Ogumi, Z.; Miyata, S.; Nishikata, A.; Siroma, Z.; Uchimoto, Y.; Yasuda, K.; Kimijima, K. I.; Iwashita, N.: Scientific aspects of polymer electrolyte fuel cell durability and degradation. *Chem Rev* **2007**, *107*, 3904-3951.

(36) Wagner, F. T.; Lakshmanan, B.; Mathias, M. F.: Elecrochemistry and the Future of the Automobile. *The Journal of Physical Chemistry Letters* **2010**, 2204-2219.

(37)Norskov, J. K.; Rossmeisl, J.; Logadottir, A.; Lindqvist, L.; Kitchin, J. R.; Bligaard, T.; Jonsson, H.: Origin of the Overpotential for Oxygen Reduction at a Fuel-Cell Cathode. *J Phys Chem B* **2004**, *108*, 17886-17892.

(38) Song, C.; Zhang, J.: *PEM Fuel Cell Electrocatalysis and Catalyst Layers: Fundamentals and Applications*, 2008.

(39) Lim, D. H.; Wilcox, J.: Mechanisms of the Oxygen Reduction Reaction on Defective Graphene-Supported Pt Nanoparticles from First-Principles. *J Phys Chem C* **2012**, *116*, 3653-3660.

(40) Sabatier, P.: Announcement. Hydrogenation and dehydrogenation for catalysis. *Ber Dtsch Chem Ges* **1911**, *44*, 1984-2001.

(41) Lee, C.-L.; Chiou, H.-P.; Syu, C.-M.; Wu, C.-C.: Silver triangular nanoplates as electrocatalyst for oxygen reduction reaction. *Electrochem Commun* **2010**, *12*, 1609-1613.

(42) Ham, D. J.; Phuruangrat, A.; Thongtem, S.; Lee, J. S.: Hydrothermal synthesis of monoclinic WO3 nanoplates and nanorods used as an electrocatalyst for hydrogen evolution reactions from water. *Chem Eng J* **2010**, *165*, 365-369.

(43) Shao, M.; Odell, J.; Humbert, M.; Yu, T.; Xia, Y.: Electrocatalysis on Shape-Controlled Palladium Nanocrystals: Oxygen Reduction Reaction and Formic Acid Oxidation. *The Journal of Physical Chemistry C* **2013**, *117*, 4172-4180.

(44) Carpenter, M. K.; Moylan, T. E.; Kukreja, R. S.; Atwan, M. H.; Tessema, M. M.: Solvothermal synthesis of platinum alloy nanoparticles for oxygen reduction electrocatalysis. *J Am Chem Soc* **2012**, *134*, 8535-42.

(45) Seo, A.; Lee, J.; Han, K.; Kim, H.: Performance and stability of Pt-based ternary alloy catalysts for PEMFC. *Electrochim Acta* **2006**, *52*, 1603-1611.

(46) Stamenkovic, V. R.; Mun, B. S.; Arenz, M.; Mayrhofer, K. J. J.; Lucas, C. A.; Wang, G. F.; Ross, P. N.; Markovic, N. M.: Trends in electrocatalysis on extended and nanoscale Pt-bimetallic alloy surfaces. *Nat Mater* **2007**, *6*, 241-247.

(47) Kitchin, J. R.; Norskov, J. K.; Barteau, M. A.; Chen, J. G.: Modification of the surface electronic and chemical properties of Pt(111) by subsurface 3d transition metals. *J Chem Phys* **2004**, *120*, 10240-6.

(48) Zhou, W. J.; Li, M.; Ding, O. L.; Chan, S. H.; Zhang, L.; Xue, Y. H.: Pd particle size effects on oxygen electrochemical reduction. *Int J Hydrogen Energ* **2014**, *39*, 6433-6442.

(49) Shao, M. H.; Peles, A.; Shoemaker, K.: Electrocatalysis on Platinum Nanoparticles: Particle Size Effect on Oxygen Reduction Reaction Activity. *Nano Lett* **2011**, *11*, 3714-3719.

(50) Liu, Y.; Zhang, L.; Willis, B. G.; Mustain, W. E.: Importance of Particle Size and Distribution in Achieving High-Activity, High-Stability Oxygen Reduction Catalysts. *Acs Catal* **2015**, *5*, 1560-1567.

(51) Kim, J. W.; Lim, B.; Jang, H. S.; Hwang, S. J.; Yoo, S. J.; Ha, J. S.; Cho, E. A.; Lim, T. H.; Nam, S. W.; Kim, S. K.: Size-controlled synthesis of Pt nanoparticles and their electrochemical activities toward oxygen reduction. *Int J Hydrogen Energ* **2011**, *36*, 706-712.

(52) Liu, K.; Kang, X.; Zhou, Z.-Y.; Song, Y.; Lee, L. J.; Tian, D.; Chen, S.: Platinum nanoparticles functionalized with acetylene derivatives: Electronic conductivity and electrocatalytic activity in oxygen reduction. *J Electroanal Chem* **2013**, *688*, 143-150.

(53) He, G.; Song, Y.; Phebus, B.; Liu, K.; Deming, C. P.; Hu, P.; Chen, S.: Electrocatalytic Activity of Organically Functionalized Silver Nanoparticles in Oxygen Reduction. *Sci Adv Mater* **2013**, *5*, 1727-1736.

(54) Pietron, J. J.; Garsany, Y.; Baturina, O.; Swider-Lyons, K. E.; Stroud, R. M.; Ramaker, D. E.; Schull, T. L.: Electrochemical Observation of Ligand Effects on Oxygen Reduction at Ligand-Stabilized Pt Nanoparticle Electrocatalysts. *Electrochemical and Solid-State Letters* **2008**, *11*, B161.

(55) Wu, Z. S.; Yang, S. B.; Sun, Y.; Parvez, K.; Feng, X. L.; Mullen, K.: 3D Nitrogen-Doped Graphene Aerogel-Supported Fe3O4 Nanoparticles as Efficient Eletrocatalysts for the Oxygen Reduction Reaction. *J Am Chem Soc* **2012**, *134*, 9082-9085.

(56) Liang, Y. Y.; Li, Y. G.; Wang, H. L.; Zhou, J. G.; Wang, J.; Regier, T.; Dai, H. J.: Co3O4 nanocrystals on graphene as a synergistic catalyst for oxygen reduction reaction. *Nat Mater* **2011**, *10*, 780-786.

(57) Jia, J. C.; Wang, H.; Ji, S.; Yang, H. J.; Li, X. S.; Wang, R. F.: SnO2-embedded worm-like carbon nanofibers supported Pt nanoparticles for oxygen reduction reaction. *Electrochim Acta* **2014**, *141*, 13-19.

(58) Schumpe, A.; Adler, I.; Deckwer, W. D.: Solubility of Oxygen in Electrolyte-Solutions. *Biotechnology and Bioengineering* **1978**, *20*, 145-150.

(59) Anastasijevic, N. A.; Dimitrijevic, Z. M.; Adzic, R. R.: Oxygen reduction on a ruthenium electrode in alkaline electrolytes. **1886**, 351.

(60) Markovic, N. M.; Gasteiger, H. A.; Grgur, B. N.; Ross, P. N.: Oxygen reduction reaction on Pt(111): effects of bromide. *Journal of Electroanalytical Chemistry* **1999**, *467*, 157-163.

(61) Strasser, P.; Koh, S.; Anniyev, T.; Greeley, J.; More, K.; Yu, C. F.; Liu, Z. C.; Kaya, S.; Nordlund, D.; Ogasawara, H.; Toney, M. F.; Nilsson, A.: Lattice-strain control of the activity in dealloyed core-shell fuel cell catalysts. *Nature Chemistry* **2010**, *2*, 454-460.

(62) Stephens, I. E.; Bondarenko, A. S.; Perez-Alonso, F. J.; Calle-Vallejo, F.; Bech, L.; Johansson, T. P.; Jepsen, A. K.; Frydendal, R.; Knudsen, B. P.; Rossmeisl, J.; Chorkendorff, I.: Tuning the activity of Pt(111) for oxygen electroreduction by subsurface alloying. *J Am Chem Soc* **2011**, *133*, 5485-91.

(63) Stamenkovic, V. R.; Fowler, B.; Mun, B. S.; Wang, G.; Ross, P. N.; Lucas, C. A.; Markovic, N. M.: Improved oxygen reduction activity on Pt3Ni(111) via increased surface site availability. *Science* **2007**, *315*, 493-7.

(64) Shao, M. H.; Sasaki, K.; Adzic, R. R.: Pd-Fe nanoparticles as electrocatalysts for oxygen reduction. *J Am Chem Soc* **2006**, *128*, 3526-3527.

(65) Wertheim, G. K.; DiCenzo, S. B.; Buchanan, D. N. E.: Noble- and transition-metal clusters: Thedbands of silver and palladium. *Phys Rev B* **1986**, *33*, 5384-5390.

(66) Rand, D. A. J.; Woods, R.: The Nature of Adsorbed Oxygen on Rhodium, Palladium, and Gold Electrodes. *J Electroanal Chem* **1971**, *31*, 29-38.

(67) Peng, J.; Gao, W.; Gupta, B. K.; Liu, Z.; Romero-Aburto, R.; Ge, L.; Song, L.; Alemany, L. B.; Zhan, X.; Gao, G.; Vithayathil, S. A.; Kaipparettu, B. A.; Marti, A. A.; Hayashi, T.; Zhu, J. J.; Ajayan, P. M.: Graphene quantum dots derived from carbon fibers. *Nano Lett* **2012**, *12*, 844-9.

(68) Deming, C. P.; Mercado, R.; Gadiraju, V.; Sweeney, S. W.; Khan, M.; Chen, S.: Graphene Quantum Dots-Supported Palladium Nanoparticles for Efficient Electrocatalytic Reduction of Oxygen in Alkaline Media. *Acs Sustain Chem Eng* **2015**, *3*, 3315-3323.

(69) Jafri, R. I.; Rajalakshmi, N.; Ramaprabhu, S.: Nitrogen doped graphene nanoplatelets as catalyst support for oxygen reduction reaction in proton exchange membrane fuel cell. *J Mater Chem* **2010**, *20*, 7114-7117.

(70) Yu, D. B.; Yao, J. F.; Qiu, L.; Wu, Y. Z.; Li, L. X.; Feng, Y.; Liu, Q.; Li, D.; Wang, H. T.: The synergetic effect of N-doped graphene and silver nanowires for high electrocatalytic performance in the oxygen reduction reaction. *Rsc Adv* **2013**, *3*, 11552-11555.

(71) Liu, X.; Li, L.; Meng, C.; Han, Y.: Palladium Nanoparticles/Defective Graphene Composites as Oxygen Reduction Electrocatalysts: A First-Principles Study. *The Journal of Physical Chemistry C* **2012**, *116*, 2710-2719.

(72) Bai, J. C.; Zhu, Q. Q.; Lv, Z. X.; Dong, H. Z.; Yu, J. H.; Dong, L. F.: Nitrogen-doped graphene as catalysts and catalyst supports for oxygen reduction in both acidic and alkaline solutions. *Int J Hydrogen Energ* **2013**, *38*, 1413-1418.

(73) Deng, D.; Pan, X.; Yu, L.; Cui, Y.; Jiang, Y.; Qi, J.; Li, W.-X.; Fu, Q.; Ma, X.; Xue, Q.; Sun, G.; Bao, X.: Toward N-Doped Graphene via Solvothermal Synthesis. *Chem Mater* **2011**, *23*, 1188-1193.

Chapter 2

Experimental

2.1 Chemicals

Ruthenium chloride ($RuCl_3$, 99+%, ACROS), 1,2-propanediol(ARCOS), sodium acetate trihydrate ($NaOAc \cdot 3H_2O$, MC&B), vinyl-ferrocene (97%, Sigma-Aldrich), tetra-n-butyl ammonium nitrate($TBANO_3$, ≥99%, Sigma-Aldrich), and 4-dodecylbenzenesulfonylazide (Aldrich), tetrachloroauric acid trihydrate ($HAuCl_4 \cdot 3H_2O$, Acros), palladium chloride ($PdCl_2$, Acros), hydrochloric acid (HCl, certified ACS Plus, Fisher Scientific), tetra-n-octylammonium bromide (TOABr, 98%, Acros), 1-dodecyne (97 %, Alpha Aesar), sodium borohydride ($NaBH_4$, 98%, Acros), Nafion 117 Solution (5 %, Fluka), carbon black (XC-72R, Fuel Cell Store), palladium black (99.95%, Sigma Aldrich), and sodium bicarbonate ($NaHCO_3$, 99.7%, Fisher Scientific), pitch carbon fibers (Fiber Glast Development corporation), sodium hydroxide (NaOH, ≥ 99.5%, Fisher Scientific), sodium carbonate (Na_2CO_3, ≥ 99.5%, Fisher Scientific), perchloric acid ($HClO_4$, 70 wt %, ACROS), sulfuric acid (H_2SO_4, Fisher Scientific), nitric acid (HNO_3, Fisher Scientific), and ultrahigh-purity nitrogen and oxygen (99.993%, Praxair), citric acid (anhydrous, 99%, Acros), urea (98%, Acros). All solvents were obtained from typical commercial sources and used without further treatment. All chemicals used as received. Water was supplied by a Barnstead Nanopure water system (18.3 Ω-cm).

2.2 Synthetic Techniques

2.2.1 Nitrene Capped Ruthenium Nanoparticles

The synthesis of the nitrene-functionalized ruthenium (Ru=N) nanoparticles has been detailed previously.[1] In brief, ruthenium chloride (0.14 mmol) and sodium

acetate (80 mg) were dissolved in 100 mL of 1,2-propanediol. The mixture was then refluxed at 165 ˚C under magnetic stirring for 1 h to allow for the reduction of the ruthenium salt into acetate-protected ruthenium colloids. The solution was then cooled down to 60˚C, and 0.52 mmol of dodecylbenzenesulfonyl azide and 20 mL of sec-butylbenzene were added to the solution which was then stirred for 1 h with the temperature maintained at 60˚C. Adsorption of the azide ligands onto the ruthenium colloids resulted in a phase transfer from 1,2-propanediol to sec-butylbenzene. The sec-butylbenzene phase was then collected and refluxed at 165˚C for 24 h where nitrene radicals were generated and attached onto the ruthenium colloid surface forming Ru=N bonds. The solution was then cooled down to room temperature and solvents were removed by a rotary evaporator. The particles were then rinsed extensively with acetonitrile to remove excessive ligands and the resulting particles remained stable and soluble in apolar solvents such as toluene, THF, chloroform, and dichloromethane, but insoluble in alkanes, ethanol or acetone.

2.2.2 Gold Palladium Alloy Nanoparticles

The biphasic route towards the preparation of organically capped gold nanoparticles was adopted for the synthesis of dodecyne capped AuPd alloy nanoparticles.[2] In a typical reaction, palladium chloride was first dissolved in concentrated HCl to prepare tetrachloropalladic acid (H_2PdCl_4), which was then mixed with tetrachloroauric acid ($HAuCl_4$) at a selected molar feed ratio (0.15 mmol in total) in 20 mL of water under magnetic stirring. The solution was then transferred into a 50 mL round-bottom flask, into which tetraoctylammonium bromide (0.45

mmol) dissolved in toluene was added, resulting in phase transfer of the metal complexes to the organic phase, as manifested by a clear aqueous layer in the bottom and the formation of a burgundy color in the top organic phase. The organic phase was then collected by using a separatory funnel and transferred to a round-bottom flask, into which 1-dodecyne (0.45 mmol) was then added. A freshly prepared solution of sodium borohydride (1.2 mmol) in chilled water was added dropwise into the solution under vigorous magnetic stirring. An immediate change of the solution color from burgundy to dark red/brown, depending on the relative content of palladium and gold signified the formation of AuPd alloy nanoparticles. Water was then used to wash away residual salts with a separatory funnel, and rotary evaporation was used to condense the toluene layer to less than 0.5 mL. Addition of a large excess of methanol led to apparent precipitation of the nanoparticles from the solution, which were collected by centrifugation. The procedure was repeated several times to remove free ligands and other reaction byproducts. The resulting particles were soluble in nonpolar organic media such as CH_2Cl_2, THF, and toluene, and referred to as AuPdHC12. Six nanoparticle samples were prepared with the Pd atomic fraction varied from approximately 65 to 100%, as determined by X-ray photoelectron spectroscopic (XPS) measurements (vide infra).

2.2.3 Graphene Quantum Dots

The synthesis of GQDs has been detailed previously.[3,4] Experimentally, carbon pitch fibers (1 g) were added to a mixture of concentrated HNO_3 (40 mL) and H_2SO_4 (60 mL) in a round-bottomed flask. Two hours of sonication allowed for

proper dispersion of these tightly woven carbon fibers in the acids followed by thermal refluxing at 110 °C for 24 h. When the solution was cooled to room temperature, the solution pH was adjusted to 7 with NaOH. The solution was then left overnight where the supersaturated salts precipitated out of the solution with GQDs dissolved in the water supernatant. The water phase was then loaded into cellulose dialysis bags and placed in Nanopure water for several days to afford purified GQDs that were about 20 nm in diameter and 2 nm in thickness (corresponding to 5−6 layers of graphene sheets. These water-soluble GQDs were then used for the preparation of Pd/GQD nanocomposites, as described below.

2.2.4 Palladium Nanoparticle Graphene Quantum Dot Composites

$PdCl_2$ (30 mg) was first dissolved in 1 mL of concentrated HCl, and the solution pH was brought to neutral with the addition of Na_2CO_3, followed by centrifugation and removal of residual precipitates. The solution was then added to a flask containing propylene glycol (20 mL) and GQDs prepared above (20 mg) under magnetic stirring. With continuous nitrogen bubbling, the solution was slowly brought to 80 °C and heated at this temperature for 2 h. Complete deposition of palladium on the GQDs was signified by a change in the solution color from dark black to clear and the formation of a dark precipitate at the bottom of the flask. The precipitate was collected and purified with water and underwent centrifugation to remove unreduced palladium and GQDs with little or no metal deposition. The purified samples were referred to as Pd/ GQD. The resulting Pd/GQD nanocomposites were added into 15 mL of water in a Teflon-lined autoclave, which

was sealed and hydrothermally treated for 12 h at a controlled temperature of 140, 160, 180, or 200 °C. The resulting particles remained insoluble in water and were denoted as Pd/GQD-T, where T represents the hydrothermal temperature.

2.2.5 Nitrogen Doped Quantum Dot Palladium Nanoparticle Composites

PdNGQD nanocomposites were synthesized by adopting a bottom-up procedure for NGQDs reported in the literature that involved hydrothermal treatment of citric acid and urea.[5] In a typical reaction, $PdCl_2$ (50 mg) was dissolved in 1 mL of concentrated HCl to form the water-soluble $PdCl_4^{2-}$complex, followed by neutralization with Na_2CO_3, and centrifugation to remove excess salts. The palladium solution was then condensed to 2.5 mL before being added to a Teflon autoclave liner. Citric acid (70 mg) and urea (60 mg) as well as 2.5 mL of propylene glycol were also added to the liner and all the salts were allowed to dissolve. Then the solution was heated at 160 °C for various periods of time (1, 4, 8, or 12 h), resulting in the formation of large, dark precipitates in the bottom of the liner. The precipitates were collected and purified extensively with water. The obtained samples were denoted as PdNGQD-t (with t being the heating time). Control experiments were also carried out where a stoichiometric amount (70 mg) of $RuCl_3$ was used instead of $PdCl_2$ while keeping other experimental conditions unchanged (heating for 8 hs), resulting in the formation of ruthenium nanoparticles supported on NGQD. The composite was denoted as RuNGQD. Additional controls were carried out where urea was replaced with a stoichiometric amount of citric acid, affording palladium

nanoparticles supported on nitrogen-free GQDs. These samples were referred to as PdGQD-t.

2.3 Instruments

2.3.1 Spectroscopy

UV–vis spectroscopic studies were performed with an ATI Unicam UV4 spectrometer using a 1 cm quartz cuvette at a resolution of 2 nm. Photoluminescence characteristics were examined with a PTI fluorospectrometer using the same 1 cm quartz cuvette at a resolution of 2 nm. 1H and 13C NMR spectroscopic measurements were carried out by using concentrated solutions of the nanoparticles in $CDCl_3$or CD_2Cl_2 with a Varian Unity 500 MHz NMR spectrometer. Raman spectroscopic measurements were carried out with a Delta NU 532 nm Raman spectrometer. X-ray photoelectron spectra (XPS) were recorded with a PHI 5400/XPS instrument equipped with an Al Kα source operated at 350 W and 10^{-9} Torr.

2.3.2 Microscopy

Transmission electron microscopic (TEM) studies were carried out with a Philips CM300 scope (300 kV). Samples were prepared by dropcasting a dispersion of the nanocomposites in ethanol onto a carbon-coated copper grid.

2.3.3 Electrochemistry

Electrochemical tests were carried out in a standard three-electrode cell connected to a CHI 710C electrochemical workstation, with a Pt foil counter electrode and a reversible hydrogen reference electrode (RHE). The working electrode is a rotating gold ring/glassy-carbon disk electrode (RRDE). A calculated

amount of the nanocomposites prepared above was dispersed in ethanol to prepare a catalyst ink, which was then slowly dropcast onto the glassy-carbon disk electrode of the RRDE and dried under gentle N_2. The catalyst films were then coated with 3 μL of a dilute Nafion solution (0.1 wt %) and dried in air.

2.3.4 Electronic Conductivity

For electronic conductivity measurements, a particle film was formed by drop casting 1 μL of a concentrated particle solution in toluene (ca. 60 mg/mL) onto an interdigitated array (IDA) electrode(25 pairs of gold fingers of 3 mm × 5 μm × 5 μm, from ABTECH). At least 30 min was allowed for solvent evaporation, and the film thickness was found to be greater than the height of the IDA fingers. Conductivity measurements were then carried out with the nanoparticle film sealed in a 20 mL vial where varied organic vapors were injected with a Hamilton microliter syringe at ambient temperature. In between each injection, the cell was purged with ultrahigh-purity nitrogen gas until a steady state was attained. The ensemble conductivity (σ) was evaluated by Eq. 2.1,

$$\sigma = \frac{1}{49R}\frac{L}{R} \tag{2.1}$$

where R is the ensemble resistance calculated from the slope of the I–V curves, L is the IDA electrode inter finger gap (5 μm), and A is the film cross-section area approximated by (finger height, 5 μm) × (finger length, 3 mm). The constant (49) reflects that there are totally 49 junctions which are in parallel within the IDA chip. Prior to exposure to any organic vapors, the electronic conductivity of the nanoparticle films was measured and denoted as σ_i. Exposure to organic vapors

changed the conductivity to σ. The variation of the normalized conductivity, which is defined as the ratio of σ/σ_i, with vapor concentration was then used to compare the sensitivity (S) of the nanoparticle ensembles to different organic vapors where S is the tangent of σ/σ_i vs. vapor concentration.

2.4 References

(1) Kang, X. W.; Song, Y.; Chen, S. W.: Nitrene-functionalized ruthenium nanoparticles. *J Mater Chem* **2012**, *22*, 19250-19257.

(2) Brust, M.; Walker, M.; Bethell, D.; Schiffrin, D. J.; Whyman, R.: Synthesis of Thiol-Derivatized Gold Nanoparticles in a 2-Phase Liquid-Liquid System. *Journal of the Chemical Society-Chemical Communications* **1994**, 801-802.

(3) He, G. Q.; Song, Y.; Liu, K.; Walter, A.; Chen, S.; Chen, S. W.: Oxygen Reduction Catalyzed by Platinum Nanoparticles Supported on Graphene Quantum Dots. *Acs Catal* **2013**, *3*, 831-838.

(4) Song, Y.; Chen, S. W.: Graphene Quantum-Dot-Supported Platinum Nanoparticles: Defect-Mediated Electrocatalytic Activity in Oxygen Reduction. *Acs Appl Mater Inter* **2014**, *6*, 14050-14060.

(5) Qu, D.; Zheng, M.; Du, P.; Zhou, Y.; Zhang, L.; Li, D.; Tan, H.; Zhao, Z.; Xie, Z.; Sun, Z.: Highly luminescent S, N co-doped graphene quantum dots with broad visible absorption bands for visible light photocatalysts. *Nanoscale* **2013**, *5*, 12272-7.

Chapter 3

Nitrene-Functionalized Ruthenium Nanoparticles: Selective Manipulation of Nanoparticle Electronic Conductivity by Vinyl Derivatives

3.1 Introduction

The functionalization of metal nanoparticles with organic molecules is one of the most commonly used methods for nanoparticle modification and has allowed for optimization of properties such as solubility, conductivity, absorption or emission of light and physical adsorptive properties.[1-5] The widespread use of organic functionalization is largely a result of facile self-assembly on metal surfaces displayed by many ligands but, more importantly, the large variety of available ligands, as well as the ease of modifying surface bound ligands has provided the necessary control over the nanoparticle properties .[6-12] That is, many ligands will spontaneously form monolayers on metal surfaces and the length, degree of branching, and substituent groups of a ligand may be chosen for a desired situation as well as altered once covalently bound to the particle.

Given the appropriate choice of metal surface and terminal ligand group, the ligands will spontaneously bond to the metal surface and form a monolayer with Van der Waals forces providing stability between neighboring ligands. The formation dynamics and properties of self-assembled monolayers (SAM) on metal surfaces have been extensively studied for both bulk and nanosized metal surfaces, perhaps most notably for the case of straight chain thiol ligands assembled on gold. The spontaneity of the monolayer formation under mild thermal and chemical conditions provides an easy method for deposition of a ligand monolayer without disturbing the metal core.[7]

Additionally, it has been widely observed that the details of the ligand composition have a profound impact on particle properties.[13-15] For example, aliphatic, straight chain carbon ligands provide facile solvation in non-polar solvents while ligands composed of polar, oxygenated moieties tend to dissolve more readily in polar solvents. More branched ligands or those with cyclic groups may impart more steric hindrance and pack less densely on the particle providing more exposed metal surface.[2] While the countless ligand choices provide a vast variety of environments for the functionalized particle, more interesting is the details of the bonding interaction between the organic ligand and the metal surface. Specifically, if the ligand contains a p orbital that does not undergo hybridization, then pi overlap is possible with the d orbitals of the metal allowing charge transfer across the metal interface.[5,12,16-18]

It is well known that pi overlap between neighboring atoms permits delocalization of electrons and that some d orbitals of metals, as well as p orbitals, contain the necessary geometry for electron cloud overlap. For aliphatic carbons and thiol groups, sp^3 hybridization results in orbital geometry incompatible with pi overlap and will not allow delocalized charge transfer. The atom of the ligand that is bonding to the metal surface will, therefore, require sp^2 or sp hybridization to obtain delocalization as is the case for terminal alkynes and alkanes. Furthermore, it has been found that terminal alkynes readily assemble on metal surfaces while alkenes have demonstrated monolayer assembly under moderate conditions The relative ease of synthesizing organic monolayer protected nanoparticles with conjugated metal

ligand interfaces has led to much research into the unprecedented optical and electronic properties resulting from facile charge transfer between the metal core and the protecting, organic ligands.[1,3,16,17,19]

For example, ruthenium nanoparticles protected by carbene fragments have shown interesting nanoparticle-mediated intervalence charge transfer between ferrocene-terminated carbene ligands on the particle surface, where the electron delocalization through the metal cores renders the particle-bound functional moieties to behave analogously to dimeric species.[4] Similar behaviors have also been observed with nitrene-functionalized nanoparticles where the nitrene fragments are prepared by controlled thermolysis of azide derivatives.[12] Interestingly, the ruthenium-nitrene interfacial bonds are found to exhibit unique chemical reactivity towards vinyl derivatives through imido transfer (Scheme 1).[12] Such a unique property may be exploited as a powerful variable in the further manipulation of interparticle charge transfer and hence nanoparticle film conductivity.

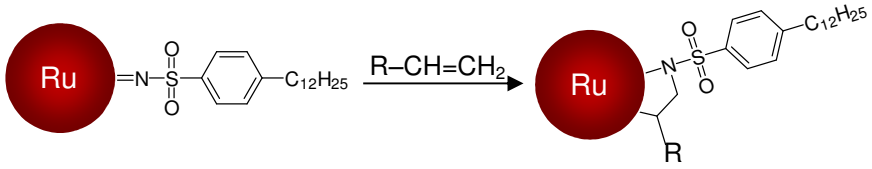

Scheme 3.1 Schematic of imido transfer reactions of nitrene-functionalized ruthenium nanoparticles with vinyl derivatives.

Films of organically capped metal nanoparticles have been widely used as vapor sensors due to a measureable change in electronic conductivity when exposed

to vapors of low concentrations.[20-22] In essence, these films consist of metal centers embedded in an organic framework of the capping ligands, and the electrons travel through the films by tunneling between metal centers with the organic ligands as the energy barriers. The effect is similar to charge transfer through a mixed valence system. Following this electron tunneling model as well as the Marcus theory, the ensemble conductivity may be defined by Eq. 3.1, [3,23,24]

$$\sigma(\delta,T) = \sigma_0 \exp(-\beta\delta)\exp(-\frac{E_a}{RT}) \tag{3.1}$$

where σ_0 is the intrinsic conductivity of the nanoparticle film based on the number and mobility of the charge carriers, β is the electronic coupling term, δ is the distance between particles, and E_a is the activation energy which is given by equation 3.2,

$$E_a = \frac{e^2}{8\pi\varepsilon\varepsilon_0}(\frac{1}{r} - \frac{1}{r+\delta}) \tag{3.2}$$

with r being the metal core radius. From these two equations, it is apparent that there are multiple parameters that may be exploited to alter the conductivity of the nanoparticle films. For instance, by increasing the interparticle distance the first exponential term in Eq. 3.1 will decrease and the activation energy (Eq. 3.2) will increase resulting in a loss of conductivity. An increase of the interparticle distance can be readily accomplished through solvation of the particles comprising the film. As the particles are solvated, the film will swell leading to larger interparticle distances and thus a larger barrier for electron tunneling and a lower overall conductivity. Such behaviors have been observed in a number of prior studies with solid films of gold nanoparticles functionalized with mercapto derivatives.[21,25]

However, in these studies, with nanoparticle solvation being the leading parameter in controlling the interparticle charge transfer, it is not surprising that the selectivity and sensitivity of the nanoparticle film conductivity towards organic vapors are rather limited.

One can envision that if the electron tunneling pathways and hence the electronic coupling can be selectively manipulated, the detection sensitivity and/or selectivity may be further enhanced with an apparent change of the ensemble intrinsic conductivity. This is rendered possible with the emergence of metal nanoparticles functionalized with conjugated metal–ligand interfacial bonds.[1,5,17,18] In principle, if exposure to an organic vapor leads to the conversion of the conjugated metal–ligand bonds to saturated ones, the ensemble conductivity will be altered significantly as a consequence of the change of the electron tunneling pathway. This will provide sensing based on the exact chemical makeup of the vapor rather than a general feature such as solvation properties, a major limitation of most prior research. Such selectivity is essential for proper sensing technology and is the primary motivation of this study, which is exemplified by the selective reactivity of nitrene-functionalized ruthenium nanoparticles towards vinyl derivatives, as a result of imido transfer reactions of the ruthenium-nitrene bonds with vinyl moieties (Scheme 3.1).

3.2 Results and Discussion

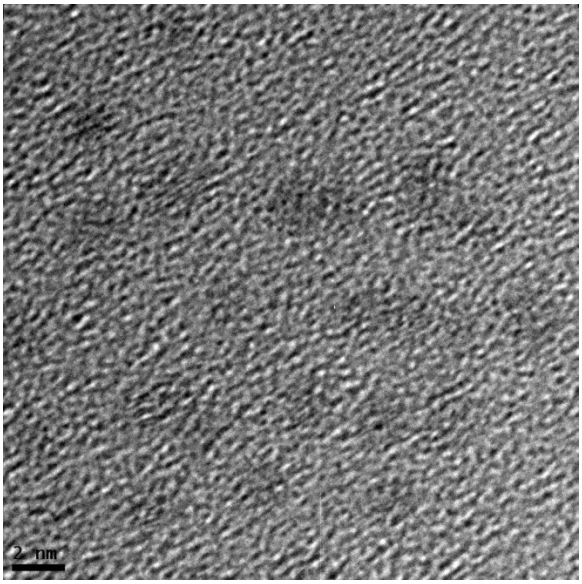

Figure 3.1. Representative TEM micrograph of Ru=N nanoparticles. Scale bar 2 nm.

Fig. 3.1 depicts a representative TEM micrograph of the Ru=N nanoparticles, where one can see that the nanoparticles are very well dispersed, suggesting good protection of the nanoparticles by the nitrene fragments. In addition, statistical analysis based on more than 100 nanoparticles shows that the average core diameter of the nanoparticles is 2.06 ± 0.31 nm.[26] The electronic conductivity of solid films of the nanoparticles was then measured and compared in the presence of various organic vapors that included a rather wide range of relative polarity, from apolar n-hexane,1-hexene, toluene, and styrene to polar acetone and ethanol.[27] Note that the Ru=N nanoparticles are not soluble in acetone or ethanol and only slightly soluble in n-hexane or 1-hexene, but are readily soluble in toluene and styrene. This means that solvation and swelling of the Ru=N nanoparticle solid films will be minimal when exposed to vapors of acetone, ethanol, n-hexane, and 1-hexene, whereas significant swelling is anticipated to occur when exposed to toluene and styrene. Fig. 3.2 depicts

the I–V profiles of the Ru=N solid films upon exposure to various organic vapors at different concentrations. It can be seen that the I–V curves all exhibited a linear correlation between the film current and applied potential, suggesting efficient interparticle charge transfer within the solid ensembles. Such a behavior has been observed extensively with nanoparticle solid ensembles and the ohmic characters were interpreted on the basis of a thermally activated hopping mechanism.[28,29] From the slopes, the electronic conductivity of the as-prepared particle films (black curves) can be estimated to be ca.1.0×10^{-5} S/m. This was about 12 orders of magnitude lower than that of metallic ruthenium (1.41×10^{7} S/m at 273 K) [30], which may be ascribed to the composite nature of the nanoparticles. Nevertheless, one may note that the Ru=N particle conductivity was very comparable to those observed with ruthenium nanoparticles functionalized with 1-alkynes of similar chain length, likely a result of the conjugated nature of the metal–ligand interfacial bonds in both cases that facilitated interparticle charge transfer.[3]

Furthermore, upon the exposure to different organic vapors, whereas the linearity of the I–V curves was preserved, the ensemble currents displayed a clear diminishment with increasing vapor concentrations, as highlighted by the dashed arrows in Fig. 3.2. Yet the sensitivity of the ensemble conductivity to vapor concentration was apparently different with the chemical nature of the organic vapors. Fig. 3.3 A summarizes the variation of the nanoparticle ensemble conductivity with vapor concentration. Note that the conductivity has been normalized to that prior to the exposure to any organic vapor. It can be seen that among the six organic vapors

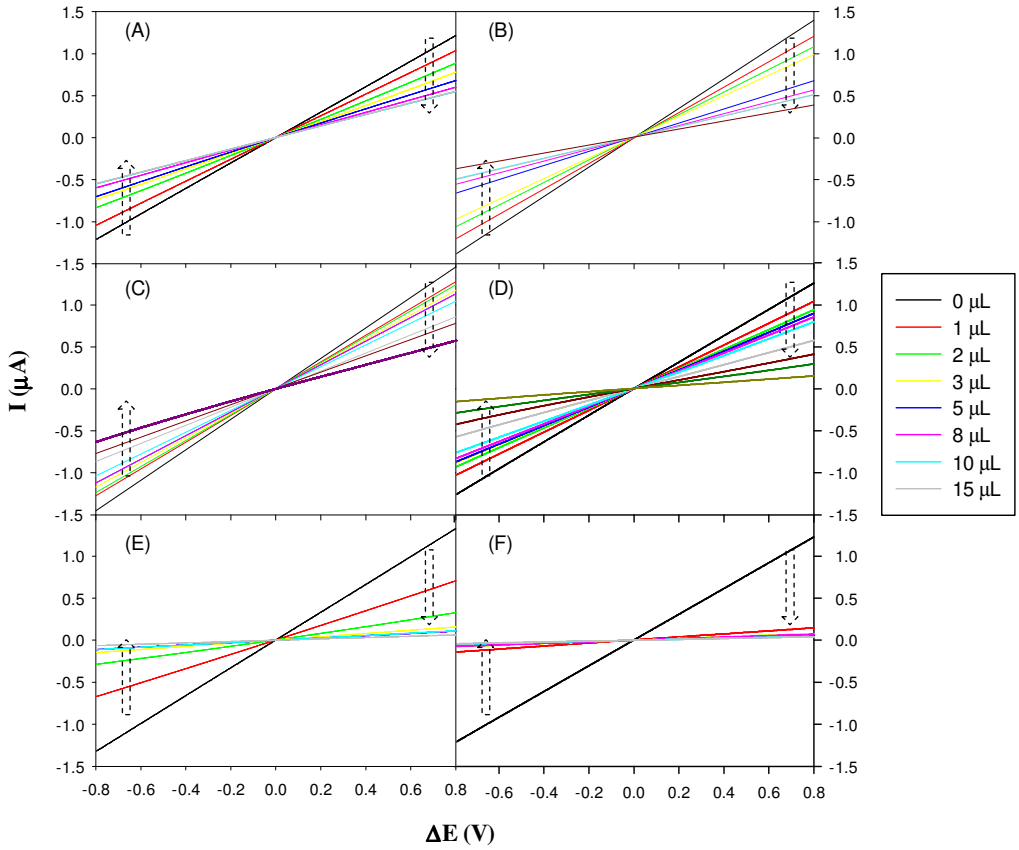

Figure 3.2. I-V curves of Ru=N nanoparticle solid films upon exposure to various organic vapors: (A) ethanol, (B) acetone, (C) n-hexane, (D) 1-hexene, I toluene, and (F) styrene. Dashed arrows highlight the diminishment of the ensemble conductance with the injection of increasing amounts of organic vapors (as specified in figure legends). Potential sweep rate 20 mV/s.

under study, the film conductivity exhibited a significantly more drastic decrease when exposed to styrene and toluene than to other vapors. For instance, in the presence of styrene (hexagons), the conductivity of the Ru=N nanoparticle film dropped sharply by about 90% at a vapor concentration of only 0.45 mM, and by 95% at higher vapor concentrations. For toluene (triangles), the diminishment of the particle conductivity was also apparent and yet less significant. When exposed to 0.47 mM of toluene vapors, the film lost about 50% of its conductivity, and at vapor concentrations higher than 1.5 mM, only 10% of the original conductivity was

retained. In contrast, markedly lower impacts were observed of the other four vapors on the nanoparticle ensemble conductivity. For instance, at 1 mM vapor concentration, the film conductivity decreased only by about 30%with 1-hexene (diamonds), about 18% with hexane (squares), and 17% with acetone (triangles) and ethanol (circles). Notably, the diminishment was also much slower with increasing vapor concentration than that observed with styrene and toluene. This can be clearly manifested in panel (B) which depicts the sensitivity of the nanoparticle film conductivity to the series of volatile solvents, with the sensitivity (S) defined as the tangent of the curves in the low vapor concentration regions in panel (A). One can see that, within the present experimental context, the sensitivity of detection of organic vapors by the Ru=N nanoparticle films decreased in the order of styrene (S = 2.02 mM^{-1}) > toluene (S = 0.81 mM^{-1}) > 1-hexene (S = 0.32 mM^{-1}) > n-hexane (S = 0.15 mM^{-1}) > ethanol(S = 0.14 mM^{-1}) > acetone (S = 0.13 mM^{-1}). These observations may be, in part, accounted for by the unique solubility properties of the Ru=N nanoparticles, which were found to be readily soluble in toluene and styrene, but insoluble in the less polar hexane and hexane or more polar ethanol and acetone—note that the relative polarity of these solvents is 0.654 (ethanol), 0.355(acetone), 0.127 (styrene), 0.099 (toluene), 1-hexene (0.052) and 0.009 (hexane) [27]. When exposed to these organic vapors, extensive penetration of the vapor molecules into the particle films was anticipated only with styrene and toluene, leading to effective swelling of the nanoparticle films and hence drastic diminishment of the interparticle charge transfer. For the other vapors, the wet-ting was most likely limited to the top

layers of the nanoparticle films and thus the impacts on the particle conductivity were small.

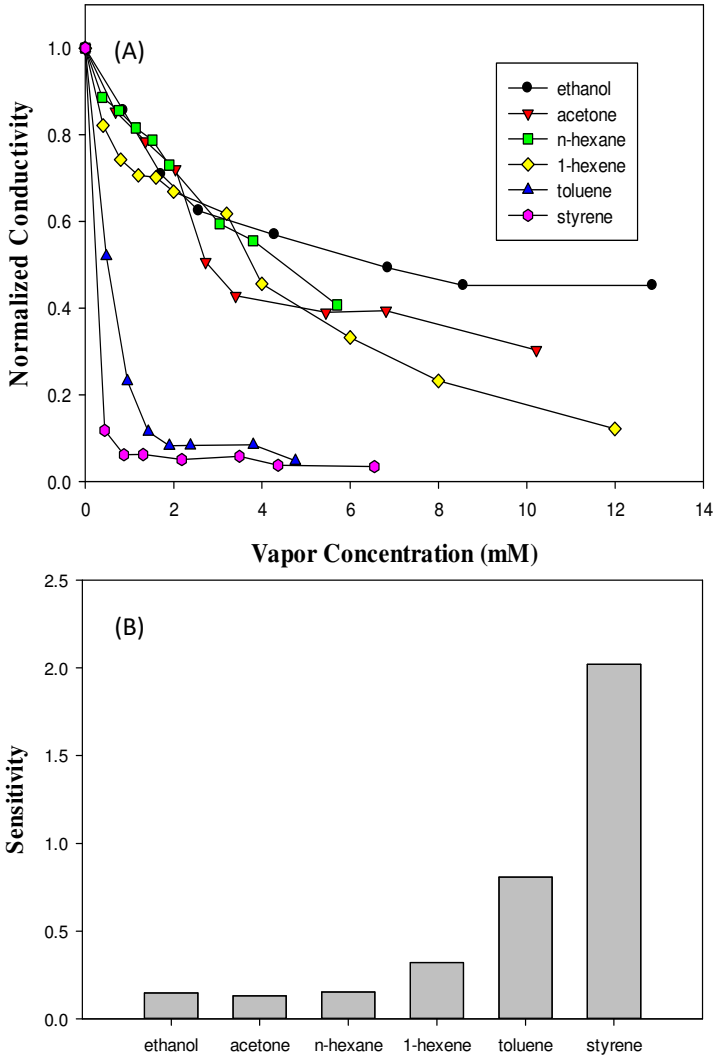

Figure 3.3 (A) Variation of the nanoparticle ensemble conductivity with the concentration of organic vapors. Symbols are experimental data calculated from Figure 3.2, and normalized to the values prior to exposure to the respective organic vapor. Lines are for eye-guiding only. (B) Sensitivity of nanoparticle film conductivity to volatile solvents.

However, when comparing the performance of styrene and toluene, one may notice that despite their very similar molecular structure, relative polarity and

nanoparticle solubility, the drop of conductivity of the nanoparticle solids was 2.5 times more sensitive to styrene than to toluene (Fig. 3.3 B). Such a marked difference of the impacts on the nanoparticle ensemble conductivity cannot be solely ascribed to a variation of nanoparticle solvation and swelling. Additional contributions most likely arose from the chemical reactivity of the Ru=N bonds to vinyl derivatives by imido transfer that resulted in the cyclic addition of the vinyl moiety to the Ru=N linkage (Scheme 3.1).[12] The diminishment of intraparticle charge delocalization then led to an increase of the energetic barrier for interparticle charge transfer. In fact, at the end of the conductivity tests, purging of ultrahigh-purity nitrogen did not restore the ensemble conductivity to the initial values, in sharp contrast to those exposed to other organic vapors that were found to be highly reversible.

Such a structural variation was manifested in photoluminescence measurements. Fig. 3.4 depicts the excitation and emission spectra (red curves) of the Ru=N nanoparticles after the conductivity tests in Fig. 3.2 (F) and re-dissolved in CH_2Cl_2. The spectra of the as-prepared nanoparticles (black curves) were also included for comparison. It can be seen that both samples exhibited a well-defined excitation and emission peak (at 367 and 469 nm, respectively) that was ascribed to the intraparticle charge delocalization between the particle-bound nitrene moieties, because of the conjugated Ru=N interfacial bonding interactions, which behaved analogously to azo (–N=N–) derivatives.[12]

However, an apparent decrease of the intensity can be seen after the particles were expo-sure to styrene, despite virtually unchanged optical absorbance as depicted in the UV–vis spectra (figure inset).

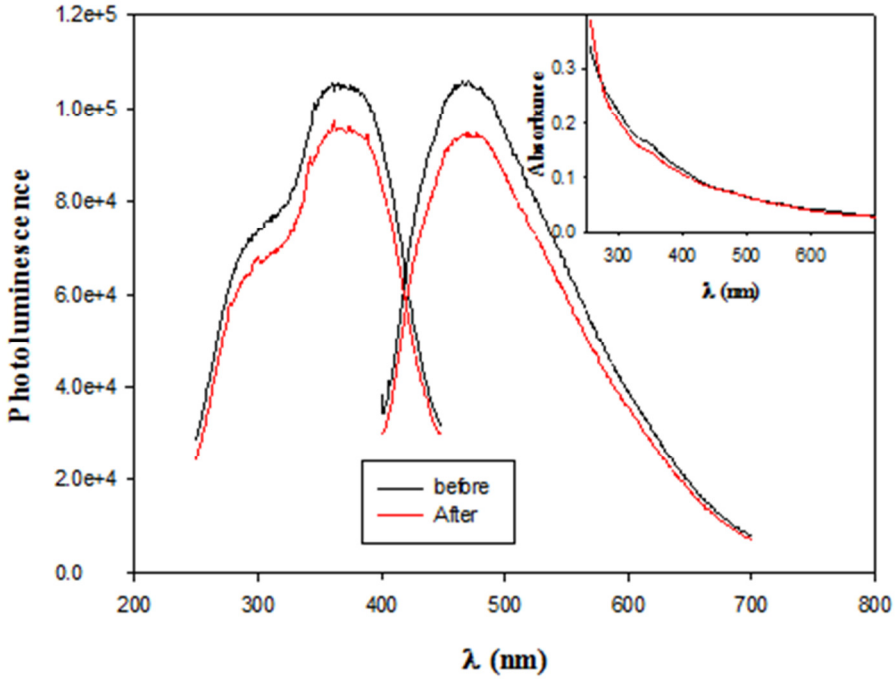

Figure 3.4. Photoluminescence spectra of Ru=N particles in CH_2Cl_2 before and after exposure to a styrene atmosphere of 6.5 mM. Inset shows the corresponding UV-vis absorption spectra. The sample was the same as that after the tests in Figure 3.2 (F).

In a previous study where the Ru=N nanoparticles were mixed with vinylferrocene in CH_2Cl_2, substantial diminishment of the nanoparticle photoluminescence was also observed, which was ascribed to the chemical reactivity of the Ru=N bonds with vinyl moieties that converted the conjugated interfacial linkages to saturated ones (Scheme 3.1).[12] It is interesting to note that in the present study, despite a low fraction of the Ru=N nanoparticles that reacted with styrene as suggested by the small change (ca. 10%) of nanoparticle photoluminescence, the

detection sensitivity of the nanoparticle films was enhanced by more than two folds, as compared to that with toluene.

Similar enhancement can be seen with 1-hexene as compared to n-hexane (Fig. 3.3). However, the lack of solvation of nanoparticles in these solvents most likely limited the reactions only to the top layers of the nanoparticle films, such that no significant difference was observed of the photoluminescence profiles. For other organic vapors, because of the lack of chemical reactivity, the nanoparticle optical characteristics remained unchanged. Such behaviors have been observed extensively in previous studies with nanoparticles functionalized with mercapto derivatives that are mostly chemically inert.[3,23,24]

3.3 Conclusion

In summary, the electronic conductivity of solid films of nitrene-functionalized ruthenium nanoparticles was found to decrease upon the exposure to a series of organic vapors of different relative polarity that included n-hexane, 1-hexene, toluene, styrene, ace-tone and ethanol. Interestingly, whereas the nanoparticle ensemble conductivity was found to diminish with increasing concentration of all organic vapors under study, the decrease was markedly more drastic with toluene and styrene than with other vapors. This was accounted for by the swelling of the particle films that led to enlarged separation between neighboring nanoparticles which impeded interparticle charge transfer. Furthermore, the particle conductivity was found to exhibit a much more sensitive variation by styrene than by toluene, which was ascribed to the additional contributions arising from the unique

chemical reactivity of the Ru=N interfacial bonds towards vinyl moieties by imido transfer. The transformation of conjugated Ru=N interfacial linkages to saturated ones diminished the spilling of metal core electrons into the organic protecting ligands and thus increased the metal–ligand interfacial contact resistance. These results suggest that metal–ligand interfacial bonding interactions may be exploited as a unique variable for further enhancement of the selective sensing of organic vapors by functional nanoparticles.

3.4 References

(1)Chen, W.; Zuckerman, N. B.; Kang, X. W.; Ghosh, D.; Konopelski, J. P.; Chen, S. W.: Alkyne-Protected Ruthenium Nanoparticles. *J Phys Chem C* **2010**, *114*, 18146-18152.

(2) Liu, K.; Kang, X.; Zhou, Z.-Y.; Song, Y.; Lee, L. J.; Tian, D.; Chen, S.: Platinum nanoparticles functionalized with acetylene derivatives: Electronic conductivity and electrocatalytic activity in oxygen reduction. *J Electroanal Chem* **2013**, *688*, 143-150.

(3) Kang, X. W.; Chen, S. W.: Electronic conductivity of alkyne-capped ruthenium nanoparticles. *Nanoscale* **2012**, *4*, 4183-4189.

(4) Chen, W.; Zuckerman, N. B.; Lewis, J. W.; Konopelski, J. P.; Chen, S. W.: Pyrene-Functionalized Ruthenium Nanoparticles: Novel Fluorescence Characteristics from Intraparticle Extended Conjugation. *J Phys Chem C* **2009**, *113*, 16988-16995.

(5) Kang, X. W.; Chen, W.; Zuckerman, N. B.; Konopelski, J. P.; Chen, S. W.: Intraparticle Charge Delocalization of Carbene-Functionalized Ruthenium Nanoparticles Manipulated by Selective Ion Binding. *Langmuir* **2011**, *27*, 12636-12641.

(6) Porter, M. D.; Bright, T. B.; Allara, D. L.; Chidsey, C. E. D.: Spontaneously organized molecular assemblies. 4. Structural characterization of n-alkyl thiol monolayers on gold by optical ellipsometry, infrared spectroscopy, and electrochemistry. *J Am Chem Soc* **1987**, *109*, 3559-3568.

(7) Goujon, F.; Bonal, C.; Limoges, B.; Malfreyt, P.: Description of Ferrocenylalkylthiol SAMs on Gold by Molecular Dynamics Simulations. *Langmuir* **2009**, *25*, 9164-9172.

(8) Rowe, G. K.; Creager, S. E.: Chain-Length and Solvent Effects on Competitive Self-Assembly of Ferrocenylhexanethiol and 1-Alkanethiols onto Gold. *Langmuir* **1994**, *10*, 1186-1192.

(9) He, G.; Song, Y.; Kang, X.; Chen, S.: Alkyne-functionalized palladium nanoparticles: Synthesis, characterization, and electrocatalytic activity in ethylene glycol oxidation. *Electrochim Acta* **2013**, *94*, 98-103.

(10) Templeton, A. C.; Chen, S. W.; Gross, S. M.; Murray, R. W.: Water-soluble, isolable gold clusters protected by tiopronin and coenzyme A monolayers. *Langmuir* **1999**, *15*, 66-76.

(11) Creager, S. E.; Rowe, G. K.: Redox Properties of Ferrocenylalkane Thiols Coadsorbed with Linear Normal-Alkanethiols on Polycrystalline Bulk Gold Electrodes. *Anal Chim Acta* **1991**, *246*, 233-239.

(12) Kang, X. W.; Song, Y.; Chen, S. W.: Nitrene-functionalized ruthenium nanoparticles. *J Mater Chem* **2012**, *22*, 19250-19257.

(13) Zhou, Z. Y.; Kang, X. W.; Song, Y.; Chen, S. W.: Ligand-Mediated Electrocatalytic Activity of Pt Nanoparticles for Oxygen Reduction Reactions. *J Phys Chem C* **2012**, *116*, 10592-10598.

(14) Pietron, J. J.; Garsany, Y.; Baturina, O.; Swider-Lyons, K. E.; Stroud, R. M.; Ramaker, D. E.; Schull, T. L.: Electrochemical Observation of Ligand Effects on Oxygen Reduction at Ligand-Stabilized Pt Nanoparticle Electrocatalysts. *Electrochemical and Solid-State Letters* **2008**, *11*, B161.

(15) Uosaki, K.; Sato, Y.; Kita, H.: Electrochemical Characteristics of a Gold Electrode Modified with a Self-Assembled Monolayer of Ferrocenylalkanethiols. *Langmuir* **1991**, *7*, 1510-1514.

(16) Kang, X. W.; Zuckerman, N. B.; Konopelski, J. P.; Chen, S. W.: Alkyne-Stabilized Ruthenium Nanoparticles: Manipulation of Intraparticle Charge Delocalization by Nanoparticle Charge States. *Angew Chem Int Edit* **2010**, *49*, 9496-9499.

(17) Kang, X. W.; Zuckerman, N. B.; Konopelski, J. P.; Chen, S. W.: Alkyne-Functionalized Ruthenium Nanoparticles: Ruthenium-Vinylidene Bonds at the Metal-Ligand Interface. *J Am Chem Soc* **2012**, *134*, 1412-1415.

(18) Chen, W.; Chen, S. W.; Ding, F. Z.; Wang, H. B.; Brown, L. E.; Konopelski, J. P.: Nanoparticle-mediated intervalence transfer. *J Am Chem Soc* **2008**, *130*, 12156-12162.

(19) Liu, K.; Song, Y.; Chen, S.: Electrocatalytic activities of alkyne-functionalized copper nanoparticles in oxygen reduction in alkaline media. *J Power Sources* **2014**, *268*, 469-475.

(20) Zamborini, F. P.; Leopold, M. C.; Hicks, J. F.; Kulesza, P. J.; Malik, M. A.; Murray, R. W.: Electron hopping conductivity and vapor sensing properties of flexible network polymer films of metal nanoparticles. *J Am Chem Soc* **2002**, *124*, 8958-8964.

(21) Ahn, H.; Chandekar, A.; Kang, B.; Sung, C.; Whitten, J. E.: Electrical conductivity and vapor-sensing properties of omega-(3-thienyl)alkanethiol-protected gold nanoparticle films. *Chem Mater* **2004**, *16*, 3274-3278.

(22) Garcia-Berrios, E.; Gao, T.; Woodka, M. D.; Maldonado, S.; Brunschwig, B. S.; Ellsworth, M. W.; Lewis, N. S.: Response versus Chain Length of Alkanethiol-Capped Au Nanoparticle Chemiresistive Chemical Vapor Sensors. *J Phys Chem C* **2010**, *114*, 21914-21920.

(23) Wang, G. N. R.; Wang, L. Y.; Qiang, R. D.; Wang, J. G.; Luo, J.; Zhong, C. J.: Correlation between nanostructural parameters and conductivity properties for molecularly-mediated thin film assemblies of gold nanoparticles. *J Mater Chem* **2007**, *17*, 457-462.

(24) Terrill, R. H.; Postlethwaite, T. A.; Chen, C. H.; Poon, C. D.; Terzis, A.; Chen, A. D.; Hutchison, J. E.; Clark, M. R.; Wignall, G.; Londono, J. D.; Superfine, R.; Falvo, M.; Johnson, C. S.; Samulski, E. T.; Murray, R. W.: Monolayers in three dimensions: NMR, SAXS, thermal, and electron hopping studies of alkanethiol stabilized gold clusters. *J Am Chem Soc* **1995**, *117*, 12537-12548.

(25) Garcia-Berrios, E.; Gao, T.; Theriot, J. C.; Woodka, M. D.; Brunschwig, B. S.; Lewis, N. S.: Response and Discrimination Performance of Arrays of Organothiol-Capped Au Nanoparticle Chemiresistive Vapor Sensors. *J Phys Chem C* **2011**, *115*, 6208-6217.

(26) Stephens, I. E.; Bondarenko, A. S.; Perez-Alonso, F. J.; Calle-Vallejo, F.; Bech, L.; Johansson, T. P.; Jepsen, A. K.; Frydendal, R.; Knudsen, B. P.; Rossmeisl, J.; Chorkendorff, I.: Tuning the activity of Pt(111) for oxygen electroreduction by subsurface alloying. *J Am Chem Soc* **2011**, *133*, 5485-91.

(27) Reichardt, C.; Welton, T.: *Solvents and solvent effects in organic chemistry*; 4th, updated and enl. ed.; Wiley-VCH: Weinheim, Germany, 2011.

(28) Ghosh, D.; Pradhan, S.; Chen, W.; Chen, S. W.: Titanium Nanoparticles Stabilized by Ti-C Covalent Bonds. **2008**.

(29) Ghosh, D.; Chen, S.: Palladium nanoparticles passivated by metal–carbon covalent linkages. *J Mater Chem* **2008**, *18*, 755.

(30) Lide, D. R.: *CRC handbook of chemistry and physics : a ready-reference book of chemical and physical data*; 85th ed.; CRC Press: Boca Raton, Fla., 2004.

Chapter 4

Alkyne-Protected AuPd Alloy Nanoparticles for Electrocatalytic Reduction of Oxygen

4.1 Introduction

Alloying a metal nanoparticle with another or even multiple other metals has been extensively studied as a means to control particle properties and consequently a sophisticated theory explaining and predicting their behavior has developed. Beyond providing potential dilution of surface sites, the second metal serves to alter the electronic structure of surface atoms by imparting a lateral force on the particle lattice [1] as well driving electron rearrangements between neighboring atoms with different d band filling and electronegativity [2,3]. Respectively termed strain and ligand effects, both situations will ultimately alter the d band structure of the surface metal and thus the degree of filling for the metal-adsorbate antibonding state and strength of adsorptive interaction. [4-7]

In fact, the d-band theory of adsorbate interaction strength has been well established and is in agreement with countless experiments and theoretical simulations.[3,8] Although there are many parameters contributing to the d band characteristics, it has been determined that the d band center relative the fermi level is sufficient to describe adsorptive behaviors of a metal surface.[9] High centers relative the fermi level result in antibonding orbitals above the fermi level that remain unfilled and lead to strong interactions between the surface and adsorbate. Low d band centers create antibonding orbitals lower than the fermi level that are filled and result in weak bond between surface and adsorbate.[10] As the efficiency of catalysis is largely dependent on the binding interaction between the metal surface and the reactants, intermediates, and final product(s), alloying can be a powerful method to

fine tune adsorptive properties.[11,12] One important reaction that is severely limited by unfavorable binding interactions between catalyst surface and reaction intermediates is the electrocatalytic reduction of oxygen necessary for harnessing energy from hydrogen fuel cells (PEMFC).[13,14]

Proton exchange membrane fuel cells (PEMFCs) have been gaining much attention recently as long-range energy sources for commercial vehicles, but are not currently available in commercial settings, because a large amount of precious metal catalyst is required for sufficient power output.[15] This large electrocatalytic demand is largely a result of the sluggish electron-transfer kinetics of oxygen reduction reactions (ORRs) at the cathode.[16-18] Although platinum has been identified as the best single metal electrocatalyst for oxygen reduction, the low abundance and high cost have limited the scale of such fuel cells and, thus, the availability of this energy source for commercial settings, even with the large surface area to volume ratio of nanoparticles.

It is clear that a modified approach must be pursued. In fact, a number of strategies have been developed and described in the literature.[2,19-27] One effective procedure is to alloy platinum with another metal in the form of homogenous or core–shell structures, which has allowed a drastic decrease in the amount of platinum with equal or better activity than that of pure Pt.[2,20-22,28] This enhancement in activity is attributed to alterations of d band center relative the fermi level resulting from the electronic interactions between neighboring atoms as well as strains from lattice mismatch.[2,22] These apparent ligand and strain effects and will alter the catalytic

activity based on changes in the adsorption kinetics of oxygen on the nanoparticle surface.[29-32]

For instance, previous studies have shown that the activity of Pt(111) surfaces modified with a subsurface copper layer exhibits a volcano-shaped trend when plotted versus the content of copper.[3] Generally, platinum and platinum-group metals bind too strongly to oxygenated intermediates. The trend in activity is, therefore, a result of weakening interactions of oxygenated intermediates with the platinum surface as copper content increases, with the peak representing the optimal concentration: low copper contents lead to strong interactions with oxygen, resulting in unfavorable removal of the final products and a small number of active sites, whereas high copper contents result in unfavorable initial adsorption and, thus, a low number of surface oxygen groups to reduce. This volcano trend was predicted by Sabatier years ago, with the peak activity in agreement with theoretical calculations based on adsorption energies.[33]

The enhancement in electrocatalytic activity of alloys, as compared to pure metal constituents, has also been recognized for many non-platinum metals including gold and palladium.[31,32,34-42] For instance, palladium is a platinum-group metal that binds to oxygen even more strongly than platinum, whereas gold has very little interaction with oxygen, making these two metals optimal candidates for a binary alloy.[33] The electrocatalytic properties of AuPd alloy nanoparticles have been found to be largely dependent on the size, elemental composition, and distribution; thus, much effort has been focused on controlling such features.[43] For instance,

stabilization and reduction in sol-gel has afforded monodispersed AuPd particles with diameters between 2.0 and 7.5 nm, which have exhibited onset potentials at least 200 mV more positive for oxygen reduction than a bare glassy-carbon electrode.[44] Ionic liquid microemulsion techniques have enabled precise control over the elemental composition[45] in addition to allowing for temporal separation between reduction of metals and, consequently, control over elemental distribution.[46] Co-reduction of metal salts in alcohols has yielded alloy particles with a gold enriched core and palladium-enriched shell with an average particle diameter of 2.14 nm.[47] Intermittent microwave heating combined with sodium borohydride reduction produced gold palladium alloy nanoparticles supported on tungsten carbide, which exhibited an onset potential for oxygen reduction 70 mV more positive than that of commercial platinum electrocatalysts.[34] From these studies, it is clear that gold and palladium alloys offer promising results; yet, the optimal ratio of gold and palladium in nanoparticles for electrocatalytic oxygen reduction has remained largely unexplored, to the best of our knowledge. This is the primary motivation and focus of the present work.

In the present study, a series of AuPd alloy nanoparticles were prepared through $NaBH_4$ reduction of metal-salt precursors with a deliberate variation of the initial feed ratio in the presence of 1-dodecyne by taking advantage of the strong affinity of alkyne ligands to transition-metal surfaces. With the alkyne capping ligands, the nanoparticles were stabilized under ambient conditions, readily dispersible in common organic solvents, and the size was controlled to within a

narrow range. The structures of the resulting nanoparticles were then characterized by using a variety of microscopic and spectroscopic measurements. Electrochemical studies showed that the resulting nanoparticles all exhibited apparent electrocatalytic activity in the ORR, and the best performance was observed with the sample consisting of 91.2% Pd and 8.8% Au, where the mass activity was over eight times better than that of commercial palladium black and the specific activity almost twice as good.

4.2 Results and Discussion

The chemical compositions of the AuPd alloy nanoparticles were first analyzed by performing XPS measurements. Figure 4.1 depicts the high-resolution scans of the Pd3d and Au4f electrons of the series of AuPd nanoparticles. It can be seen that for all samples, the Pd3d spectra may be deconvoluted into two doublets. The pairs at lower energies (335.6 and 340.9 eV) are consistent with those of metallic Pd, whereas those at somewhat higher energies (336.9 and 342.2 eV) may be assigned to Pd(II) species.[48] This suggests the formation of a substantial amount of palladium oxide in the nanoparticles, which may, in part, be ascribed to electron transfer from palladium to gold as a result of the stronger electronegativity of gold than that of palladium. In contrast, for the Au4f electrons, only a single pair of peaks may be resolved at approximately 83 and 87 eV, which are in good agreement with the binding energies of the 4f7/2 and 4f5/2 electrons of metallic Au, respectively.[48]

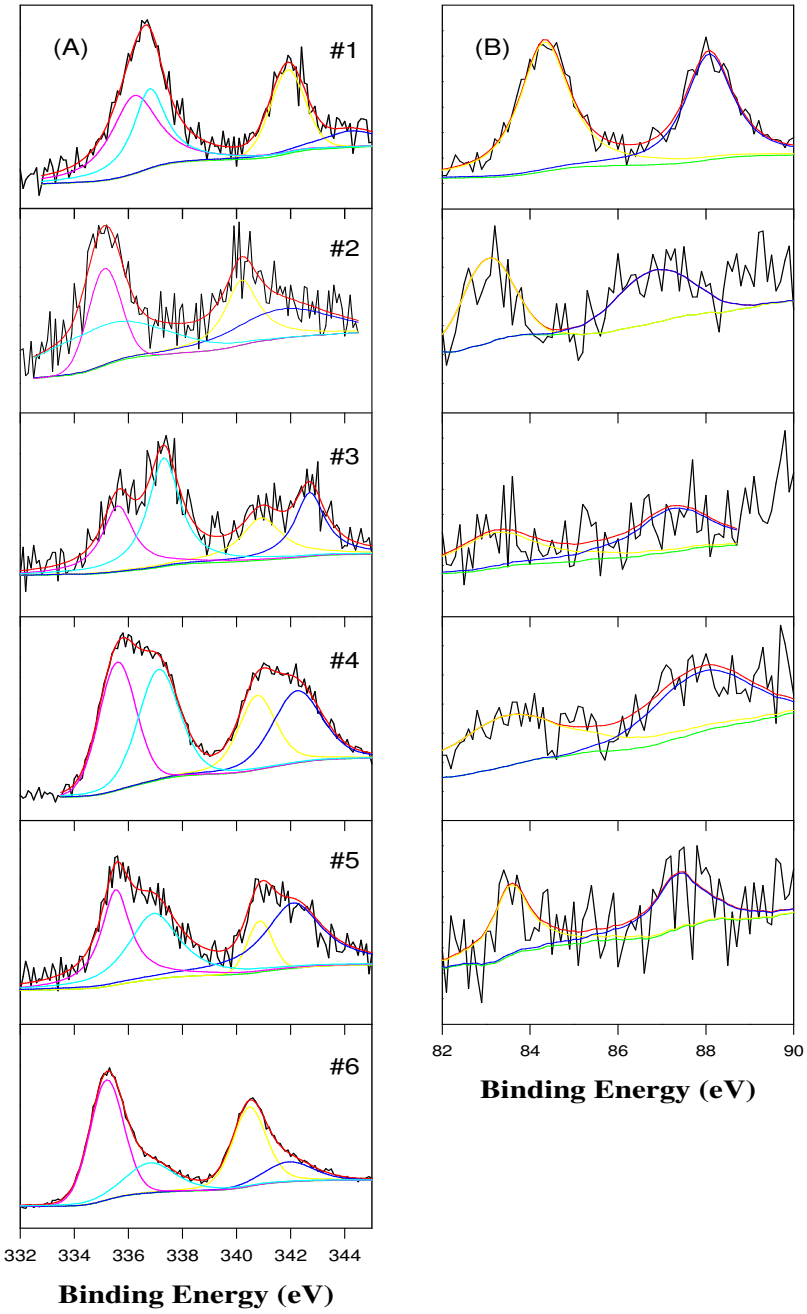

Figure 4.1. High-resolution XPS spectra of A) Pd3d and B) Au4f electrons of AuPd alloy nanoparticles at varied Pd concentrations of 64.9, 87.0, 91.2, 92.8, 94.1, and 100% for samples 1 to 6, respectively. Black curves are experimental data and colored curves are deconvolution fits.

Furthermore, based on the integrated peak areas, the atomic concentrations of palladium in the nanoparticle cores were estimated to be 64.9, 87.0, 91.2, 92.8, 94.1, and 100% for samples 1 to 6, respectively (Table 4.1).

	#1	#2	#3	#4	#5	#6	Commercial Pd black
Core diameter (nm)	4.48 ± 0.51	3.12 ± 0.39	4.89 ± 0.60	2.68 ± 0.70	3.28 ± 0.83	4.11 ± 1.28	~ 6.0 (ref. [49])
Pd at.%	64.9	87.0	91.2	92.8	94.1	100	100
Onset potential (V vs RHE)	+0.93	+0.97	+0.98	+0.98	+0.96	+0.96	+0.96
J_s (□A/cm^2 at +0.90 V)	158	110	610	245	204	253	356
J_m (A/g at +0.90 V)	39	64	162	95	41	30	19

Table 4.1. Spectroscopic and electrochemical characteristics of all AuPd samples

Further structural insights were obtained by performing TEM measurements. Figure 4.2 shows a representative TEM image of the nanoparticles. One can see that the majority of the AuPd alloy nanoparticles were rather well dispersed without apparent aggregation, suggesting effective passivation of the metal cores by the alkyne ligands. In addition, statistical analysis based on more than 100 nanoparticles shows that the average nanoparticle diameter actually fluctuated within the narrow range of 3–5 nm with palladium contents at 4.84±0.51, 3.12±0.39, 4.89±0.60, 2.68±0.70, 3.28±0.83, and 4.11±1.28 nm for samples 1 to 6, respectively. These data are also listed in Table 4.1.

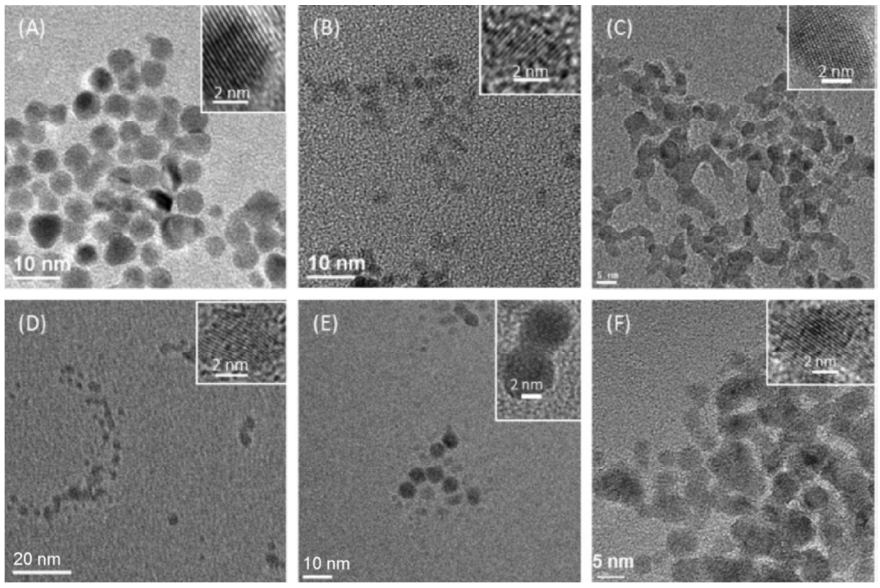

Figure 4.2. Representative TEM images of AuPdHC12 nanoparticles at different palladium concentrations: A) 64.9, B) 87.0, C) 91.2, D) 92.8, E) 94.1, and E) 100%. Insets show the corresponding high-resolution TEM images

The slight variation in size is likely a result of the nanoparticle growth dynamics, where metal nucleation competes with ligand adsorption (nucleation vs. passivation).[50] That is, the bonding of alkyne ligands on Au is not as strong as on Pd and the reduction potential of Au(III) (+1.5 V) is significantly more positive than that of Pd(II) (+0.987), leading to different sizes for samples with different feeding ratios. Furthermore, well-defined lattice fringes can readily be identified for the AuPd nanoparticles from the high-resolution TEM images depicted in the corresponding figure insets. For samples with small percentages of gold (samples 3–6), the lattice spacing was in strong agreement with that of Pd(111) (2.24 Å). For the samples with a larger content of gold (samples 1 and 2), the lattice spacing was around 2.28 Å,

which is in the intermediate range between those of Pd(111) and Au(111) (2.35 Å) crystalline planes, a common feature in bimetallic alloys.[37,44] This not only suggests alloying between the metals, but is also direct visual evidence of lattice strain in the nanoparticles.

UV/Vis absorption spectroscopy also confirmed the formation of nanosized particles, which was manifested by the exponential decay profiles, the so-called Mie scattering. From Figure 4.3 A, it can be seen that, for the sample exhibiting the highest concentration of gold (sample 1, 64.9% Pd and 35.1% Au) a broad peak centered around 520 nm also appeared, which was ascribed to the surface plasmon resonance of gold nanoparticles. The absence of this peak for samples with lower gold contents has previously been observed [44,46] and ascribed to the rearrangement of electron density between the two metals.[51]

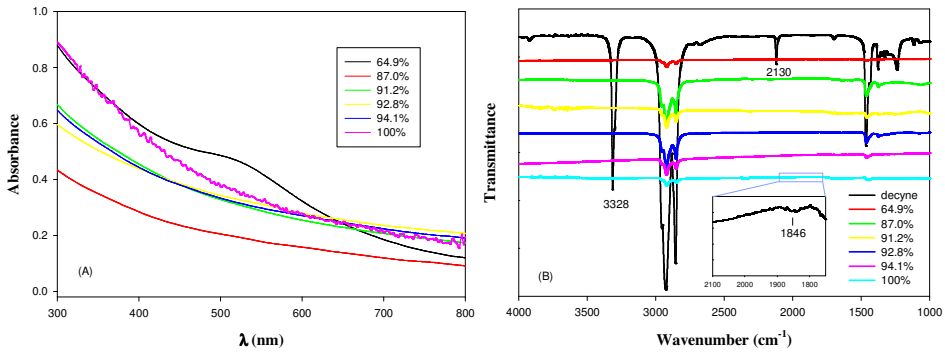

Figure 4.3. A) UV/Vis absorption spectra and B) FTIR spectra of 1-dododecynefunctionalized AuPd nanoparticles at various Pd concentrations. The FTIR spectrum of monomeric 1-dododecyne is also included as the black curve in panel (B). Inset shows the magnified region between 2100 and 1700 cm^{-1}.

FTIR measurements confirmed the bonding attachment of the dodecyne ligands on the metal nanoparticle surface. From Figure 4.3 B, one can see that, for monomeric ligands (black curve), several well-defined vibrational features can be readily identified, such as the terminal H-C≡ stretch at 3300 cm^{-1}, C≡C stretch at 2100 cm^{-1}, methyl and methylene stretches around 2900 cm^{-1}, and the scissoring and rocking of the carbon chains at 1470 and 1375 cm^{-1}, respectively. For the nanoparticle samples, however, the terminal H-C≡ stretch vanished altogether and the C≡C stretch red-shifted to 1846 cm^{-1} (Figure inset), whereas the rest of the vibrational features remained almost unchanged. This suggests the ready cleavage of the terminal H-C≡ bonds when the ligands self-assembled on the nanoparticle surface, forming metal–acetylide (M-C≡) /–vinylidene (M=C=CH-) interfacial bonds through a tautomeric rearrangement process and, hence, leading to a redshift of the C≡C stretch through intraparticle charge delocalization. Similar behaviors have been observed in a series of recent studies.[52-54] The absence of the H-C≡ vibrational stretch also signified that the nanoparticle samples were free of excessive monomeric ligands.

The electrocatalytic activity of the AuPd nanoparticles for the ORR was then examined and compared through voltammetric measurements in N_2- and O_2-saturated 0.1 M NaOH solutions. Note that, before the ORR measurements, the electrodes were subject to an electrochemical activation treatment by rapid potential cycling (500 mVs^{-1}) between 0 and +1.2 V (vs. RHE) in a N_2- saturated 0.1 M NaOH solution until a steady voltammogram was obtained. From Figure 4.4, it can be seen that, for

pure gold nanoparticles (aqua blue curve) in N_2-saturated NaOH, the anodic scan of gold oxidation started to occur at about +1.15 V, whereas, in the cathodic scan, the reduction of gold oxide peaked at +0.991 V. In contrast, for pure palladium nanoparticles (magenta curve), the peak potential of the reduction of palladium oxide was far more negative at +0.567 V, indicating that palladium interacts far more strongly with oxygenated species than gold.[55]

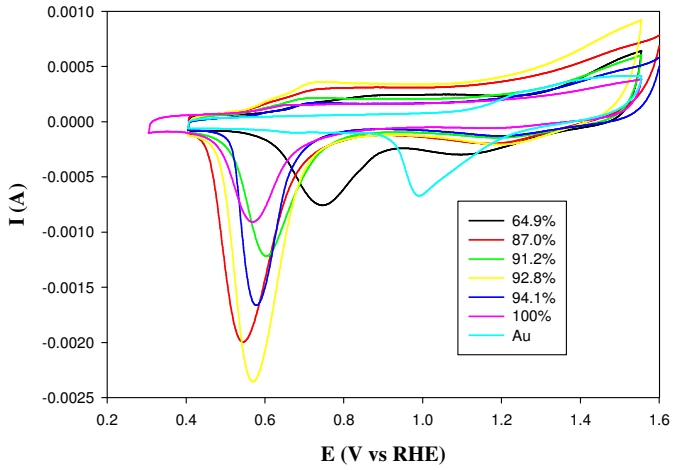

Figure 4.4. Cyclic voltammograms of a glassy carbon electrode modified with different AuPd nanoparticles in nitrogen-saturated 0.1 M NaOH. The data for pure Au nanoparticles were also included as the aqua- blue curve. Potential sweep rate: 100 mV s^{-1}.

Interestingly, for the series of AuPd alloy nanoparticles, only a single cathodic peak was observed, likely because of intimate alloying of the metals in the nanoparticles rather than formation of separate nanoparticles, as manifested in TEM measurements (Figure 4.2). In addition, the peak potential for metal-oxide reduction exhibited a clear variation with the elemental particle composition. For instance, for

sample1 (64.9% Pd), the oxide reduction peaked at +0.746 V, which is between those of pure Au and pure Pd, suggesting that both Pd and Au components were readily accessible on the nanoparticle surface; however, for other AuPd nanoparticles, the peak potentials were actually very close to that of pure Pd, at +0.546, +0.578, +0.568, and +0.604 V for samples 2 to 5, respectively. This implies that in these Pd-dominant nanoparticles (Pd concentrations >87 %), the surface was primarily enriched with Pd.

In addition, based on the integrated peak area, the effective electrochemical surface area (ECSA) was estimated to be 18.0, 25.3, 15.3, 28.0, 14.7, and 10.7 $m^2 g^{-1}$ for samples 1 to 6, respectively. In comparison to the theoretical surface area (by assuming a spherical shape, Figure 4.2), the fraction of nanoparticle surface that was electrochemically accessible decreased roughly with increasing Pd concentration (20.8, 24.4, 12.8, 18.0, 7.9, and 7.4% for samples 1 to 6, respectively). This might be associated with the relatively strong bonding interactions of Pd with the alkyne ligands as compared to gold, such that an increase of Pd concentration in the nanoparticles would render it increasingly difficult to desorb the organic capping ligands during the electrochemical activation process.

The electrocatalytic activity for oxygen reduction was then evaluated by using rotating ring-disk electrode (RRDE) voltammetric measurements in O_2-saturated 0.1 M NaOH at different rotation rates. Figure 4.5 A depicts the RDE voltammograms of the series of AuPd nanoparticles at a rotation rate of 1600 RPM, along with that of commercial Pd black. It can be seen that nonzero currents started to appear at around +1.0 V and, at even more negative electrode potentials, the currents increased

drastically and reached a plateau at potentials < +0.80 V. This signified apparent electrocatalytic activity of the nanoparticles in oxygen reduction.

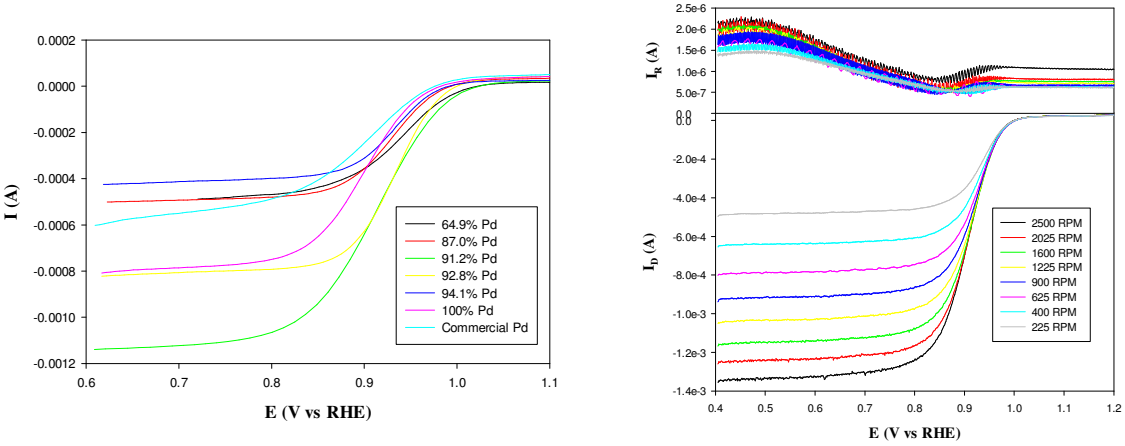

Figure 4.5. A) RRDE voltammograms of a glassy carbon electrode modified with various AuPd alloy nanoparticles in oxygen-saturated 0.1 M NaOH at 1600 RPM. B) RRDE voltammograms of a glassy carbon electrode modified with sample 3 AuPd alloy nanoparticles in oxygen-saturated 0.1 M NaOH. Disk potential sweep rate: 10 mVs^{-1}; ring potential: +1.5 V; catalyst loading: 0.60 g m^{-2}.

From the voltammograms, the onset potential of the ORR can be identified at +0.93, +0.97, +0.98, +0.98, +0.96, and +0.96 V for samples 1 to 6, respectively, and +0.96 V for Pd black. Of note is that the onset potentials of samples 3 and 4 were the most positive among the series, even slightly more positive (by up to 30 mV) than those of pure Pd nanoparticles (sample 6) and Pd black. In addition, the limiting currents also showed an apparent variation with the nanoparticle compositions. For instance, the limiting currents at +0.75V were 0.48, 0.49, 1.10, 0.80, 0.41, and 0.78 mA for samples 1 to 6, respectively, and 0.53 mA for commercial Pd black (note that the metal loadings were the same for all nanoparticle catalysts). From these results,

one can see that among the series, sample 3 (91.2% Pd) stood out as the best ORR catalyst with the most positive onset potential and highest limiting currents.

More detailed studies were carried out by using RRDE measurements. Figure 4.5 B depicts the RRDE voltammograms of AuPd nanoparticles (sample 3) at various electrode rotation rates (225–2500 RPM) with the ring potential set at +1.50 V. It can be seen that the disk limiting current increased with increasing electrode rotation rates, and the ring current was about two orders of magnitude lower than those at the disk electrode, signifying the production of only a minimal amount of peroxide species, such that the ORR most likely proceeded through the four-electron reduction pathway to OH^-. Similar behaviors are observed with other AuPd nanoparticles and based on the disk (I_D) and ring (I_R) currents, the electron-transfer number (n) can be quantitatively estimated by the equation, $n = 4\, I_D \Big/ (I_D + {}^{I_R}\!/_{N})$, where N is collection efficiency of the electrode (40 %).[25] Figure 4.6 depicts the variation of the n values with electrode potentials for the series of nanoparticle samples. It can be seen that, at potentials more negative than +0.90 V, all samples exhibited $n \approx 4.0$, except for sample 1 where $n \approx 3.92$, indeed suggesting almost full reduction of oxygen to OH^-.

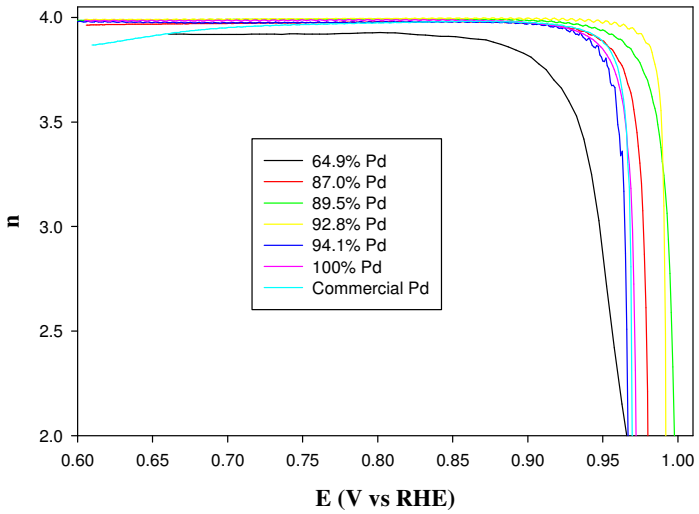

Figure 4.6. Variation in the electron transfer number of AuPd nanoparticles during oxygen reduction.

The electron-transfer kinetics were further analyzed by using the Koutecky–Levich (K–L) method. As the voltammetric disk current (I_D) may include both kinetic (I_k) and diffusion-controlled (I_d) contributions, the K–L equation is expressed as shown in Equations (4.1)–(4.3):

$$\frac{1}{I_D} = \frac{1}{I_k} + \frac{1}{I_d} = \frac{1}{I_k} + \frac{1}{B\omega^{1/2}} \quad (4.1)$$

$$B = 0.62nFAC_O D_O^{2/3} \nu^{-1/6} \quad (4.2)$$

$$I_k = nAFkC_O \quad (4.3)$$

where w is the electrode rotation rate, n is electron-transfer number, F is the Faraday constant (96485 C mol^{-1}), A is the geometric surface area of the electrode, C_O is the oxygen concentration in O_2-saturated solutions (1.26×10^{-6} mol/cm^3),[56] D_O is the diffusion coefficient of O_2 in 0.1 M NaOH aqueous solution (1.93×10^{-5} cm^2/s),[57] v is the kinematic viscosity of the solution (1.009×10^{-2} cm^2/s), [58] and k is the electron-

transfer rate constant. The K–L plots of I_D^{-1} versus $\omega^{-½}$ exhibited good linearity with consistent slopes in each sample, suggesting a first-order reaction with respect to oxygen concentration in the solution.

In addition, the y-axis intercepts of the linear regressions may be exploited for the quantification of the kinetic current density (J_k, I_k normalized to the ECSA of the nanoparticle catalysts). Figure 4.7 A depicts the corresponding Tafel plot, where one can see that, for all samples, the kinetic current density increased markedly with increasingly negative electrode potential, and sample 3 (91.2% Pd) stood out as the best catalyst among the series with the highest current density, even better than the commercial Pd black. For instance, at +0.90 V, the specific activity (J_k) was 158, 110, 610, 245, 204, and 253 mA cm^{-2} for samples 1 to 6, respectively, and 356 mA cm^{-2} for commercial Pd, as depicted by the red bars in panel B of Figure 4.7, where the activity of sample 3 was almost twice that of commercial Pd black.

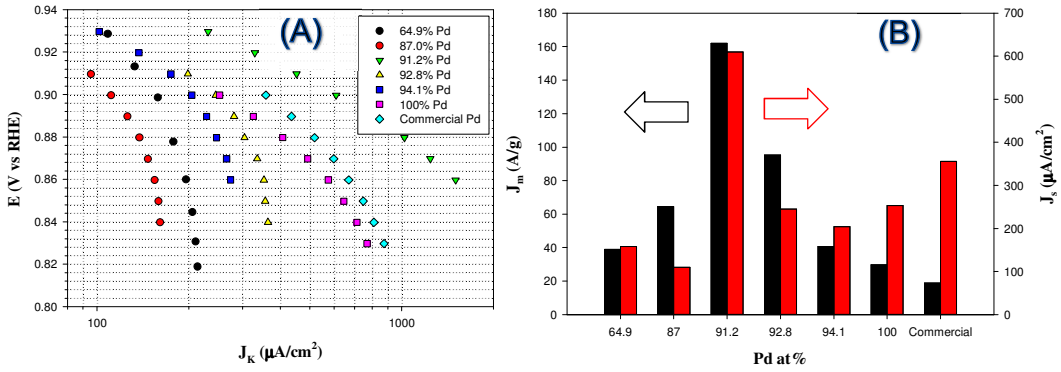

Figure 4.7. A) Tafel plot of dodecyne-capped AuPd nanoparticles in oxygen reduction. B) Comparison of the specific activity (J_s, red bars) and mass activity (J_m, black bars) at +0.90 V for the series of AuPd nanoparticles in ORR.

Similar behaviors can be observed with the mass activity (J_m, I_k normalized by the mass of the respective nanoparticles; black bars in panel B), which also exhibited a volcano-shaped variation with Pd concentration in the nanoparticles (data also listed in Table 1). Again, sample 3 can be identified as the best catalyst among the series with a mass activity of about 162 A g^{-1}, which was more than eight times that of a much larger commercial Pd black catalyst (ca. 6 nm in diameter)[49] and nearly five times that of dodecyne capped pure palladium particles (sample 6).

It should be noted that, for the ORR, the Tafel slopes are typically found at 60 or 120 mVdec^{-1}, where the former corresponds to a pseudo-two-electron reaction as the rate-determining step, and the latter suggests that the rate-determining step is a first-electron reduction of oxygen, implying that the subsequent reduction and O-O bond-breaking steps are relatively facile.[16] In the present study, linear regressions yielded Tafel slopes in the low overpotential regime (E > +0.88 V) of 181, 166, 69, 130, 85, 96 mV dec^{-1} for samples 1 to 6, respectively, and 125 mV dec^{-1} for commercial Pd. This seems to suggest that the ORR on sample 3 was largely limited by the pseudo-two-electron reduction step, whereas for samples 4 to 6 (high Pd loadings), the first-electron reduction was likely the rate-limiting step, similar to that of commercial Pd black. However, for samples 1 and 2 (low Pd loadings), the exceedingly high Tafel slopes suggest that oxygen adsorption was likely the limiting factor in the ORR kinetics, probably caused by the relatively high concentrations of gold that diminished the binding affinity to oxygen.

Note that the ORR performance of sample 3 is markedly better than leading results in the literature with relevant Pd based alloy nanoparticles. For example, Sekol et al. deposited silver–palladium core–shell alloy nanoparticles (diameter: 7.5 nm) onto multiwall carbon nanotubes and observed an onset potential of oxygen reduction around +0.9 V versus RHE and an n value of about 3.[59] In another study, Hu et al. decorated ordered mesoporous carbons with palladium–tungsten alloy nanoparticles that featured segregated nanoislands of palladium (ca. 1 nm) on the nanoparticle surface, and found that the onset potential of ORR was about +0.86V versus RHE, a positive shift of 60 mV compared to that of ordered mesoporous carbons with tungsten nanoparticles alone. [60] Alloy nanoparticles have also been prepared by incorporating Fe, Cu, and Ni into Pd at controlled concentrations through co-impregnation and single-phase colloidal methods, yielding stable particles on a Vulcan carbon support, and the best activities were found to be around 30 A g^{-1} for PdFe, 95 A g^{-1} for PdCu, and 20 A g^{-1} for PdNi at +0.90 V versus RHE.[61] Cobalt–palladium core–shell nanoparticles and alloy nanoparticles[62] have also been prepared and the onset potentials (+0.83 and +0.87 V) and specific activity (500 and 75 mA cm^{-2} at +0.75 V) remained subpar compared to those of the similarly sized AuPd alloy nanoparticles in the present study. In a recent study with oleylamine-functionalized Pd nanoparticles,[63] the specific activity of 100 $mAcm^{-2}$ at +0.9V was also markedly lower than the results in the present study.

Such a remarkable performance might be accounted for by gold alloying that led to diminished bonding interactions of the nanoparticles with oxygenated species,

as compared to pure Pd. [31,32] Note that in previous studies based on EXAFS measurements, it has been found that the palladium-oxygen bond might be suppressed with increasing gold content, leading to enhanced stabilization of surface palladium towards oxide-layer formation, as a result of possible charge transfer from palladium to gold, owing to the difference in electronic negativity, as suggested in XPS measurements (Figure 4.1).[35] Additional contributions may arise from the alkyne capping ligands that form conjugated metal–ligand interfacial bonds, leading to extended spilling of metal core electrons into the ligand shells.[23,64]

However, alloying may also produce lattice strain that has been found to shift the d-band center relative to the Fermi level and affect interactions with oxygenated intermediates.[13,22] As evidenced in TEM measurements (Figure 4.2), the two metals are intimately mixed with lattice spacing in between those of pure Pd and pure Au. That is, the incorporation of gold into the nanoparticles indeed led to the expansion of the Pd crystalline lattices, which raised the d-band center of Pd and enhanced the strength of the interaction between the nanoparticle and oxygen adsorbates. This was anticipated to result in decreasing catalytic activity.

Despite these two opposing effects, it is clear from the experimental results presented above that the ORR activity was enhanced with AuPd alloy nanoparticles, as compared to pure Pd. This indicates that electronic effects from the push-and pull nature of heteroatoms (and deliberate surface engineering with the alkyne ligands) dominate the negative contributions from lattice strain. Furthermore, the volcano-shaped variation of the ORR performance with nanoparticle elemental composition

suggests that, with the incorporation of an increasing amount of gold in the nanoparticles, binding to oxygen intermediates was likely weakened, leading to enhanced activity that reached a maximum with sample 3; a further increase in gold content resulted in interactions with oxygen intermediates that were too weak and diminished the ORR activity. This is a clear demonstration of Sabatier's postulate with the peak mass activity of sample 3 representing the optimal balance between these two opposing alloying effects.

4.3 Conclusions

A series of dodecyne-capped gold–palladium alloy nanoparticles of varying elemental compositions were readily prepared by using a simple chemical reduction route. XPS measurements showed that the palladium concentrations in the nanoparticle cores varied from 65 to 100 at% and the particle diameters were found to be mostly in the range of 2–6 nm, as manifested in TEM measurements. The formation of AuPd alloy nanoparticles was also observed in UV/Vis absorption measurements, and FTIR studies confirmed the successful self-assembly of the alkyne ligands onto the nanoparticle surface. Electrochemical studies showed that, for Pd-dominant nanoparticles, the reduction of metal oxides occurred at a potential similar to that of pure Pd, whereas at relatively high gold concentrations, the peak potential was actually in between those for pure Au and pure Pd. This suggests that alloying with gold indeed weakened the interactions of palladium with oxygen species. In addition, all samples exhibited apparent electrocatalytic activity for the ORR in alkaline media, and the sample with 91.2 at% palladium exhibited the best

performance, within the context of onset potential, electron transfer number, as well as mass and specific activity. In fact, the mass activity of this sample was more than eight times better than that of commercial palladium black, and almost twice as good in terms of specific activity. This is attributed to alterations of surface electronic properties as a result of interactions between gold and palladium atoms as well as unique metal–ligand bonding interactions with the alkyne ligands. This allows for optimum binding to oxygenated intermediates and enhanced electrocatalytic activity.

4.4 References

(1) Strasser, P.; Koh, S.; Anniyev, T.; Greeley, J.; More, K.; Yu, C. F.; Liu, Z. C.; Kaya, S.; Nordlund, D.; Ogasawara, H.; Toney, M. F.; Nilsson, A.: Lattice-strain control of the activity in dealloyed core-shell fuel cell catalysts. *Nature Chemistry* **2010**, *2*, 454-460.

(2) Kitchin, J. R.; Norskov, J. K.; Barteau, M. A.; Chen, J. G.: Modification of the surface electronic and chemical properties of Pt(111) by subsurface 3d transition metals. *J Chem Phys* **2004**, *120*, 10240-6.

(3) Stephens, I. E.; Bondarenko, A. S.; Perez-Alonso, F. J.; Calle-Vallejo, F.; Bech, L.; Johansson, T. P.; Jepsen, A. K.; Frydendal, R.; Knudsen, B. P.; Rossmeisl, J.; Chorkendorff, I.: Tuning the activity of Pt(111) for oxygen electroreduction by subsurface alloying. *J Am Chem Soc* **2011**, *133*, 5485-91.

(4) Hennig, D.; GanduglіaPirovano, M. V.; Scheffler, M.: Adlayer core-level shifts of admetal monolayers on transition-metal substrates and their relation to the surface chemical reactivity. *Phys Rev B* **1996**, *53*, 10344-10347.

(5) Bzowski, A.; Sham, T. K.; Watson, R. E.; Weinert, M.: Electronic-Structure of Au and Ag Overlayers on Ru(001) - the Behavior of the Noble-Metal D-Bands. *Phys Rev B* **1995**, *51*, 9979-9984.

(6) Lima, F. H. B.; Zhang, J.; Shao, M. H.; Sasaki, K.; Vukmirovic, M. B.; Ticianelli, E. A.; Adzic, R. R.: Catalytic Activity-d-Band Center Correlation for the O2 Reduction Reaction on Platinum in Alkaline Solutions. *J Phys Chem C* **2007**, *111*, 404-410.

(7) Weinert, M.; Watson, R. E.: Core-Level Shifts in Bulk Alloys and Surface Adlayers. *Phys Rev B* **1995**, *51*, 17168-17180.

(8) Stamenkovic, V.; Mun, B. S.; Mayrhofer, K. J. J.; Ross, P. N.; Markovic, N. M.; Rossmeisl, J.; Greeley, J.; Norskov, J. K.: Changing the activity of electrocatalysts for oxygen reduction by tuning the surface electronic structure. *Angew Chem Int Edit* **2006**, *45*, 2897-2901.

(9) Hammer, B.; Norskov, J. K.: Electronic factors determining the reactivity of metal surfaces. *Surf Sci* **1995**, *343*, 211-220.

(10) Hammer, B.; Norskov, J. K.: Theoretical surface science and catalysis - Calculations and concepts. *Advances in Catalysis, Vol 45* **2000**, *45*, 71-129.

(11) Gates, J. A.; Kesmodel, L. L.: Methanol Adsorption and Decomposition on Clean and Oxygen Precovered Palladium (111). *J Catal* **1983**, *83*, 437-445.

(12) Butz, R.; Wagner, H.: Enhanced Oxygen-Adsorption on Palladium Silicide at Room-Temperature. *J Vac Sci Technol B* **1983**, *1*, 816-818.

(13) Stephens, I. E. L.; Bondarenko, A. S.; Grønbjerg, U.; Rossmeisl, J.; Chorkendorff, I.: Understanding the electrocatalysis of oxygen reduction on platinum and its alloys. *Energ Environ Sci* **2012**, *5*, 6744.

(14) Lim, D. H.; Wilcox, J.: Mechanisms of the Oxygen Reduction Reaction on Defective Graphene-Supported Pt Nanoparticles from First-Principles. *J Phys Chem C* **2012**, *116*, 3653-3660.

(15) Wagner, F. T.; Lakshmanan, B.; Mathias, M. F.: Elecrochemistry and the Future of the Automobile. *The Journal of Physical Chemistry Letters* **2010**, 2204-2219.

(16) Song, C.; Zhang, J.: *PEM Fuel Cell Electrocatalysis and Catalyst Layers: Fundamentals and Applications*, 2008.

(17) Rabis, A.; Rodriguez, P.; Schmidt, T. J.: Electrocatalysis for Polymer Electrolyte Fuel Cells: Recent Achievements and Future Challenges. *Acs Catal* **2012**, *2*, 864-890.

(18) Norskov, J. K.; Rossmeisl, J.; Logadottir, A.; Lindqvist, L.; Kitchin, J. R.; Bligaard, T.; Jonsson, H.: Origin of the Overpotential for Oxygen Reduction at a Fuel-Cell Cathode. *J Phys Chem B* **2004**, *108*, 17886-17892.

(19) Gasteiger, H. A.; Kocha, S. S.; Sompalli, B.; Wagner, F. T.: Activity benchmarks and requirements for Pt, Pt-alloy, and non-Pt oxygen reduction catalysts for PEMFCs. *Applied Catalysis B: Environmental* **2005**, *56*, 9-35.

(20) Chen, S.; Gasteiger, H. A.; Hayakawa, K.; Tada, T.; Shao-Horn, Y.: Platinum-Alloy Cathode Catalyst Degradation in Proton Exchange Membrane Fuel Cells: Nanometer-Scale Compositional and Morphological Changes. *J Electrochem Soc* **2010**, *157*, A82-A97.

(21) Higgins, D. C.; Ye, S. Y.; Knights, S.; Chen, Z. W.: Highly Durable Platinum-Cobalt Nanowires by Microwave Irradiation as Oxygen Reduction Catalyst for PEM Fuel Cell. *Electrochem Solid St* **2012**, *15*, B83-B85.

(22) Strasser, P.; Koh, S.; Anniyev, T.; Greeley, J.; More, K.; Yu, C.; Liu, Z.; Kaya, S.; Nordlund, D.; Ogasawara, H.; Toney, M. F.; Nilsson, A.: Lattice-strain control of the activity in dealloyed core-shell fuel cell catalysts. *Nat Chem* **2010**, *2*, 454-60.

(23) Liu, K.; Kang, X.; Zhou, Z.-Y.; Song, Y.; Lee, L. J.; Tian, D.; Chen, S.: Platinum nanoparticles functionalized with acetylene derivatives: Electronic conductivity and electrocatalytic activity in oxygen reduction. *J Electroanal Chem* **2013**, *688*, 143-150.

(24) He, G. Q.; Song, Y.; Liu, K.; Walter, A.; Chen, S.; Chen, S. W.: Oxygen Reduction Catalyzed by Platinum Nanoparticles Supported on Graphene Quantum Dots. *Acs Catal* **2013**, *3*, 831-838.

(25) Zhou, Z. Y.; Kang, X.; Song, Y.; Chen, S.: Enhancement of the electrocatalytic activity of Pt nanoparticles in oxygen reduction by chlorophenyl functionalization. *Chem Commun (Camb)* **2012**, *48*, 3391-3.

(26)Zhou, Z. Y.; Kang, X. W.; Song, Y.; Chen, S. W.: Ligand-Mediated Electrocatalytic Activity of Pt Nanoparticles for Oxygen Reduction Reactions. *J Phys Chem C* **2012**, *116*, 10592-10598.

(27) He, G.; Song, Y.; Phebus, B.; Liu, K.; Deming, C. P.; Hu, P.; Chen, S.: Electrocatalytic Activity of Organically Functionalized Silver Nanoparticles in Oxygen Reduction. *Sci Adv Mater* **2013**, *5*, 1727-1736.

(28) Greeley, J.; Stephens, I. E. L.; Bondarenko, A. S.; Johansson, T. P.; Hansen, H. A.; Jaramillo, T. F.; Rossmeisl, J.; Chorkendorff, I.; Norskov, J. K.: Alloys of platinum and early transition metals as oxygen reduction electrocatalysts. *Nat Chem* **2009**, *1*, 552-556.

(29) Tripković, V.; Skúlason, E.; Siahrostami, S.; Nørskov, J. K.; Rossmeisl, J.: The oxygen reduction reaction mechanism on Pt(111) from density functional theory calculations. *Electrochim Acta* **2010**, *55*, 7975-7981.

(30) Stamenkovic, V. R.; Fowler, B.; Mun, B. S.; Wang, G.; Ross, P. N.; Lucas, C. A.; Markovic, N. M.: Improved oxygen reduction activity on Pt3Ni(111) via increased surface site availability. *Science* **2007**, *315*, 493-7.

(31) Damjanovic, A.; Brusic, V.; Bockris, J. O.: Mechanism of Oxygen Reduction Related to Electronic Structure of Gold-Palladium Alloy. *The Journal of Physical Chemistry* **1967**, *71*, 2741-2742.

(32) Damjanovic, A.; Brusic, V.: Oxygen reduction at Pt-Au and Pd-Au alloy electrodes in acid solution.pdf. *Electrochim Acta* **1967**, *12*, 1171-1184.

(33) Sabatier, P.: Announcement. Hydrogenation and dehydrogenation for catalysis. *Ber Dtsch Chem Ges* **1911**, *44*, 1984-2001.

(34) Nie, M.; Shen, P. K.; Wei, Z.: Nanocrystaline tungsten carbide supported Au–Pd electrocatalyst for oxygen reduction. *J Power Sources* **2007**, *167*, 69-73.

(35) Koenigsmann, C.; Sutter, E.; Adzic, R. R.; Wong, S. S.: Size- and Composition-Dependent Enhancement of Electrocatalytic Oxygen Reduction Performance in Ultrathin Palladium-Gold (Pd1-xAux) Nanowires. *J Phys Chem C* **2012**, *116*, 15297-15306.

(36) Maye, M. M.; Kariuki, N. N.; Luo, J.; Han, L.; Njoki, P.; Wang, L. Y.; Lin, Y.; Naslund, H. R.; Zhong, C. J.: Electrocatalytic reduction of oxygen: Gold and gold-platinum nanoparticle catalysts prepared by two-phase protocol. *Gold Bull* **2004**, *37*, 217-+.

(37) Metin, O.; Sun, X. L.; Sun, S. H.: Monodisperse gold-palladium alloy nanoparticles and their composition-controlled catalysis in formic acid dehydrogenation under mild conditions. *Nanoscale* **2013**, *5*, 910-912.

(38) Jablonski, A.; Overbury, S. H.; Somorjai, G. A.: Surface Composition of Gold-Palladium Binary Alloy System. *Surf Sci* **1977**, *65*, 578-592.

(39) Kim, J. H.; Bryan, W. W.; Chung, H. W.; Park, C. Y.; Jacobson, A. J.; Lee, T. R.: Gold, Palladium, and Gold-Palladium Alloy Nanoshells on Silica Nanoparticle Cores. *Acs Appl Mater Inter* **2009**, *1*, 1063-1069.

(40) Dimitratos, N.; Lopez-Sanchez, J. A.; Meenakshisundaram, S.; Anthonykutty, J. M.; Brett, G.; Carley, A. F.; Taylor, S. H.; Knight, D. W.; Hutchings, G. J.: Selective formation of lactate by oxidation of 1,2-propanediol using gold palladium alloy supported nanocrystals. *Green Chem* **2009**, *11*, 1209-1216.

(41) Jiang, J. H.; Kucernak, A.: Probing anodic reaction kinetics and interfacial mass transport of a direct formic acid fuel cell using a nanostructured palladium-gold alloy microelectrode. *Electrochim Acta* **2009**, *54*, 4545-4551.

(42) Simonov, A. N.; Plyusnin, P. E.; Shubin, Y. V.; Kvon, R. I.; Korenev, S. V.; Parmon, V. N.: Hydrogen electrooxidation over palladium-gold alloy: Effect of pretreatment in ethylene on catalytic activity and CO tolerance. *Electrochim Acta* **2012**, *76*, 344-353.

(43) Paalanen, P.; Weckhuysen, B. M.; Sankar, M.: Progress in controlling the size, composition and nanostructure of supported gold–palladium nanoparticles for catalytic applications. *Catal Sci Technol* **2013**, *3*, 2869.

(44) Devarajan, S.; Bera, P.; Sampath, S.: Bimetallic nanoparticles: a single step synthesis, stabilization, and characterization of Au-Ag, Au-Pd, and Au-Pt in sol-gel derived silicates. *J Colloid Interface Sci* **2005**, *290*, 117-29.

(45) Yuan, X.; Sun, G.; Asakura, H.; Tanaka, T.; Chen, X.; Yuan, Y.; Laurenczy, G.; Kou, Y.; Dyson, P. J.; Yan, N.: Development of palladium surface-enriched heteronuclear Au-Pd nanoparticle dehalogenation catalysts in an ionic liquid. *Chemistry* **2013**, *19*, 1227-34.

(46) Zhang, G.; Zhou, H.; An, C.; Liu, D.; Huang, Z.; Kuang, Y.: Bimetallic palladium–gold nanoparticles synthesized in ionic liquid microemulsion. *Colloid Polym Sci* **2012**, *290*, 1435-1441.

(47) Liu, H. F.; Mao, G. P.; Meng, S. J.: Preparation and Characterization of the Polymer-Protected Palladium Gold Colloidal Bimetallic Catalysts. *J Mol Catal* **1992**, *74*, 275-284.

(48) Wagner, C. D.; Riggs, W. M.; Davis, L. E.; Moulder, J. F.; E., M. G.: Handbook of X-Ray Photoelectron Spectroscopy. **1979**.

(49) Cerritos, R. C.; Guerra-Balcázar, M.; Ramírez, R. F.; Ledesma-García, J.; Arriaga, L. G.: Morphological Effect of Pd Catalyst on Ethanol Electro-Oxidation Reaction. *Materials* **2012**, *5*, 1686-1697.

(50) Chen, S. W.; Templeton, A. C.; Murray, R. W.: Monolayer-protected cluster growth dynamics. *Langmuir* **2000**, *16*, 3543-3548.

(51) Creighton, J. A.; Eadon, D. G.: Ultraviolet Visible Absorption-Spectra of the Colloidal Metallic Elements. *J Chem Soc Faraday T* **1991**, *87*, 3881-3891.

(52) Chen, W.; Zuckerman, N. B.; Kang, X. W.; Ghosh, D.; Konopelski, J. P.; Chen, S. W.: Alkyne-Protected Ruthenium Nanoparticles. *J Phys Chem C* **2010**, *114*, 18146-18152.

(53) Kang, X. W.; Zuckerman, N. B.; Konopelski, J. P.; Chen, S. W.: Alkyne-Stabilized Ruthenium Nanoparticles: Manipulation of Intraparticle Charge Delocalization by Nanoparticle Charge States. *Angew Chem Int Edit* **2010**, *49*, 9496-9499.

(54) Kang, X. W.; Zuckerman, N. B.; Konopelski, J. P.; Chen, S. W.: Alkyne-Functionalized Ruthenium Nanoparticles: Ruthenium-Vinylidene Bonds at the Metal-Ligand Interface. *J Am Chem Soc* **2012**, *134*, 1412-1415.

(55) Rand, D. A. J.; Woods, R.: The Nature of Adsorbed Oxygen on Rhodium, Palladium, and Gold Electrodes. *J Electroanal Chem* **1971**, *31*, 29-38.

(56) Schumpe, A.; Adler, I.; Deckwer, W. D.: Solubility of Oxygen in Electrolyte-Solutions. *Biotechnology and Bioengineering* **1978**, *20*, 145-150.

(57) Anastasijevic, N. A.; Dimitrijevic, Z. M.; Adzic, R. R.: Oxygen reduction on a ruthenium electrode in alkaline electrolytes. **1886**, 351.

(58) Markovic, N. M.; Gasteiger, H. A.; Grgur, B. N.; Ross, P. N.: Oxygen reduction reaction on Pt(111): effects of bromide. *Journal of Electroanalytical Chemistry* **1999**, *467*, 157-163.

(59) Sekol, R. C.; Li, X.; Cohen, P.; Doubek, G.; Carmo, M.; Taylor, A. D.: Silver palladium core–shell electrocatalyst supported on MWNTs for ORR in alkaline media. *Applied Catalysis B: Environmental* **2013**, *138-139*, 285-293.

(60) Hu, G.; Nitze, F.; Gracia-Espino, E.; Ma, J.; Barzegar, H. R.; Sharifi, T.; Jia, X.; Shchukarev, A.; Lu, L.; Ma, C.; Yang, G.; Wagberg, T.: Small palladium islands embedded in palladium-tungsten bimetallic nanoparticles form catalytic hotspots for oxygen reduction. *Nat Commun* **2014**, *5*, 5253.

(61) Wang, X.; Kariuki, N.; Niyogi, S.; Smith, M.; Myers, D. J.; Hofmann, T.; Zhang, Y.; Bar, M.; Heske, C.: Bimetallic Palladium-Base Metal Nanoparticle Oxygen Reduction Electrocatalysts. *Ecs Transactions* **2008**, *16*, 109-119.

(62) Jang, J.-H.; Pak, C.; Kwon, Y.-U.: Ultrasound-assisted polyol synthesis and electrocatalytic characterization of PdxCo alloy and core–shell nanoparticles. *J Power Sources* **2012**, *201*, 179-183.

(63) Shi, Y.; Yin, S.; Ma, Y.; Lu, D.; Chen, Y.; Tang, Y.; Lu, T.: Oleylamine-functionalized palladium nanoparticles with enhanced electrocatalytic activity for the oxygen reduction reaction. *J Power Sources* **2014**, *246*, 356-360.

(64) Liu, K.; Song, Y.; Chen, S.: Electrocatalytic activities of alkyne-functionalized copper nanoparticles in oxygen reduction in alkaline media. *J Power Sources* **2014**, *268*, 469-475.

Chapter 5

Graphene Quantum Dots-Supported Palladium Nanoparticles for Efficient Electrocatalytic Reduction of Oxygen in Alkaline Media

5.1 Introduction

Among the powerful methods to manipulate metal nanoparticle properties, especially for electrocatalysis optimization is the utilization of an active support. Experimentally, to achieve proper article dispersion and to limit current losses from catalytic sites to the electrode, metal nanoparticle catalysts are generally supported on a stable, high surface area, conducting material such as the commonly utilized Vulcan supports.[1,2] Yet, as such commercial supports encounter issues with stability and purity, other carbon materials have been examined as effective supporting substrates for fuel cell catalysts, such as mesoporous carbon,[3,4] graphene derivatives (e.g., graphene oxide and GQDs),[5,6] and one dimensional carbon supports such as carbon nanotubes[7,8] and carbon nanofibers.[9,10] Thus far, graphene derivatives, specifically GQDs, have been widely used and exhibited promising properties as metal nanoparticle supports due to their chemical inertness, high electrical conductivity, and large surface area.[11-13] More interestingly, these GQD supports have proven to impart electronic interactions with the metal nanoparticles so as to modulate the metal nanoparticle ORR activity.[5,6]

Generally, supports are perceived to play a passive role in providing conduction of currents and dispersion of metal nanoparticles but not significantly influencing the particle electrochemical properties. The idea of electronic interactions between the nanoparticles and supporting materials highlights the main difference between a passive and active support.[14] For instance, GQDs are generally synthesized by chemical oxidation and exfoliation of graphitic precursors, which

results in a number of oxygen functional groups on the surface.[15,16] It has been argued that these oxygen defects may result in diminished stability of the graphitic materials through disruption of the sp2 backbone and are therefore commonly removed through chemical and thermal treatments.[7,8] However, there have been an increasing number of studies where positive contributions are observed from oxygen functional groups on GQDs to metal nanoparticle electrocatalysis.[5,6,8,15] It is proposed that the GQD oxygenated defects provide natural sites for metal particle adhesion allowing for more intimate contacts between particle and support.[8] Additionally, recent DFT studies suggest that the defect groups may pull electrons from the metal nanoparticles, leading to more favorable interactions between the active sites and oxygenated intermediates (OIs).[17]

Since the activity and durability of metal electrocatalysts such as palladium and platinum are limited by strong binding with OIs, the influence of associated GQDs and the electronegative moieties, may lend similar enhancements as do alloys and organic functionalization. In fact, we have observed that GQD-supported Pt nanoparticles (Pt/GQD) exhibited an ORR onset potential 70 mV more positive than similarly sized Pt particles dispersed on commercial carbon supports.[5] The abundance of oxygen groups found on the GQDs are thought to be responsible for the improved activity through diminished electron density on Pt surface atoms and thus improved interactions with OIs. We then identified an optimal defect concentration in a subsequent study where Pt/GQD composites were subject to hydrothermal treatments at temperatures ranging from 140 to 200 °C for 3 to 12 h in order to

manipulate the defect concentration.[18] The sample with about 20% structural defects exhibited an activity over 10 times that of samples with too low or too high levels of oxygen defects.[6]

As a platinum group metal, palladium is also a well-studied electrocatalyst for ORR. Because the d-band structure, and hence adsorptive properties, of palladium and platinum are similar, the diverse methods for improving the ORR activity of platinum may also be applicable for palladium.[19-22] Numerous reports have indeed detailed the synthesis and characterization of functional nanocomposites based on palladium nanoparticles supported on graphitic materials such as graphene sheets, GQDs, and nanohorns,[23-25] and their ORR activity has been studied.[11,26] However, thus far there has been no systematic study to optimize the ORR activity within the context of GQD defect concentration, to the best of our knowledge. This is the primary motivation of the present study where the goal is to identify optimal conditions for GQD supported Pd nanoparticles (Pd/GQD) for ORR electrocatalysis. Note that in the volcano plot, palladium binds to OIs more strongly than Pt, thus more substantial electron withdrawing from GQD structural defects is anticipated to achieve marked activity enhancement of the Pd/GQD composites.[20,27] That is, the optimal defect concentration is most likely higher for Pd/GQD than for Pt/GQD.[6]

Experimentally, carbon pitch fibers were thermally and chemically treated in acids to yield stable water-soluble GQDs.[15] Pd/GQD nanocomposites were then synthesized by thermolytic reduction of $PdCl_2$ in 1,2-propanediol in the presence of GQDs and then underwent hydrothermal treatment at controlled temperatures (140 to

200 °C) for 12 h to manipulate the defect concentrations. Since palladium is catalytically active in decarboxylation,[28,29] we should expect a more efficient defect removal than would be at high temperatures alone. The structural details were then characterized by TEM, XPS, and Raman measurements, and the ORR activity was evaluated in alkaline media. Notably, the series of Pd/GQD nanocomposites all exhibited apparent ORR activity, and the activity displayed a clear volcano-shaped variation with the GQD defect concentration. The fact that the GQD defect concentration at the peak ORR activity was higher than that observed for Pt/GQD further confirmed that manipulation of the electronic density of metal nanoparticles by GQD structural defects might be a unique, effective mechanism in enhancing and optimizing the ORR performance.

5.2 Results and Discussion

Figure 5.1 (left panels) depicts a representative TEM micrograph for each of the series of Pd/GQD samples prepared above. It is shown from panel (A) that the as-prepared Pd/GQD composites exhibited a raspberry-like morphology, where a number of small, spherical nanoparticles of ca. 8 nm in diameter clustered together to form large aggregates from 50 to 100 nm. Such behaviors have also been observed with palladium nanoparticles grown on carbon nanoparticles[30] and PdPt nanodendrites.[31] Hydrothermal treatments of the Pd/GQD at 140 and 160 °C did not lead to marked variations of the ensemble morphologies, as depicted in panels (B) and (C). However, at higher hydrothermal temperatures, e.g., 180 °C in panel (D) and 200 °C in panel E, individual nanoparticles became increasingly difficult to

resolve, and the particles appeared to fuse into much larger agglomerates, forming porous network nanostructures.

The discrepancy of the Pd/GQD nanocomposite structures might be accounted for by the nanoparticle growth dynamics.[32] Chemically produced GQDs are known to include a number of structural defects (i.e., oxygenated groups) that may serve as the anchoring site for metal ion chelation and the growth of metal nanoparticles. Hydrothermal treatment is an effective method in (partially) removing the structural defects and restoring the sp^2 character.[33,34] Therefore, at higher hydrothermal temperatures, the GQD defects became more effectively removed, leading to less efficient anchoring and passivation of the Pd nanoparticles and hence larger sizes of the metal nanostructures. Further contributions may be ascribed to the Pd nanoparticles formed during the hydrothermal process, which are well-known decarboxylation catalysts,[29] as carboxylic acids have been recognized to be a major oxygenated component of the various oxygenated groups on GQDs (vide infra). This is consistent with the experimental observations. Note that in prior DFT studies it has been found that a hyper cross-linked polystyrene matrix provides unique pockets for palladium nucleation, which are modeled as phenyl groups surrounding the nucleation site, leading to manipulation of the shapes and properties of the Pd nanoparticles.[35] The formation of Pd/GQD likely followed the similar mechanism.

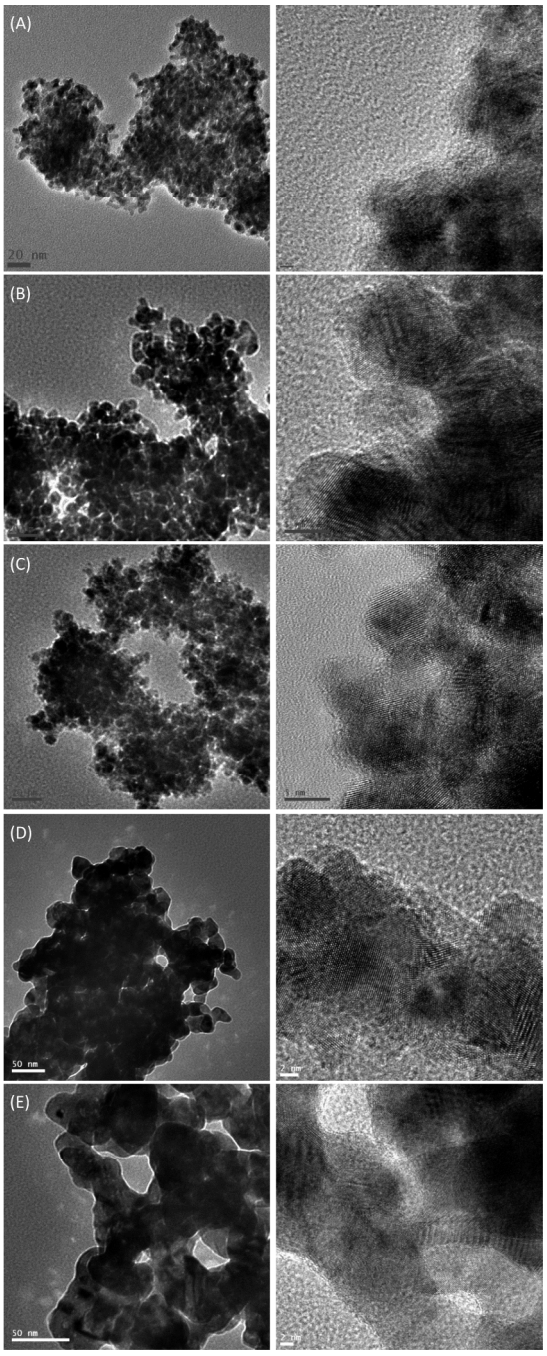

Figure 5.1. (Left) Representative TEM images of the Pd/GQD nanoparticles (A) before and after hydrothermal treatment at (B) 140 °C, (C) 160 °C, (D) 180 °C, and (E) 200 °C. Scale bars are 20 nm in panels (A) to (C) and 50 nm in (D) and (E). The corresponding high-resolution TEM images are shown in the right panels. Scale bars are 5 nm in panels (A) – (C) and 2 nm in (D) and (E).

High-resolution TEM studies further confirmed that that $PdCl_2$ was indeed reduced into metallic Pd, forming Pd/GQD nanocomposites. From the respective HRTEM images in Figure 5.1 (right panels), one can see highly crystalline domains were embedded within a non-crystalline matrix. The former is most likely metallic Pd where the well-defined lattice fringes exhibited an interlayer spacing of 0.23 nm, in good agreement with that of the (111) crystalline planes of fcc Pd; whereas the latter may be ascribed to GQDs that were difficult to identify in the TEM images because of their low electron density and poor crystallinity.

Further structural characterization was carried out with XPS measurements. Figure 5.2 shows the high-resolution scans of the (left panels) C 1s and (right panels) Pd 3d electrons of the Pd/GQD composites before and after hydrothermal treatment at varied temperatures. It is shown from the left panels that deconvolution of the carbon 1s spectra yields four components, graphitic (C=C, 284.8 eV), alcoholic (C–OH, 285.5 eV), carbonylic (C=O, 287.5 eV), and carboxylic (COOH, 288.5 eV). The three oxygen-containing groups can be viewed as structural defects that disrupt the planar graphitic backbone and may be removed to restore the Csp^2 nature.[7,8] On the basis of the integrated peak areas, one can see apparent impacts of hydrothermal temperature on the carbon compositions, where the concentration of oxygenated species decreased with increasing hydrothermal temperature. Specifically, the fraction of oxygenated carbons (i.e., structural defects) in GQDs decreased from 64.1% for the as-prepared sample to 58.0% when treated at 140 °C, 45.7% at 160 °C, 50.5% at 180 °C, and 41.0% at 200 °C (Table 5.1).

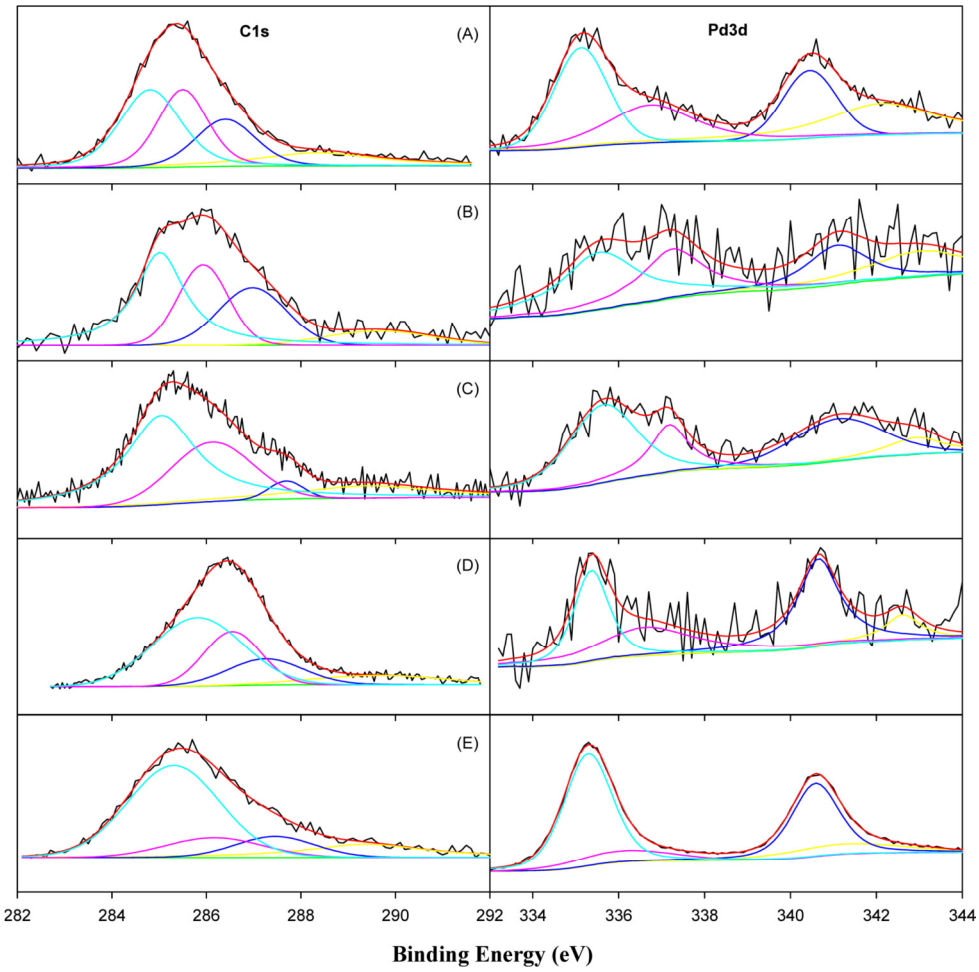

Figure 5.2. High resolution XPS spectra for the C 1s and Pd 3d electrons for Pd/GQD (A) before and after hydrothermal treatment at (B) 140 °C, (C) 160 °C, (D) 180 °C, and (E) 200 °C. Black curves are experimental data and colored curves are deconvolution fits.

Oxygen defects are thought to provide anchoring points for particle attachment but have also been found theoretically[17] and experimentally[5,6] to impart electronic effects on the neighboring metal particles. To reveal the nature of such interactions, high resolution XPS scans of Pd 3d electrons were also acquired and analyzed for each sample. In the right panels of Figure 5.2, the peaks at ca. 335.0 eV (light blue curve) and 340.5 eV (dark blue curve) may be ascribed to the 3d5/2 and

3d3/2 electrons of metallic palladium, respectively.[36] Peaks colored with pink and yellow represent electron-deficient palladium, which likely results from charge transfer from Pd to electronegative oxygen of the GQDs. As the area of each curve represents the abundance of the corresponding component, it is clear that the hydrothermal temperature had a strong influence on the relative abundance of electron-deficient palladium. In fact, analysis of the XPS data for palladium was very consistent with that for carbon. The as-prepared sample shows the largest relative signal from electron-deficient palladium likely from the high level of oxygen groups in the GQDs. At higher hydrothermal temperatures, the GQD oxygen groups are more effectively removed, leading to diminished signals from electron-deficient palladium.

Pd/GQD	Defect %[a]	I_D/I_G[b]	Pd wt %
As prepared	64.1	1.29	36.7
140 ˚C	58.0	1.19	17.7
160 ˚C	45.7	1.01	32.0
180 ˚C	50.5	1.09	13.1
200 ˚C	41.0	0.42	66.4

Table 5.1. Summary of Structural Defects and Compositions in Pd/GQD Nanocomposites. [a]From XPS measurements in Figure 5.2. [b]From Raman measurements in Figure 5.3.

Within the series, Pd/GQD-200 exhibited almost no peaks in the high-energy region, most probably due to the catalytic decarboxylation of GQDs at elevated temperatures.[25,26] In addition, based on the integrated peak areas, the mass fractions of Pd in the nanocomposites were quantitatively estimated to be 36.7% for the as-

prepared sample, 17.7% for Pd/GQD-140, 32.0% for Pd/GQD-160, 13.1% for Pd/GQD-180, and 66.4% for Pd/GQD-200 (Table 5.1).

To further probe the nature of GQD defects, Raman spectroscopy was utilized. Specifically, graphitic materials generally display prominent bands arising from the graphitic (G) and defect (D) domains.[37,38] The intensity ratio of these two bands (I_D/I_G) may be used as a quantitative descriptor for defect concentration. A close-up of the region containing the D and G bands is given in Figure 5.3 for each sample, and it is apparent that each sample displays D and G bands at 1385 and 1590 cm^{-1}, respectively.

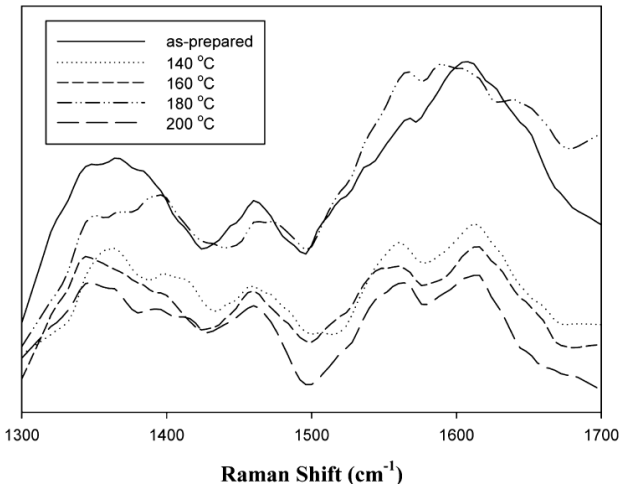

Figure 5.3. Raman spectra for Pd/GQD nanocomposites before and after hydrothermal treatment at different temperatures (specified in figure legends).

Furthermore, the I_D/I_G value is strongly dependent on the hydrothermal temperature. For the as-prepared Pd/GQD sample, the I_D/I_G ratio was estimated to be 1.29, which decreased to 1.19 for Pd/GQD-140, 1.01 for Pd/GQD-160, 1.09 for Pd/GQD-180, and 0.42 for Pd/GQD-200 (Table 5.1), indicating increasingly

dominant graphitic characters of the GQDs at increasing hydrothermal temperature. These results are in strong agreement with defect analysis by XPS measurements (Figure 5.2). Similar behaviors have also been observed in the previous study with Pt/GQD nanocomposites.[6]

Interestingly, the series of Pd/GQD nanocomposites all exhibited apparent electrocatalytic activity toward ORR. A same amount (20 μg) of the Pd/GQD catalysts was dropcast onto a glassy carbon disk for electrochemical evaluations, corresponding to a palladium mass loading of 7.2 μg Pd for Pd/GQD, 3.5 μg Pd for Pd/GQD-140, 6.4 μg Pd for Pd/GQD-160, 2.6 μg Pd for Pd/GQD-180, and 13 μg Pd for Pd/GQD-200, as determined by XPS measurements (Table 5.1). The electrodes were then subject to electrochemical activation by rapid potential cycling between +0.25 V and +1.6 V at 500 mV/s in a nitrogen saturated 0.1 M NaOH solution. Figure 5.4 A depicts the corresponding steady-state cyclic voltammograms, where the potential range was chosen to avoid the adsorption/absorption/desorption of hydrogen on Pd surfaces. All samples show a voltammetric peak around +0.73 V vs RHE in the anodic scan and a large sharp peak around +0.57 V in the cathodic scan. These represent the formation and removal of an oxide monolayer on the palladium nanoparticle surface, respectively. The electrochemical surface area (ECSA) was then extracted from the integrated charges of the oxide reduction peak at 13.1 m^2/g Pd for the as-prepared Pd/GQD sample, 41.2 m^2/g Pd for Pd/GQD-140, 20.6 m^2/g Pd for Pd/ GQD-160, 33.3 m^2/g Pd for Pd/GQD-180, and 7.5 m^2/g Pd for Pd/GQD-200. Of note is that the Pd/GQD-140 sample exhibited the largest ECSA among the series,

whereas the Pd/GQD-200 showed the smallest, which might be ascribed to the effective removal of oxygenated defects at high temperatures and hence restacking of the graphene nanosheets that limited the electrochemical accessibility of the Pd surfaces.

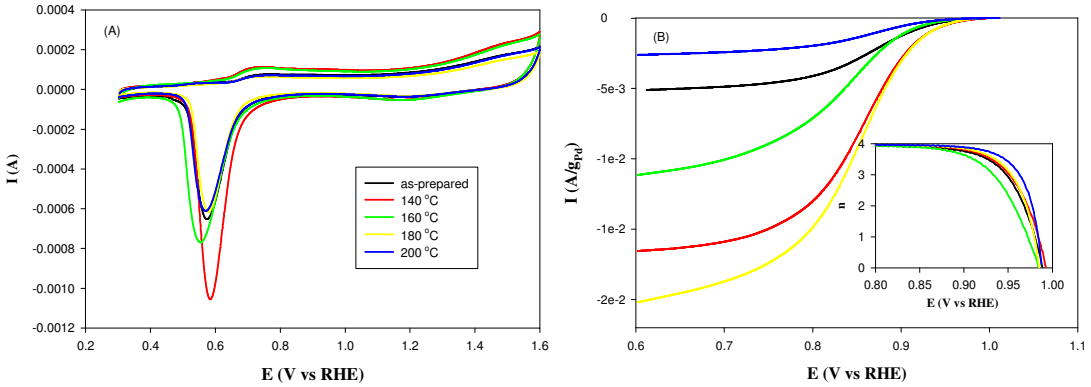

Figure 5.4. (A) Cyclic voltammograms of a glassy carbon electrode modified with different Pd/GQD nanoparticles in nitrogen-saturated 0.1 M NaOH. Potential sweep rate 100 mV/s. (B) RDE voltammograms of the same electrodes with the electrolyte saturated with oxygen. Inset is the corresponding number of electron transfer during ORR calculated from the RRDE voltammograms at 1600 rpm. Electrode rotation rate 1600 rpm. DC ramp 10 mV/s. Catalyst loading 20 μg.

The ORR activity of the Pd/GQD samples was then evaluated in oxygen-saturated 0.1 M NaOH. Figure 5.4 B shows the RDE voltammograms of a glassy carbon electrode modified with a calculated amount of the various Pd/GQD nanocomposites at the rotation rates of 1600 rpm. From the figure, it is apparent that each sample displayed a nonzero disk current as the electrode potential was swept in the negative direction, signifying oxygen reduction catalyzed by the Pd/GQD particles. Yet the catalytic performance displayed a marked difference among the Pd/GQD samples. For instance, the onset potential increased in the order of

Pd/GQD-160 (+0.86 V) < as-prepared (+0.88 V) < Pd/GQD-140 (+0.89 V) < Pd/GQD-200 ≈ Pd/GQD-180 (+0.90 V). The limiting currents (I_{lim}) also varied markedly. For instance, at the electrode potential of +0.6 V, I_{lim} can be estimated to be 5.15×10^{-3} A/g Pd for as-prepared Pd/GQD, 1.65×10^{-2} A/g Pd for Pd/GQD-140, 1.11×10^{-2} A/g Pd for Pd/GQD-160, 2.02×10^{-2} A/g Pd for Pd/GQD-180, and 2.61×10^{-3} A/g Pd for Pd/GQD-200. These results suggest that the Pd/GQD-180 sample stood out as the best catalyst among the series.

Moreover, the limiting current of the Pd/GQD modified electrodes increased with rotation rate, which were roughly 2 orders of magnitude larger than the ring currents. This signifies a low level of undesired peroxide species produced during oxygen reduction. That is, ORR proceeded largely by the 4-electron reduction pathway. In fact, the numbers of electron transfer (n) in ORR were all close to 4 at potentials more negative than ca. + 0.90 V (inset to Figure 5.4 B), which were quantified by the disk (I_{Disk}) and ring (I_{Ring}) currents, $n = 4I_{Disk}/(I_{Disk} + I_{Ring}/N)$, with N being the collection efficiency of the electrode (40%).67 Yet a small discrepancy canbe seen. For instance, at +0.90 V, n = 3.76 for as-produced Pd/GQD, 3.81 for Pd/GQD-140, 3.64 for Pd/GQD-160, 3.85 for Pd/GQD-180, and 3.89 for Pd/GQD-200.

Further insights into the electron-transfer kinetics were obtained from Koutecky–Levich (K-L) analysis of the RRDE data. Specifically, the disk current may include contributions from both diffusion-controlled (I_d) and kinetic-controlled (I_k) components, as is shown in equations 5.1-5.3,[39]

$$\frac{1}{I_D} = \frac{1}{I_k} + \frac{1}{I_d} = \frac{1}{I_k} + \frac{1}{B\omega^{1/2}} \quad (5.1)$$

$$B = 0.62nFAC_O D_O^{2/3} \nu^{-1/6} \quad (5.2)$$

$$I_k = nAFkC_O \quad (5.3)$$

where ω is the electrode rotation rate, n is electron-transfer number, F is the Faraday constant (96485 C mol^{-1}), A is the geometric surface area of the electrode, C_O is the oxygen concentration in O_2-saturated solutions (1.26×10^{-6} mol/cm^3),[40] D_O is the diffusion coefficient of O_2 in 0.1 M NaOH aqueous solution (1.93×10^{-5} cm^2/s),[41] ν is the kinematic viscosity of the solution (1.009×10^{-2} cm^2/s), [42] and k is the electron-transfer rate constant.

The K-L plots all exhibited good linearity suggesting first-order reaction of ORR with the oxygen concentration, and from the y intercepts, the kinetic currents (I_k) were quantitatively estimated, which were depicted in the Tafel plot (Figure 5.5) where the kinetic current density (J_k) was obtained by normalizing I_k to the respective ECSA. One can see that J_k increased markedly with increasingly negative electrode potential, and the Tafel slope varied somewhat among the series of Pd/GQD samples at 96.2 mV/dec for the as-prepared sample, 71.6 mV/dec for Pd/GQD-140, 84.4 mV/dec for Pd/GQD-160, 71.6 mV/dec for Pd/GQD-180, and 82.2 mV/dec for Pd/GQD-200, signifying that the first electron reduction of adsorbed oxygen was likely the rate-determining step for ORR at Pd/GQD. Furthermore, it can be seen that the Pd/GQD-180 sample exhibited the largest J_k at all potentials among the series. For instance, at +0.90 V, J_k = 0.98 A/m^2 for Pd/GQD, 0.71 A/m^2 for Pd/GQD-140,

0.56 A/m^2 for Pd/GQD-160, 1.08 A/m^2 for Pd/GQD-180, and 0.94 A/m^2 for Pd/GQD-200. Mass-specific activity exhibited a similar variation at 8.6 A/g Pd for the as-prepared Pd/GQD, 20.3 A/g Pd for Pd/GQD-140, 7.7 A/g Pd for Pd/GQD-160, 23.9 A/g Pd for Pd/GQD-180, and 4.7 A/g Pd for Pd/GQD-200. From the figure inset, it is shown that the ORR activity actually exhibited a volcano-shaped variation with the GQD structural defects and the Pd/GQD-180 sample represented the optimal interactions between the GQD structural defects and the palladium nanoparticles that led to most favored binding interactions of OIs on Pd surfaces and hence the best ORR performance among the series.

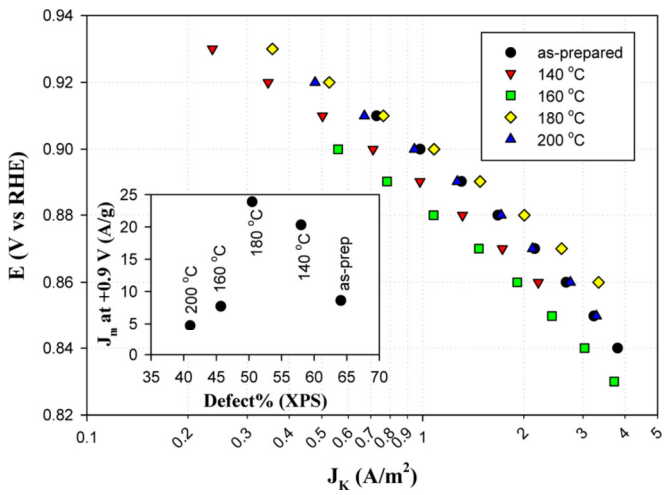

Figure 5.5. Tafel plot of Pd/GQD nanocomposites in ORR electrocatalysis. Data are obtained from the respective K-L plots. Inset is the mass-specific activity of the various Pd/GQD samples.

Note that the overall trend is analogous to that observed with the Pt/GQD counterparts; however, the peak ORR performance of the Pd/GQD nanocomposites corresponded to about 50% structural defects within the GQDs (Table 5.1), which

was markedly higher than that (ca. 20%) observed with Pt/GQD.[6] This may be accounted for by the stronger binding interactions of OIs to Pd surfaces than to Pt, as predicted in the volcano plot, such that a higher defect concentration is needed to weaken the interactions of OIs to Pd for maximal ORR activity.[6,43] This is also consistent with previous research on platinum functionalized with electron withdrawing moieties as well as the standing d band theory description of adsorbate−catalyst interactions.[44]

5.3 Conclusion

In this study, Pd/GQD nanocomposites were synthesized via thermolytic reduction of metal salts in the presence of GQDs and underwent hydrothermal treatment for 12 h at 140, 160, 180, or 200 °C to allow for the controlled removal of oxygen defects and the restoration of the planar Csp^2 backbone. TEM studies showed a raspberry-shaped morphology, which seemed to smooth out as hydrothermal temperature increased as a result of increasing defect removal and thus removal of anchoring points for particle attachment, as indicated by XPS and Raman measurements, which showed good correlation. Voltammetric tests revealed that the defect concentration had a significant impact on the ORR activity with the best sample (Pd/GQD-180) determined on the basis of onset potential, number of electron transfer, specific activity, and mass activity. The peak activity was reached with the optimal level of defects that provided sufficient electron withdrawal from the Pd particles so that the tight binding to OIs was deliberately diminished but would not pull too many electrons away so as to limit the adsorption of oxygen intermediates.

The results further confirm the significance of metal–substrate interactions in the manipulation of their electrocatalytic activity, a fundamental insight that may be exploited for the rational design and engineering of nanocomposite catalysts for fuel cell electrochemistry.

5.4 References

(1) Sharma, S.; Pollet, B. G.: Support materials for PEMFC and DMFC electrocatalysts-A review. *J Power Sources* **2012**, *208*, 96-119.

(2) Zhou, X. J.; Qiao, J. L.; Yang, L.; Zhang, J. J.: A Review of Graphene-Based Nanostructural Materials for Both Catalyst Supports and Metal-Free Catalysts in PEM Fuel Cell Oxygen Reduction Reactions. *Adv Energy Mater* **2014**, *4*.

(3) Joo, S. H.; Kwon, K.; You, D. J.; Pak, C.; Chang, H.; Kim, J. M.: Preparation of high loading Pt nanoparticles on ordered mesoporous carbon with a controlled Pt size and its effects on oxygen reduction and methanol oxidation reactions. *Electrochim Acta* **2009**, *54*, 5746-5753.

(4) Ding, J.; Chan, K. Y.; Ren, J. W.; Xiao, F. S.: Platinum and platinum-ruthenium nanoparticles supported on ordered mesoporous carbon and their electrocatalytic performance for fuel cell reactions. *Electrochim Acta* **2005**, *50*, 3131-3141.

(5) He, G. Q.; Song, Y.; Liu, K.; Walter, A.; Chen, S.; Chen, S. W.: Oxygen Reduction Catalyzed by Platinum Nanoparticles Supported on Graphene Quantum Dots. *Acs Catal* **2013**, *3*, 831-838.

(6) Song, Y.; Chen, S. W.: Graphene Quantum-Dot-Supported Platinum Nanoparticles: Defect-Mediated Electrocatalytic Activity in Oxygen Reduction. *Acs Appl Mater Inter* **2014**, *6*, 14050-14060.

(7) Wang, J. J.; Yin, G. P.; Shao, Y. Y.; Wang, Z. B.; Gao, Y. Z.: Investigation of further improvement of platinum catalyst durability with highly graphitized carbon nanotubes support. *J Phys Chem C* **2008**, *112*, 5784-5789.

(8) Hull, R. V.; Li, L.; Xing, Y. C.; Chusuei, C. C.: Pt nanoparticle binding on functionalized multiwalled carbon nanotubes. *Chem Mater* **2006**, *18*, 1780-1788.

(9) Jia, B.; Wang, Y.; Yao, Y.; Xie, Y.: A new indicator on the impact of large-scale circulation on wintertime particulate matter pollution over China. *Atmos Chem Phys* **2015**, *15*, 11919-11929.

(10) Hsin, Y. L.; Hwang, K. C.; Yeh, C. T.: Poly(vinylpyrrolidone)-modified graphite carbon nanofibers as promising supports for PtRu catalysts in direct methanol fuel cells. *J Am Chem Soc* **2007**, *129*, 9999-10010.

(11) Seo, M. H.; Choi, S. M.; Kim, H. J.; Kim, W. B.: The graphene-supported Pd and Pt catalysts for highly active oxygen reduction reaction in an alkaline condition. *Electrochem Commun* **2011**, *13*, 182-185.

(12) Geim, A. K.; Novoselov, K. S.: The rise of graphene. *Nat Mater* **2007**, *6*, 183-191.

(13) Vinayan, B. P.; Nagar, R.; Rajalakshmi, N.; Ramaprabhu, S.: Novel Platinum-Cobalt Alloy Nanoparticles Dispersed on Nitrogen-Doped Graphene as a Cathode Electrocatalyst for PEMFC Applications. *Adv Funct Mater* **2012**, *22*, 3519-3526.

(14) Hu, P. G.; Liu, K.; Deming, C. P.; Chen, S. W.: Multifunctional Graphene-Based Nanostructures for Efficient Electrocatalytic Reduction of Oxygen. *Journal of Chemical Technology and Biotechnology* **2015**, xx.

(15) He, D. P.; Cheng, K.; Peng, T.; Sun, X. L.; Pan, M.; Mu, S. C.: Bifunctional effect of reduced graphene oxides to support active metal nanoparticles for oxygen reduction reaction and stability. *J Mater Chem* **2012**, *22*, 21298-21304.

(16) Li, Y.; Zhao, Y.; Cheng, H.; Hu, Y.; Shi, G.; Dai, L.; Qu, L.: Nitrogen-doped graphene quantum dots with oxygen-rich functional groups. *J Am Chem Soc* **2012**, *134*, 15-8.

(17) Lim, D. H.; Wilcox, J.: Mechanisms of the Oxygen Reduction Reaction on Defective Graphene-Supported Pt Nanoparticles from First-Principles. *J Phys Chem C* **2012**, *116*, 3653-3660.

(18) Tian, L.; Song, Y.; Chang, X. J.; Chen, S. W.: Hydrothermally enhanced photolu minescence of carbon nanoparticles. *Scripta Mater* **2010**, *62*, 883-886.

(19) Shao, M.; Odell, J.; Humbert, M.; Yu, T.; Xia, Y.: Electrocatalysis on Shape-Controlled Palladium Nanocrystals: Oxygen Reduction Reaction and Formic Acid Oxidation. *The Journal of Physical Chemistry C* **2013**, *117*, 4172-4180.

(20) Lima, F. H. B.; Zhang, J.; Shao, M. H.; Sasaki, K.; Vukmirovic, M. B.; Ticianelli, E. A.; Adzic, R. R.: Catalytic Activity-d-Band Center Correlation for the O2 Reduction Reaction on Platinum in Alkaline Solutions. *J Phys Chem C* **2007**, *111*, 404-410.

(21) Hu, G.; Nitze, F.; Gracia-Espino, E.; Ma, J.; Barzegar, H. R.; Sharifi, T.; Jia, X.; Shchukarev, A.; Lu, L.; Ma, C.; Yang, G.; Wagberg, T.: Small palladium islands embedded in palladium-tungsten bimetallic nanoparticles form catalytic hotspots for oxygen reduction. *Nat Commun* **2014**, *5*, 5253.

(22) Shi, Y.; Yin, S.; Ma, Y.; Lu, D.; Chen, Y.; Tang, Y.; Lu, T.: Oleylamine-functionalized palladium nanoparticles with enhanced electrocatalytic activity for the oxygen reduction reaction. *J Power Sources* **2014**, *246*, 356-360.

(23) Jin, Z.; Nackashi, D.; Lu, W.; Kittrell, C.; Tour, J. M.: Decoration, Migration, and Aggregation of Palladium Nanoparticles on Graphene Sheets. *Chem Mater* **2010**, *22*, 5695-5699.

(24) Yan, X.; Li, Q.; Li, L. S.: Formation and stabilization of palladium nanoparticles on colloidal graphene quantum dots. *J Am Chem Soc* **2012**, *134*, 16095-8.

(25) Bekyarova, E.; Hashimoto, A.; Yudasaka, M.; Hattori, Y.; Murata, K.; Kanoh, H.; Kasuya, D.; Iijima, S.; Kaneko, K.: Palladium nanoclusters deposited on single-walled carbon nanohorns. *J Phys Chem B* **2005**, *109*, 3711-3714.

(26) Truong-Phuoc, L.; Pham-Huu, C.; Da Costa, V.; Janowska, I.: Few-layered graphene-supported palladium as a highly efficient catalyst in oxygen reduction reaction. *Chem Commun* **2014**, *50*, 14433-14435.

(27) Norskov, J. K.; Rossmeisl, J.; Logadottir, A.; Lindqvist, L.; Kitchin, J. R.; Bligaard, T.; Jonsson, H.: Origin of the Overpotential for Oxygen Reduction at a Fuel-Cell Cathode. *J Phys Chem B* **2004**, *108*, 17886-17892.

(28) Chen, L. M.; Song, Y.; Hu, P. G.; Deming, C. P.; Guo, Y.; Chen, S. W.: Interfacial reactivity of ruthenium nanoparticles protected by ferrocenecarboxylates. *Physical Chemistry Chemical Physics* **2014**, *16*, 18736-18742.

(29) Matsubara, S.; Yokota, Y.; Oshima, K.: Palladium-catalyzed decarboxylation and decarbonylation under hydrothermal conditions: Decarboxylative deuteration. *Organic Letters* **2004**, *6*, 2071-2073.

(30) Huang, J.; Zhou, Z.; Song, Y.; Kang, X. W.; Liu, K.; Zhou, W.; Chen, S. W.: Electrocatalytic Activity of Palladium Nanocatalysts Supportedon Carbon Nanoparticles in Formic Acid Oxidation. *Journal of Electrochemistry* **2012**, *18*, 508-514.

(31) Lim, B.; Jiang, M. J.; Camargo, P. H. C.; Cho, E. C.; Tao, J.; Lu, X. M.; Zhu, Y. M.; Xia, Y. N.: Pd-Pt Bimetallic Nanodendrites with High Activity for Oxygen Reduction. *Science* **2009**, *324*, 1302-1305.

(32) Chen, S. W.; Templeton, A. C.; Murray, R. W.: Monolayer-protected cluster growth dynamics. *Langmuir* **2000**, *16*, 3543-3548.

(33) Zhou, Y.; Bao, Q.; Tang, L. A. L.; Zhong, Y.; Loh, K. P.: Hydrothermal Dehydration for the "Green" Reduction of Exfoliated Graphene Oxide to Graphene and Demonstration of Tunable Optical Limiting Properties. *Chem. Mater.* **2009**, *21*, 2950-2956.

(34) Pei, S. F.; Cheng, H. M.: The reduction of graphene oxide. *Carbon* **2012**, *50*, 3210-3228.

(35) Prestianni, A.; Ferrante, F.; Sulman, E. M.; Duca, D.: Density Functional Theory Investigation on the Nucleation and Growth of Small Palladium Clusters on a Hyper-Cross-Linked Polystyrene Matrix. *The Journal of Physical Chemistry C* **2014**, *118*, 21006-21013.

(36) Wagner, C. D.; Riggs, W. M.; Davis, L. E.; Moulder, J. F.; E., M. G.: Handbook of X-Ray Photoelectron Spectroscopy. **1979**.

(37) Dresselhaus, M. S.; Terrones, M.: Carbon-Based Nanomaterials From a Historical Perspective. *P Ieee* **2013**, *101*, 1522-1535.

(38) Zhou, Z. Y.; Kang, X.; Song, Y.; Chen, S.: Enhancement of the electrocatalytic activity of Pt nanoparticles in oxygen reduction by chlorophenyl functionalization. *Chem Commun (Camb)* **2012**, *48*, 3391-3.

(39) Bard, A. J.; Faulkner, L. R.: *Electrochemical methods: fundamentals and applications*; 2nd ed.; John Wiley: New York, 2001.

(40) Schumpe, A.; Adler, I.; Deckwer, W. D.: Solubility of Oxygen in Electrolyte-Solutions. *Biotechnology and Bioengineering* **1978**, *20*, 145-150.

(41) Anastasijevic, N. A.; Dimitrijevic, Z. M.; Adzic, R. R.: Oxygen reduction on a ruthenium electrode in alkaline electrolytes. **1886**, 351.

(42) Markovic, N. M.; Gasteiger, H. A.; Grgur, B. N.; Ross, P. N.: Oxygen reduction reaction on Pt(111): effects of bromide. *Journal of Electroanalytical Chemistry* **1999**, *467*, 157-163.

(43) Li, L.; Xing, Y. C.: Electrochemical durability of carbon nanotubes in noncatalyzed and catalyzed oxidations. *J Electrochem Soc* **2006**, *153*, A1823-A1828.

(44) Zhou, Z. Y.; Kang, X. W.; Song, Y.; Chen, S. W.: Ligand-Mediated Electrocatalytic Activity of Pt Nanoparticles for Oxygen Reduction Reactions. *J Phys Chem C* **2012**, *116*, 10592-10598.

Chapter 6

Oxygen Electroreduction Catalyzed by Palladium Nanoparticles Supported on Nitrogen-Doped Graphene Quantum Dots

6.1 Introduction

As demonstrated in the previous section of this dissertation, active supports are an effective method of altering the surface properties of metal nanoparticles and represent a promising route to enhance the activity of nanoparticles electrocatalysts towards oxygen reduction. In fact, the experimental studies that have detailed the ORR activity enhancement of GQDs-supported platinum, palladium and copper nanoparticles revealed that the GQDs exhibited various oxygenated species and their concentrations were readily manipulated by thermal treatment at controlled temperatures, as quantitatively determined by XPS and Raman measurements.[1-3] Additionally, the ORR activity of the corresponding metal-GQD nanocomposites displayed a volcano-shaped variation with the GQD defect concentration. This rise and fall of the ORR activity with the defect level is in strong agreement with the standing theories on the correlation between the d band structure and the strength of interactions between adsorbate and catalyst surface.

While the manipulation of oxygenated defects has indeed afforded a control over the activity of the associated metal particles, the rather high levels required for optimal activity will likely diminish the conductivity and compromise the eventual performance. An alternative is the incorporation of heteroatoms into the graphitic structure, in particular, nitrogen. The doping of nitrogen into the carbon backbone has been achieved by nitrogen plasma treatment of graphene nanoplatelets,[4,5] hydrothermal treatment of GQDs in ammonia,[6-8] and direct fixation from nitrogen in the air,[9] as well as by bottom-up synthesis based on CVD[10-12] or solvothermal

methods utilizing nitrogen containing precursors.[13,14] Nitrogen may be incorporated into the graphitic structure as pyridinic, pyrrolic, or graphitic quaternary centers, which are easily distinguished by XPS measurements based on the different binding energies of the N1s electrons.[5,10,14,15] Since nitrogen is more electronegative than carbon, it is likely that these centers will withdraw electron density from carbons, similar to oxygen, but without the disruption of the delocalized electron cloud since nitrogen centers are incorporated within the Csp^2 hybridization network. That is, nitrogen may provide the electron withdrawal necessary for activity enhancement of the metal nanoparticles but without compromising the electrical conductivity and stability of the support.[1-3] These unique characteristics of nitrogen-doped GQDs (NGQDs) may be exploited to enhance the ORR activity of palladium nanoparticles by forming PdNGQD nanocomposites. At present, palladium is less expensive and more abundant than platinum and is therefore valuable in the search for an economically viable clean energy source. Although the intrinsic catalytic activity is not generally seen as comparable to that of platinum, palladium electrocatalysts have displayed competitive activity and exhibited enhanced activity upon functionalization with N-doped graphene (NG), but the optimization of the synthetic conditions for such a system remains largely unexplored.[16] This is the primary motivation of the present study.

Herein, a series of nanocomposites based on palladium nanoparticles supported on NGQDs were prepared by hydrothermal treatment at 160 °C of citric acid and urea in the presence of palladium (II) chloride for a varied period of time.

The concurrent formation of NGQD and Pd nanoparticles allowed intimate contacts between them, as manifested in microscopic and spectroscopic measurements. Nitrogen was found to be incorporated into the graphitic structure in the pyrrolic and pyridinic forms, and the concentrations, along with the overall structural defects of the resulting NGQDS, were found to vary with the hydrothermal reaction time. The resulting nanocomposites exhibited apparent ORR activity in alkaline media, which was markedly higher than that with undoped GQDs. Control experiments with NGQDs-supported ruthenium nanoparticles prepared in a similar fashion suggested only minimal contributions from the NGQDs alone to the observed ORR activity, within the present experimental context. Significantly, a strong correlation was observed between the ORR activity and the pyrrolic nitrogen concentrations, which was accounted for by the preferred interactions between palladium and pyrrolic N moieties.

6.2 Results and Discussion

NGQDs have been previously prepared by hydrothermal reactions of citric acid and urea at elevated temperatures .[17] In the present study, the addition of a controlled amount of metal salts led to in situ formation of nanocomposites with metal nanoparticles incorporated within the NGQD molecular skeletons. Figure 6.1 depicts representative TEM micrographs of the series of PdNGQD nanocomposites. It can be seen that the composites all exhibited a structure characterized by nanoparticles of 10-20 nm clustered into larger superstructures of 100 nm and above. This morphology is similar to that of the nanocomposites where palladium was

deposited onto carbon nanoparticles or GQDs derived from pitch fiber.[3,18] However, as the electron density is much lower for carbon, it is difficult to identify the carbon materials in PdNGQDs.

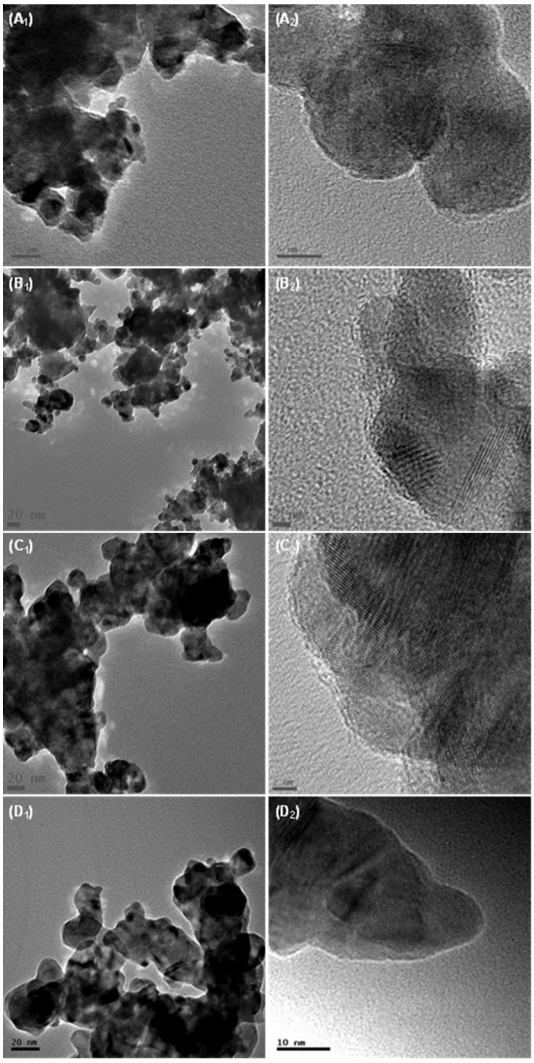

Figure 6.1. Representative TEM images of (A_1 and A_2) PdNGQD-1, (B_1 and B_2) PdNGQD-4, (C_1 and C_2) PdNGQD-8, (D_1 and D_2) PdNGQD-12. Scale bars are all 20 nm in panels (A_1) – (D_1), 5 nm in panel (A_2), 2 nm in (B_2) and (C_2), and 10 nm in (D_2).

This is very likely a result of the dynamics of simultaneous formation of NGQD and Pd nanoparticles that resulted in the embedment of metal nanostructures

within the graphitic matrix.[19-21] In the high-resolution images of panels (A_2) to (D_2), clearly defined lattice fringes can be readily observed where the interplanar spacing of 0.23 nm is consistent with that of the (111) crystalline planes of *fcc* palladium. Similar structures were observed with the PdGQD samples (Figure 6.2), whereas for the RuNGQD sample (Figure 6.3), ruthenium nanoparticles can be readily identified with a diameter of ca. 3 nm, where the lattice fringes of 0.21 nm are in good agreement with the interplanar distance between Ru(101) crystalline planes.[22]

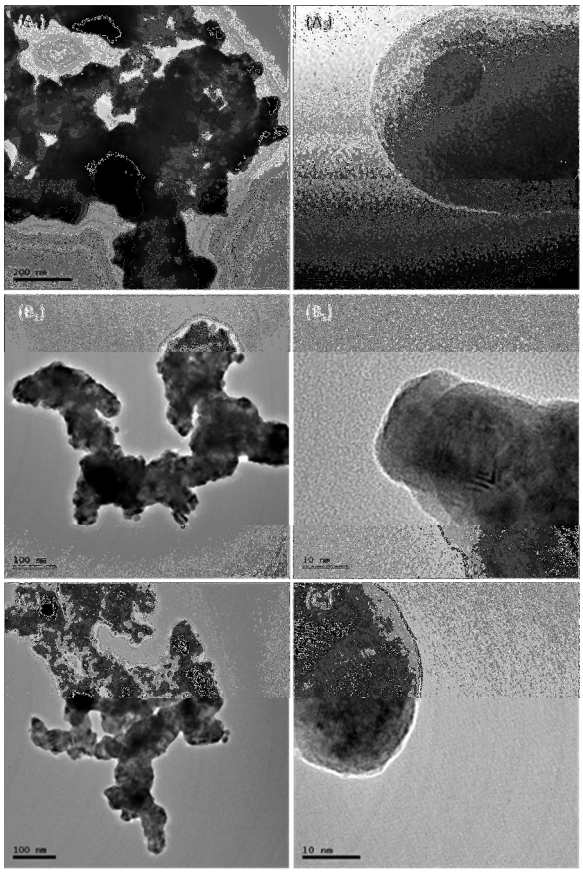

Figure 6.2. Representative TEM images of (A_1 and A_2) PdGQD-1, (B_1 and B_2) PdGQD-4, (C_1 and C_2) PdGQD-8. Scale bars is 200 nm in panel (A_1), 100 nm in panels (B_1) and (C_1), and 10 nm in panels (A_2)-(C_2).

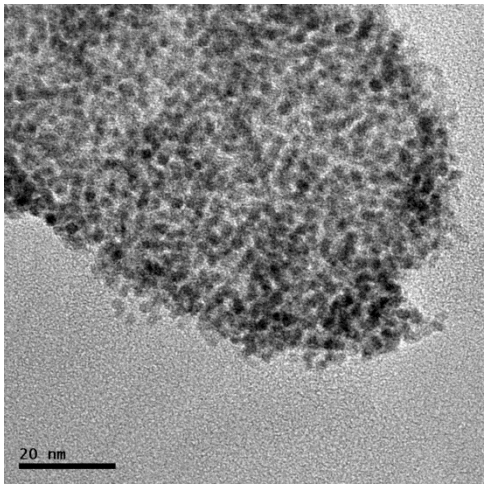

Figure 6.3. Representative TEM image of RuNGQD. Scale bar is 20 nm.

The formation of PdNGQD nanocomposites was confirmed by XPS measurements, where C1s, Pd3d and N1s electrons can be readily identified in the survey spectra at the binding energies of ca. 285, 340, and 400 eV, respectively. Further insights into the elemental compositions and valence states of the nanocomposites were obtained from the high resolution scans of the C1s, N1s, and Pd3d electrons, which are depicted in Figure 6.4.

From panels (A), one can see that the PdNGQD-1 and PdNGQD-4 samples both exhibited a doublet at ca. 334.9 and 340.2 eV, consistent with the $Pd3d_{5/2}$ and $Pd3d_{3/2}$ electrons of metallic palladium, respectively.[23] Yet these binding energies increased slightly with the samples prepared by longer hydrothermal reactions, 335.1 and 340.4 eV for PdNGQD-8, and 335.2 and 340.5 eV for PdNGQD-12. The results are summarized in Table 6.1.

For the C1s electrons in panels (B), de-convolution of the spectra yields four subpeaks, sp^2 carbon (C=C, yellow curves) at 284.7 eV, C–OH (dark blue curves) at

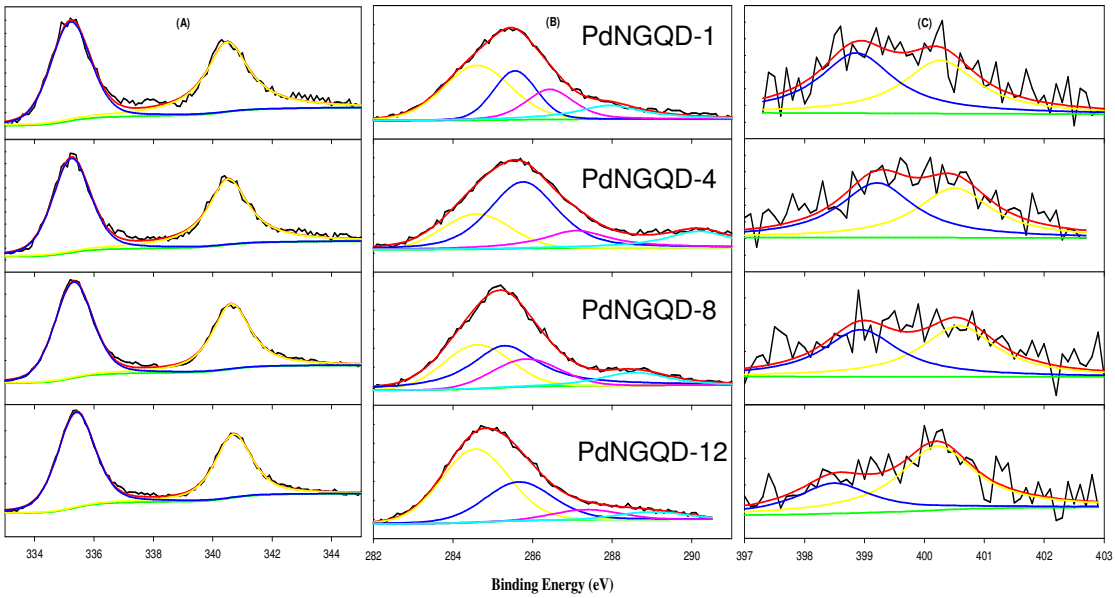

Figure 6.4. High-resolution XPS spectra of (A) Pd3d, (B) C1s and (C) N1s electrons of the series of PdNGQD nanocomposites. Black curves are experimental data and colored curves are deconvolution fits.

Sample	Pd			N dopants			
	Pd3d5/2 (eV)	Pd3d3/2 (eV)	Pd at.%	Pyridinic N (eV)	Pyrrolic N (eV)	N at.%	Pyridinic/Pyrrolic N ratio
PdNGQD-1	334.9	340.2	3.1	398.7	400.0	10.2	1.32
PdNGQD-4	334.8	340.2	2.9	398.8	399.9	9.0	1.06
PdNGQD-8	335.1	340.4	6.9	398.4	400.3	10.0	0.40
PdNGQD-12	335.2	340.5	6.0	398.2	399.9	10.8	0.37

Table 6.1. Summary of the XPS results of the series of PdNGQD nanocomposites

285.6 eV, carbonyl (C=O, pink curves) at 286.5 eV, and carboxylic (COOH, light blue curves) at 288.2 eV in each sample, indicating the formation of a large number of oxygenated species in the hydrothermal synthesis of NGQDs by citric acid and urea.[17] However, the concentrations of these carbon species varied markedly among the samples. In fact, based on the integrated peak areas, one can see that the fraction of (electron-withdrawing) C=O/COOH carbons decreased markedly with prolonging hydrothermal reaction time, at ca. 33% for PdNGQD-1, 30% for PdNGQD-4, 29%

for PdNGQD-8, and 13% for PdNGQD-12. This may be, at least in part, ascribed to the thermal instability of the C=O/COOH moieties. In fact, in previous studies with Pt, Pd and Cu nanoparticles supported on GQDs derived from carbon pitch fiber,[14,16,17] it has been observed that the C=O/COOH moieties could be removed effectively by hydrothermal treatment. Further contributions may arise from interfacial decarboxylation catalyzed by Pd.[24]

In the N1s spectra in panel (C), two major components can be identified by deconvolution. The peaks at ca. 398.5 eV (yellow curves) may be assigned to pyridinic nitrogen, whereas the other at ca. 400.0 eV (blue curve) most likely arose from pyrrolic nitrogen (Table 6.1).[25] This suggests that nitrogen was indeed doped into the graphitic molecular skeleton forming NGQDs. It should be noted that no quaternary nitrogen was identified at 401.7 eV. This is in sharp contrast with results observed previously in the hydrothermal synthesis of NGQDs with citric acid and urea but in the absence of metal salts, where an abundance of quaternary nitrogen was found with no signal from pyridinic nitrogen.[17] In the present study, the same procedure was adopted to prepare PdNGQD by adding a calculated amount of metal salts into the hydrothermal reactions. The fact that only pyridinic and pyrrolic nitrogens were formed in the graphitic scaffolds of PdNGQD is likely due to the preferred binding of palladium to these two nitrogen moieties.

Interestingly, based on the integrated peak areas, the overall concentration of nitrogen dopants was found to be almost invariant among the series of PdNGQD at 10 at.% (the corresponding concentration for Pd was 3.1 at.% for PdNGQD-1, 2.9 at.%

for PdNGQD-4, 6.9 at.% for PdNGQD-8, and 6.0 at.% for PdNGQD-12, Table 6.1); yet, the fractions of the pyrrolic and pyridinic nitrogens varied significantly. From panel (A) of Figure 6.5, one can see that the pyridinic nitrogen fraction decreased markedly, whereas the fraction of the pyrrolic nitrogen increased accordingly, with prolonging hydrothermal reaction time. This implies a gradual transformation of pyridinic nitrogens into pyrrolic nitrogen in the hydrothermal reactions. Note that in an earlier study, urea was utilized to dope graphene oxide and Pd nanoparticles were deposited on the resulting nitrogen-doped graphene oxide through thermal reduction of Pd^{2+} in a water/glycol mixture at 110 °C for 7 h,[26] XPS analysis showed that pyrrolic nitrogens accounted for over 80% of the nitrogen dopants. Additionally, it has been observed that palladium catalyzes the selective transformation of imines into pyrrolic derivatives at moderate temperatures and in the presence of O_2.[27]

Because pyrrolic nitrogen is known to be more acidic than pyridinic nitrogen (both are of p-type doping),[28,29] the increase of the pyrrolic nitrogen fraction would lead to a diminishment of the Pd electron density, due to the intimate interactions between palladium and the nitrogen dopants. Indeed, this is consistent with results from Figure 6.4 A, where the Pd3d binding energy increased from PdNGQD-1 to PdNGQD-12, as depicted in Figure 6.5 A. In fact, regression analysis showed a linear fit between the abundance of pyrrolic nitrogen centers and the Pd3d binding energy with an R^2 value of 0.833, while a negative correlation was observed for the linear fit between oxygenated carbon abundance and Pd3d binding energy, with an R^2 value of only 0.334. This strongly indicates that pyrrolic nitrogens are the primary

source of electronic modulation for palladium nanoparticles, within the present experimental context. Importantly, as the relative amount of pyrrolic nitrogens is well correlated with hydrothermal reaction time, deliberate structural manipulation may be achieved. Whereas additional contributions might arise from oxygenated species as observed previously with undoped GQDs,[1-3] the present observations imply that pyrrolic nitrogen likely dominated the manipulation of the metal nanoparticle properties, as nitrogen centers act as stronger anchoring sites than oxygen moieties.

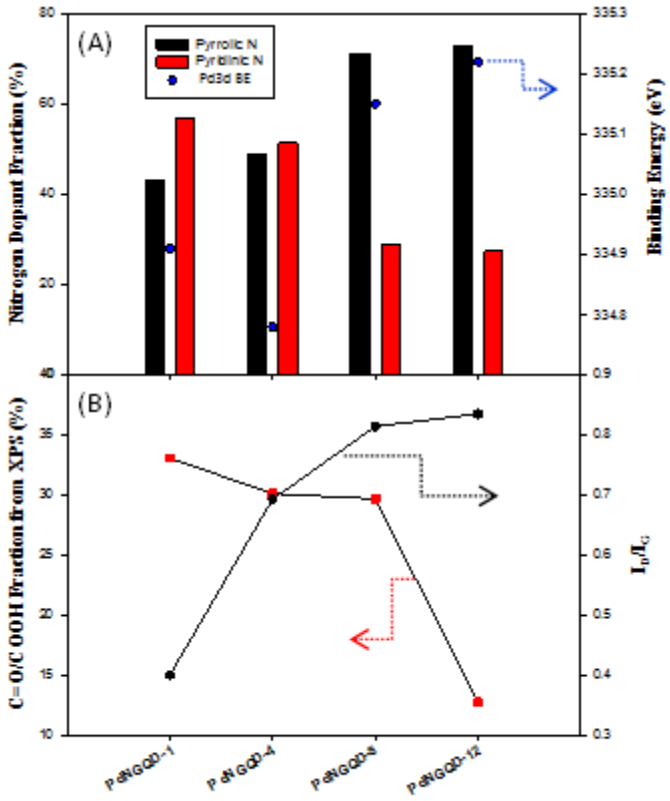

Figure 6.5. (A) Abundance of pyrrolic and pyridinic nitrogens, and Pd3d binding energy, and (B) percentage of oxygenated carbon from XPS and I_D/I_G ratio from Raman measurements for the series of PdNGQD nanocomposites.

The formation of PdNGQD nanocomposites was further confirmed by Raman spectroscopic measurements. Typically, graphitic material displays a G band (~1585 cm^{-1}) which represents the high frequency phonon of E2g symmetry within sp^2 carbons, as well as a D band (1350 cm^{-1}) which represents the phonon of A1g symmetry arising from a breathing mode at crystallite boundaries.[30-32] Since the G band arises from extended Csp^2 domains and the D band from interruptions in these domains, the relative ratio of their intensities (I_D/I_G) is widely used as a descriptor of the defect density for graphitic materials. Figure 6.6 A depicts the Raman spectra of the series of the PdNGQD nanocomposites, where the D and G bands are rather well-defined for each sample, indicating the successful graphitization of citric acid and urea by hydrothermal treatments.[17] Yet marked differences can be seen upon a closer analysis. For instance, whereas the D band positions are very consistent among the samples at ca. 1360 cm^{-1}, the G band positions are markedly different. Specifically, the G band energy increased in the order of PdNGQD-1 (1538 cm^{-1}) < PdNGQD-4 (1569 cm^{-1}) < PdNGQD-8 ≈ PdNGQD-12 (1374 cm^{-1}), suggesting that prolonging hydrothermal reaction time led to shrinking Csp^2 domains of the resulting NGQDs. Consistent results were obtained in the comparison of the I_D/I_G ratio, which increased in the same order of PdNGQD-1 (0.036) < PdNGQD-4 (0.82) < PdNGQD-8 (1.02) < PdNGQD-12 (2.06), indicating an increasingly defective structure of the NGQDs. This is in agreement with the increasing abundance of pyrrolic moieties in the series of PdNGQD samples, where the five-member pyrrolic rings would introduce

enhanced geometrical strains to the graphitic matrix, as compared to the six-member pyridinic moieties. This trend is graphically depicted in figure 6.5 B. In contrast, for

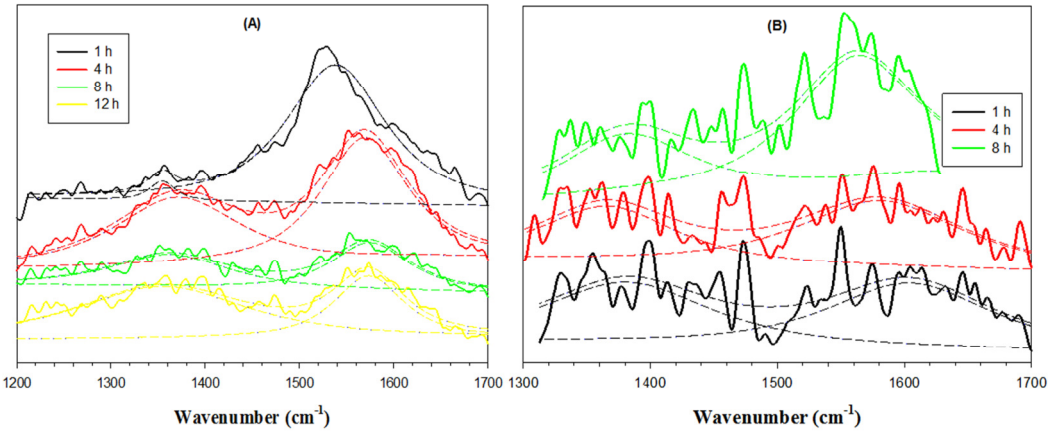

Figure 6.6. (A) Raman spectra of PdNGQD nanocomposites. (B) Raman spectra of PdGQD nanocomposites Solid curves are experimental data and dashed curves are deconvolution fits.

the control samples of PdGQD (Figure 6.6 B), a red-shift of the G band energy, along with a decreasing I_D/I_G ratio, was observed with increasing hydrothermal reaction time, indicating an increasing degree of graphitization of the GQDs due to effective removal of oxygenated species, as observed previously.[33-35]

Significantly, the series of PdNGQD composites all displayed apparent electrocatalytic activity towards oxygen reduction. A calculated amount of the nanocomposite catalysts was loaded onto a clean glassy carbon electrode, which was subject to electrochemical activation by rapid potential cycling within the potential range of +0.3 to +1.0 V in a nitrogen-saturated 0.1 M NaOH solution.

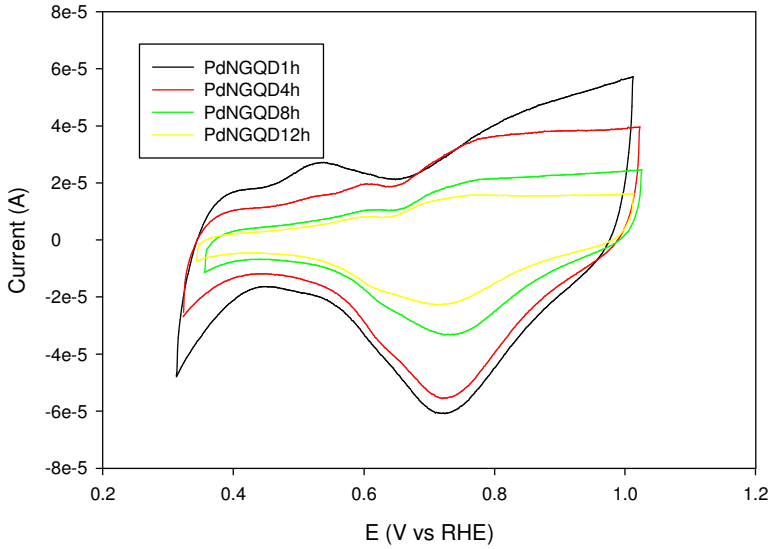

Figure 6.7. Cyclic voltammograms of a glassy carbon electrode modified with different Pd/GQD nanoparticles in nitrogen-saturated 0.1 M NaOH. Potential sweep rate 100 mV/s.

This range was deliberately chosen to avoid any complications from hydrogen absorption in Pd. From the steady-state voltammograms (Figure 6.7), a small broad peak between +0.65 and +0.95 V can be seen in the anodic scan, accompanied by a larger, sharper peak centered around +0.72 V in the cathodic scan. These respectively represent the formation and reduction of an oxide monolayer on the surface of the palladium particles and may be utilized to estimate the electrochemical surface area (ECSA), which is 3.80 m^2/g_{Pd} for PdNGQD-1, 2.99 m^2/g_{Pd} for PdNGQD-4, 2.46 m^2/g_{Pd} for PdNGQD-8, and 1.98 m^2/g_{Pd} for PdNGQD-12. These low values of ECSA are consistent with the rather extensive agglomeration of palladium particles observed in TEM measurements (Figure 6.1). Additionally, the palladium surface might be covered by the NGQDs which further limited electrochemical accessibility.

The activity for oxygen reduction was then evaluated in O_2-saturated 0.1 M KOH. Figure 6.8 A displays the RRDE voltammograms at the rotation rate of 1600 RPM. It can be seen that for each sample, non-zero current started to occur as the potential was swept negatively past ca. +0.99 V, increased rapidly with electrode potentials, and reached a plateau at potentials more negative than around +0.7 V, indicating apparent electrocatalytic activity of the PdNGQD nanocomposites towards oxygen reduction. Yet, from the voltammograms, one can see that the ORR activity varied among the series of PdNGQD nanocomposites. For instance, at +0.70 V, the current density increased by about 50% from PdNGQD-1 (40.8 A/m^2) and PdNGQD-4 (39.8 A/m^2) to PdNGQD-8 (61.6 A/m^2) and PdNGQD-12 (61.8 A/m^2), indicating that samples synthesized by longer hydrothermal reactions exhibited much better ORR activity.

In addition, by setting the ring potential at +1.5 V, collection experiments showed that the ring currents were at least two orders of magnitude lower than the disk currents, suggesting the production of a minimal amount of peroxide species during oxygen reduction. In fact, using the data in panel (A) as the example, the number of electron transfer (n) during ORR was evaluated with the equation, $= \frac{4I_{Disk}}{I_{Disk}+\frac{I_{Ring}}{N}}$, where I_{Disk} and I_{Ring} are the voltammetric currents at the disk and ring electrode respectively, and N is the collection efficiency. From panel (B), one can see that for the PdNGQD-8 sample, n is almost 4 within a large potential range of +0.50 to +1.0 V, indicating that oxygen underwent complete (4e) reduction to OH^-. The other samples also showed $n \approx 4$, but only at potentials less

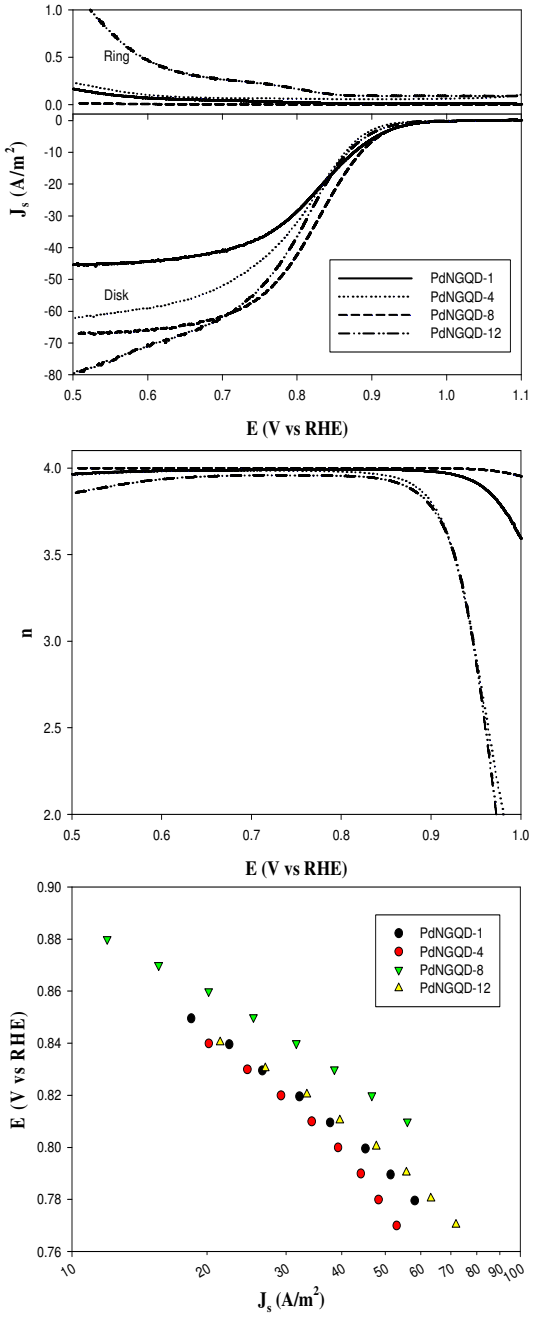

Figure 6.8. (A) RRDE voltammograms of PdNGQD nanocomposites in oxygen-saturated 0.1 M KOH at the electrode rotation rate of 1600 RPM. The potential of the ring electrode is set at+1.5 V. The palladium loadings are 6.52 μg for PdNGQD-1, 7.82 μg of Pd for PdNGQD-4, 6.28 μg for PdNGQD-8, and 5.01 μg for PdNGQD-12. DC ramp 10 mV/s. (B) Variation of the number of electron transfer (n) with electrode potentials. Data are calculated from the RRDE voltammograms in panel (A). (C)

Tafel plots of the various PdNGQD nanocomposites. Data are obtained from the Koutecky-Levich plots.

positive than +0.90 and +0.85 V, respectively. Taken together, these results indicate that the PdNGQD-8 sample stood out as the best catalyst among the series towards ORR.

Consistent behaviors were observed in the Tafel plot, where the kinetic current density was quantitatively assessed by Koutecky-Levich (K-L) analysis. From panel (C), it can be seen that for the PdNGQD series, the kinetic current density all increased drastically with increasingly negative electrode potential, due to enhanced electron transfer kinetics in ORR, and the Tafel slopes were found to be very close at 138 mV/dec for PdNGQD-1, 132 mV/dec for PdNGQD-4, 120 mV/dec for PdNGQD-8, and 128 mV/dec for PdNGQD-12, suggesting a similar reaction mechanism for ORR where the first electron reduction of oxygen was likely the rate-determining step.[36] In addition, it can also been seen that at all potentials the PdNGQD-8 sample exhibited the highest specific activity among the series of samples. For example, at +0.84 V, the kinetic current density was 22.4 A/m^2 for PdNGQD-1, 19.6 A/m^2 for PdNGQD-4, 31.6 A/m^2 for PdNGQD-8, and 21.4 A/m^2 for PdNGQD-12. This is likely a result of the strong influence by the nitrogen centers that facilitate charge transfer and provide optimal binding interaction between the metal surface and oxygenated intermediates.

Recently it has been shown that nitrogen-doped graphene derivatives exhibit high electrocatalytic activity towards ORR, which is largely attributed to pyridinic

nitrogens as the active sites.[37] In the present study, whereas pyridinic nitrogens were also formed in the PdNGQD nanocomposites, control experiments with RuNGQDs showed that the ORR activity was primarily due to the palladium nanoparticles and manipulated by the nitrogen dopants within the graphitic substrates. The onset potential for RuNGQD was around +0.70 V, about 300 mV more negative than that for any of the PdNGQD composites. Also, the RuNGQD did not reach a steady limiting current plateau even at +0.50 V and the current density was markedly lower. These results indicate minimal contributions from the nitrogen dopants towards oxygen reduction in this study. Rather, the influence of the nitrogen centers emerges through the electronic modification of the palladium particles through the varying amount of pyrrolic centers in the graphitic structure.

Pyridinic nitrogen bonds with two different carbons and donates one electron to the π cloud leaving two valence electrons localized on the N center. Pyrrolic nitrogen bonds to two different carbons similar to the pyridinic one, but because this is a five member ring, two electrons are donated to the conjugation system leaving one electron localized. This means that there will be an overall lower charge density on the pyrrolic centers compared to pyridinic. In fact, electron density maps of pyridine and pyrrole show that the pyridinic nitrogen has an appreciable electron density while pyrrolic has a significant electron deficiency. This notion is also reflected in the larger binding energy photoelectron observed for pyrrolic centers.

As oxygenated moieties have been shown to modulate the electronic environment of a neighboring metal particle based on the relative abundance of these

groups, we believe that such modulation can occur through varying the type of nitrogen center since the electronic environment of each center are significantly different, as previously discussed. That is, the more pyrrolic centers will withdraw more electron density from the metal particles while more pyridinic centers will not have such a drastic electron withdrawal effect and may even increase the electron density of associated metal particles due to the localized electron density of pyridinic centers. This is also apparent in the lower Pd 3d binding energies for samples with a larger abundance of pyridinic peaks and a larger Pd 3d binding energy for those with larger amounts of pyrrolic centers.

It should be noted though that the influence from the oxygenated defects is not insignificant, as indicated by the larger Pd3d peak binding energy for PdNGQD1h compared to PdNGQD4h, it is just not the dominant source as it was found to be for non N-doped graphitic materials. That is, although there are less pyrrolic nitrogen centers for the PdNGQD1h sample compared to the PdNGQD4h sample, there are significantly more oxygenated groups for the PdNGQD1h sample and therefore a slightly higher binding energy measured for the Pd3d electron for this sample when compared to the PdNGQD4h sample. The exact influence of each will be the focus of future studies with an emphasis on further understanding the exact dynamic of simultaneous nitrogen center formation, oxygen group removal, and metal ion reduction in addition to the further understanding of the activity enhancements provided by pyrrolic centers for metal surfaces toward oxygen reduction.

Furthermore, the activity of the PdNGQD samples compared very well to those of relevant composites based on palladium nanoparticles supported on graphitic substrates. For example, palladium nanoparticles were deposited on Vulcan XC72 carbon support through chemical and thermal reduction of the organometallic precursor [Pd3(μ-3-PhPz)6] resulting in particles with diameters 2.3 nm and 3.3 nm for chemical and thermal treatment respectively.[38] These samples displayed an onset potential for electrocatalytic oxygen reduction more than 100 mV lower than that for the PdNGQD samples, a likely consequence of nitrogen presence in the graphitic structure. Additionally, reduced graphene oxide supported palladium nanoparticles synthesized through photo assisted reduction of Na_2PdCl_4 in the presence of graphene oxide by exposure to a 500 W, high pressure mercury lamp for 12 hours.[39] Resulting particles averaged 3 nm and showed apparent ORR electrocatalytic activity displaying a mass activity of 88 A/g at +0.765 V vs RHE when evaluated in oxygen saturated 0.1 M KOH. The top sample in the present study exhibited a mass activity of 205 A/g at the same potential and given that the palladium nanoparticles photo reduced onto graphene averaged 3 nm in diameter and the clusters of the PdNGQD samples were larger than 100 nm, this disparity in mass activity is again a strong indication of the enhancements from nitrogen incorporations. Furthermore, the PdNGQD samples in this study exhibited a specific activity over 8 times better than that of PdGQD composites synthesized through thermal reduction of ionic palladium in the presence of GQDs.[3] These PdGQDs exhibited a very similar aggregated morphology with units larger than 100 nm and showed strong Raman D and G bands

resulting from the abundance of oxygenated moieties present. As the PdGQD system was optimized for ORR through selective removal of these oxygenated groups, the incorporation of nitrogen must then be responsible for such extreme activity gains in the present study. That is, the nitrogen incorporation provides a higher peak activity to strive towards.

6.3 Conclusion

In this study, PdNGQDs were synthesized for through a co-reduction method where palladium salt, citric acid, and urea were treated hyrdrothermally at 160 C for 1, 4, 8, and 12 hours to provide simultaneous formation of metal nanostructures and nitrogen doped graphitic backbone and to determine how synthesis duration will affect the composite structure and thus electrocatalytic activity. TEM imaging revealed large aggregates structures that differed little between synthesis times while XPS studies revealed that the type of nitrogen center, pyrrolic or pyridinic, was strongly depended on synthetic time with larger percentages of pyrrolic centers present with longer times. The relative abundance of pyrrolic centers also seem very well correlated with defect ratio from Raman measurements and the binding energy of the Pd 3d electrons. Electrocatalytic testing revealed that the PdNQGD1h exhibited the top mass activity while the PdNGQD8h exhibited the best specific activity, both of which were nearly 10 times better than activities of nitrogen free counterparts. The top electrocatalytic performance represents the optimal degree of electron withdrawal from the metal cores which was found to be modulated by a combination of oxygen and nitrogen influences but was largely dominated by the

characteristics of the nitrogen center. As the type of nitrogen center was easily influenced by duration of synthesis, we have presented an easy, energy efficient method for synthesizing palladium nanoparticle/nitrogen doped GQD composites with control over the nitrogen center specifics and thus the electronic environment of the active catalyst. Additionally, the co-reduction of precursors allows for the maximum association between the metal surface and NGQDs and thus an enhanced influence of the electron withdrawing nitrogen and oxygen groups.

6.4 References

(1) He, G. Q.; Song, Y.; Liu, K.; Walter, A.; Chen, S.; Chen, S. W.: Oxygen Reduction Catalyzed by Platinum Nanoparticles Supported on Graphene Quantum Dots. *Acs Catal* **2013**, *3*, 831-838.

(2) Song, Y.; Chen, S. W.: Graphene Quantum-Dot-Supported Platinum Nanoparticles: Defect-Mediated Electrocatalytic Activity in Oxygen Reduction. *Acs Appl Mater Inter* **2014**, *6*, 14050-14060.

(3) Deming, C. P.; Mercado, R.; Gadiraju, V.; Sweeney, S. W.; Khan, M.; Chen, S.: Graphene Quantum Dots-Supported Palladium Nanoparticles for Efficient Electrocatalytic Reduction of Oxygen in Alkaline Media. *Acs Sustain Chem Eng* **2015**, *3*, 3315-3323.

(4) Jafri, R. I.; Rajalakshmi, N.; Ramaprabhu, S.: Nitrogen doped graphene nanoplatelets as catalyst support for oxygen reduction reaction in proton exchange membrane fuel cell. *J Mater Chem* **2010**, *20*, 7114-7117.

(5) Chetty, R.; Kundu, S.; Xia, W.; Bron, M.; Schuhmann, W.; Chirila, V.; Brandl, W.; Reinecke, T.; Muhler, M.: PtRu nanoparticles supported on nitrogen-doped multiwalled carbon nanotubes as catalyst for methanol electrooxidation. *Electrochim Acta* **2009**, *54*, 4208-4215.

(6) Sun, H. J.; Gao, N.; Wu, L.; Ren, J. S.; Wei, W. L.; Qu, X. G.: Highly Photoluminescent Amino-Functionalized Graphene Quantum Dots Used for Sensing Copper Ions. *Chem-Eur J* **2013**, *19*, 13362-13368.

(7) Hu, C. F.; Liu, Y. L.; Yang, Y. H.; Cui, J. H.; Huang, Z. R.; Wang, Y. L.; Yang, L. F.; Wang, H. B.; Xiao, Y.; Rong, J. H.: One-step preparation of nitrogen-doped

graphene quantum dots from oxidized debris of graphene oxide. *J Mater Chem B* **2013**, *1*, 39-42.

(8) Tian, R. X.; Hu, S. L.; Wu, L. L.; Chang, Q.; Yang, J. L.; Liu, J.: Tailoring surface groups of carbon quantum dots to improve photoluminescence behaviors. *Appl Surf Sci* **2014**, *301*, 156-160.

(9) Jeon, I. Y.; Choi, H. J.; Ju, M. J.; Choi, I. T.; Lim, K.; Ko, J.; Kim, H. K.; Kim, J. C.; Lee, J. J.; Shin, D.; Jung, S. M.; Seo, J. M.; Kim, M. J.; Park, N.; Dai, L.; Baek, J. B.: Direct nitrogen fixation at the edges of graphene nanoplatelets as efficient electrocatalysts for energy conversion. *Sci Rep-Uk* **2013**, *3*.

(10) Jin, Z.; Yao, J.; Kittrell, C.; Tour, J. M.: Large-Scale Growth and Characterizations of Nitrogen-Doped Monolayer Graphene Sheets. *Acs Nano* **2011**, *5*, 4112-4117.

(11) Koos, A. A.; Murdock, A. T.; Nemes-Incze, P.; Nicholls, R. J.; Pollard, A. J.; Spencer, S. J.; Shard, A. G.; Roy, D.; Biro, L. P.; Grobert, N.: Effects of temperature and ammonia flow rate on the chemical vapour deposition growth of nitrogen-doped graphene. *Phys Chem Chem Phys* **2014**, *16*, 19446-19452.

(12) Wei, D. C.; Liu, Y. Q.; Wang, Y.; Zhang, H. L.; Huang, L. P.; Yu, G.: Synthesis of N-Doped Graphene by Chemical Vapor Deposition and Its Electrical Properties. *Nano Lett* **2009**, *9*, 1752-1758.

(13) Deng, D.; Pan, X.; Yu, L.; Cui, Y.; Jiang, Y.; Qi, J.; Li, W.-X.; Fu, Q.; Ma, X.; Xue, Q.; Sun, G.; Bao, X.: Toward N-Doped Graphene via Solvothermal Synthesis. *Chem Mater* **2011**, *23*, 1188-1193.

(14) Li, Y.; Zhao, Y.; Cheng, H.; Hu, Y.; Shi, G.; Dai, L.; Qu, L.: Nitrogen-doped graphene quantum dots with oxygen-rich functional groups. *J Am Chem Soc* **2012**, *134*, 15-8.

(15) Wang, G.; Jia, L. T.; Zhu, Y.; Hou, B.; Li, D. B.; Sun, Y. H.: Novel preparation of nitrogen-doped graphene in various forms with aqueous ammonia under mild conditions. *Rsc Adv* **2012**, *2*, 11249-11252.

(16) Jukk, K.; Kongi, N.; Matisen, L.; Kallio, T.; Kontturi, K.; Tammeveski, K.: Electroreduction of oxygen on palladium nanoparticles supported on nitrogen-doped graphene nanosheets. *Electrochim Acta* **2014**, *137*, 206-212.

(17) Qu, D.; Zheng, M.; Du, P.; Zhou, Y.; Zhang, L.; Li, D.; Tan, H.; Zhao, Z.; Xie, Z.; Sun, Z.: Highly luminescent S, N co-doped graphene quantum dots with broad visible absorption bands for visible light photocatalysts. *Nanoscale* **2013**, *5*, 12272-7.

(18) Huang, J.; Zhou, Z.; Song, Y.; Kang, X. W.; Liu, K.; Zhou, W.; Chen, S. W.: Electrocatalytic Activity of Palladium Nanocatalysts Supportedon Carbon Nanoparticles in Formic Acid Oxidation. *Journal of Electrochemistry* **2012**, *18*, 508-514.

(19) Templeton, A. C.; Wuelfing, M. P.; Murray, R. W.: Monolayer protected cluster molecules. *Accounts Chem Res* **2000**, *33*, 27-36.

(20) Chen, S. W.; Templeton, A. C.; Murray, R. W.: Monolayer-protected cluster growth dynamics. *Langmuir* **2000**, *16*, 3543-3548.

(21) Lim, B.; Jiang, M. J.; Camargo, P. H. C.; Cho, E. C.; Tao, J.; Lu, X. M.; Zhu, Y. M.; Xia, Y. N.: Pd-Pt Bimetallic Nanodendrites with High Activity for Oxygen Reduction. *Science* **2009**, *324*, 1302-1305.

(22) Ghosh, D.; Chen, S. W.: Solid-state electronic conductivity of ruthenium nanoparticles passivated by metal-carbon covalent bonds. *Chemical Physics Letters* **2008**, *465*, 115-119.

(23) Wagner, C. D.; Riggs, W. M.; Davis, L. E.; Moulder, J. F.; Muilenberg, G. E.: *Handbook of x-ray photoelectron spectroscopy : a reference book of standard data for use in x-ray photoelectron spectroscopy*; Perkin-Elmer Corp.: Eden Prairie, Minn., 1979.

(24) Chen, L. M.; Song, Y.; Hu, P. G.; Deming, C. P.; Guo, Y.; Chen, S. W.: Interfacial reactivity of ruthenium nanoparticles protected by ferrocenecarboxylates. *Physical Chemistry Chemical Physics* **2014**, *16*, 18736-18742.

(25) Liu, X. J.; Li, L. G.; Zhou, W. J.; Zhou, Y. C.; Niu, W. H.; Chen, S. W.: High-Performance Electrocatalysts for Oxygen Reduction Based on Nitrogen-Doped Porous Carbon from Hydrothermal Treatment of Glucose and Dicyandiamide. *Chemelectrochem* **2015**, *2*, 803-810.

(26) Movahed, S. K.; Dabiri, M.; Bazgir, A.: Palladium nanoparticle decorated high nitrogen-doped graphene with high catalytic activity for Suzuki-Miyaura and Ullmann-type coupling reactions in aqueous media. *Applied Catalysis a-General* **2014**, *488*, 265-274.

(27) Meng, L.; Wu, K.; Liu, C.; Lei, A.: Palladium-catalysed aerobic oxidative Heck-type alkenylation of Csp3-H for pyrrole synthesis. *Chem Commun (Camb)* **2013**, *49*, 5853-5.

(28) Kang, H. S.; Jeong, S.: Nitrogen doping and chirality of carbon nanotubes. *Physical Review B* **2004**, *70*.

(29) Ewels, C. P.; Glerup, M.: Nitrogen doping in carbon nanotubes. *Journal of Nanoscience and Nanotechnology* **2005**, *5*, 1345-1363.

(30) Dresselhaus, M. S.; Terrones, M.: Carbon-Based Nanomaterials From a Historical Perspective. *P Ieee* **2013**, *101*, 1522-1535.

(31) Ferrari, A. C.; Basko, D. M.: Raman spectroscopy as a versatile tool for studying the properties of graphene. *Nature Nanotechnology* **2013**, *8*, 235-246.

(32) Tuinstra, F.: Raman Spectrum of Graphite. *The Journal of Chemical Physics* **1970**, *53*, 1126.

(33) Norskov, J. K.; Rossmeisl, J.; Logadottir, A.; Lindqvist, L.; Kitchin, J. R.; Bligaard, T.; Jonsson, H.: Origin of the Overpotential for Oxygen Reduction at a Fuel-Cell Cathode. *J Phys Chem B* **2004**, *108*, 17886-17892.

(34) Stephens, I. E. L.; Bondarenko, A. S.; Grønbjerg, U.; Rossmeisl, J.; Chorkendorff, I.: Understanding the electrocatalysis of oxygen reduction on platinum and its alloys. *Energ Environ Sci* **2012**, *5*, 6744.

(35) Kitchin, J. R.; Norskov, J. K.; Barteau, M. A.; Chen, J. G.: Modification of the surface electronic and chemical properties of Pt(111) by subsurface 3d transition metals. *J Chem Phys* **2004**, *120*, 10240-6.

(36) Song, C.; Zhang, J.: *PEM Fuel Cell Electrocatalysis and Catalyst Layers: Fundamentals and Applications*, 2008.

(37) Guo, D. H.; Shibuya, R.; Akiba, C.; Saji, S.; Kondo, T.; Nakamura, J.: Active sites of nitrogen-doped carbon materials for oxygen reduction reaction clarified using model catalysts. *Science* **2016**, *351*, 361-365.

(38) Arroyo-Ramirez, L.; Montano-Serrano, R.; Luna-Pineda, T.; Roman, F. R.; Raptis, R. G.; Cabrera, C. R.: Synthesis and characterization of palladium and palladium-cobalt nanoparticles on Vulcan XC-72R for the oxygen reduction reaction. *ACS Appl Mater Interfaces* **2013**, *5*, 11603-12.

(39) Huang, Y. X.; Xie, J. F.; Zhang, X.; Xiong, L.; Yu, H. Q.: Reduced graphene oxide supported palladium nanoparticles via photoassisted citrate reduction for enhanced electrocatalytic activities. *ACS Appl Mater Interfaces* **2014**, *6*, 15795-801.